

# Quantum computation of molecular electronic spectroscopy on a superconducting quantum processor

Kaixuan Huang<sup>2,3†</sup>, Xiaoxia Cai<sup>1†</sup>, Hao Li<sup>3,7†</sup>, Zi-Yong Ge<sup>5</sup>, Ruijuan Hou<sup>1</sup>, Hekang Li<sup>3</sup>, Tong Liu<sup>3,4</sup>, Yunhao Shi<sup>3,4</sup>, Chitong Chen<sup>3,4</sup>, Dongning Zheng<sup>3,4,6</sup>, Kai Xu<sup>3,4,6\*</sup>, Zhi-Bo Liu<sup>2\*</sup>, Zhendong Li<sup>1\*</sup>, Heng Fan<sup>3,4,6\*</sup>, Wei-Hai Fang<sup>1</sup>

<sup>1</sup> Key Laboratory of Theoretical and Computational Photochemistry, Ministry of Education, College of Chemistry, Beijing Normal University, Beijing 100875, China

<sup>2</sup> The Key Laboratory of Weak Light Nonlinear Photonics, Ministry of Education, Teda Applied Physics Institute and School of Physics, Nankai University, Tianjin 300457, China

<sup>3</sup> Institute of Physics, Chinese Academy of Sciences, Beijing 100190, China

<sup>4</sup> School of Physical Sciences, University of Chinese Academy of Sciences, Beijing 100190, China

<sup>5</sup> Theoretical Quantum Physics Laboratory, RIKEN Cluster for Pioneering Research, Wako-shi, Saitama 351-0198, Japan

<sup>6</sup> CAS Center for Excellence in Topological Quantum Computation, University of Chinese Academy of Sciences, Beijing 100190, China

<sup>7</sup> School of Physics, Northwest University, Xi'an 710127, China

† These authors contributed equally;

\* To whom correspondence should be addressed;

E-mail: kaixu@iphy.ac.cn, liuzb@nankai.edu.cn, zhendongli@bnu.edu.cn, hfan@iphy.ac.cn

**Predictive simulation of molecular response properties is crucial for interpreting experimental spectroscopies and accelerating materials design. On classical computers, it is often hampered by the exponential growth of the many-electron Hilbert space as the molecular size increases. Here, we report the first**

**proof-of-principle experimental demonstration of a scalable quantum computational approach for simulating molecular electronic spectroscopy on a superconducting quantum processor. We benchmark the feasibility of this approach by computing dynamic polarizabilities of the hydrogen molecule, and then demonstrate its potential for solving important practical problems by simulating ultraviolet-visible absorption spectra of polyacenes and X-ray absorption spectra of carbon monoxide. Our results open up the possibility of using near-term quantum computers as a new computational tool for reliably simulating linear and nonlinear response properties of more complex systems in the near future.**

## **Introduction**

In silico simulation of molecular response properties, such as dynamic polarizabilities, absorption/emission spectra, and nonlinear optical properties, has become an essential component in virtual design of new materials with specific properties (1). The need for accurate and efficient computational tools is more urgent than before in the era of data driven material research, since they can significantly accelerate the high-throughput screening of the enormous candidates. Despite decades of effort and tremendous progress in methodological developments, predictive simulation of molecular response properties remains a fundamental challenge for electronic structure methods on classical computers (2, 3). While density functional theory (DFT) and its time-dependent extension (TD-DFT) have been the workhorse for simulating structural and response properties of large molecules, the limitations of density functional approximations are well-known (4), especially for strongly correlated systems. More accurate wavefunction-based methods are constrained to small molecules by their steep computational scaling with respect to the system size (2). For instance, the exact method for solving the many-electron Schrödinger

equation within a given basis set, full configuration interaction (FCI) or exact diagonalization, has an exponential scaling in both physical memory and computational time.

As initially suggested by Feynman (5), a promising way to overcome the *exponential wall* in simulating interacting many-body systems is to use quantum computers, which are controllable quantum mechanical devices. Recent breakthroughs in quantum computing technology with superconducting quantum processors have achieved the quantum computational advantage for specific sampling problems (6, 7), for which quantum computers can outperform the most powerful current supercomputers. Quantum chemistry is one of the most promising fields (8–10), where these noisy intermediate-scale quantum (11) (NISQ) devices may offer a practical quantum advantage for important problems such as designing new catalysts for nitrogen fixation (12–14). Previous quantum simulations of molecules have almost exclusively focused on solving the ground-state problem (15–19), which is the very first step towards simulating molecular properties. In particular, the variational quantum eigensolver (18, 19) (VQE), belonging to the class of hybrid quantum-classical algorithms (20), has attracted much interest due to its feasibility on NISQ devices. Once the ground state is prepared on quantum computers, molecular properties described by ground-state expectation values, such as dipole moments (21), can be trivially computed by measurements. In contrast, computing linear and nonlinear response properties is far more challenging, because they implicitly involve not only the ground state but also all the excited states (3). Existing quantum algorithms for linear response functions largely rely on computing time-correlation functions using quantum computers (22–24), which can later be Fourier transformed to the frequency domain. Recently, we introduced a different theoretical framework for computing response properties in the frequency domain (25), which employs quantum algorithms such as the Harrow-Hassidim-Lloyd algorithm (26) as subroutines for solving linear response equations on quantum computers. Theoretically, all these quantum algorithms promise an exponential speedup over classical FCI-

based response algorithms (2). Unfortunately, they are generally infeasible for molecules on NISQ devices, due to the requirement of very deep quantum circuits for implementing the time evolution  $e^{-i\hat{H}_0 t}$  with the molecular Hamiltonian  $\hat{H}_0$  (17) as a common component in these algorithms. Therefore, how to compute response properties of molecules by leveraging the power of NISQ devices remains a highly nontrivial open problem and has not been experimentally demonstrated.

Here, we describe a pragmatic quantum computational approach, termed the variational quantum response (VQR) approach, for computing linear response properties. Building upon the frequency-domain framework (25), we design efficient quantum circuits with low depths for solving the linear response problem in a variational hybrid quantum-classical way and introduce an error mitigation (EM) strategy based on symmetry projection to mitigate the impact of noises inherent in NISQ devices (9). With the VQR approach, we report the first proof-of-principle quantum simulation of molecular electronic spectroscopy on a superconducting quantum processor (27, 28). The feasibility of this approach is benchmarked for computing dynamic polarizabilities of the hydrogen molecule ( $\text{H}_2$ ) at three geometries with different electron correlation strengths. Its potential for solving important practical problems is revealed by simulating ultraviolet-visible (UV-Vis) absorption spectra of polyacenes and X-ray absorption spectra of carbon monoxide. These results demonstrate that it is the combination of the three key ingredients in the VQR approach, viz., frequency-domain formulation for response properties, variational algorithms with low-depth quantum circuits, and error mitigation techniques, that enables the quantum simulation of molecular linear response properties on NISQ devices. Our work has opened up the possibility of identifying a practical quantum computational advantage in simulating molecular response properties.

## Results

### Variational quantum response (VQR) algorithm and experimental implementation

We outline how VQR works for simulating linear response properties, which characterize the first order response of molecules to an applied external field and are essential for understanding absorption and emission properties of materials. Further details are provided in the Materials and Method as well as Supplementary Materials. Specifically, we consider the following linear response function

$$\chi(\omega) = \sum_k \frac{|\langle \Psi_k | \hat{V} | \Psi_0 \rangle|^2}{\omega_{k0} - (\omega + i\gamma)}, \quad (1)$$

where  $\omega$  is the frequency of the external field and  $\gamma$  is a broadening parameter. This function encodes all the information of the excitation process from the ground state  $|\Psi_0\rangle$  to the  $k$ -th excited state  $|\Psi_k\rangle$  due to the perturbation  $\hat{V}$ , i.e., the excitation energy  $\omega_{k0} = E_k - E_0$  and the corresponding transition amplitude  $|\langle \Psi_k | \hat{V} | \Psi_0 \rangle|^2$ . Here, we focus on the case where  $\hat{V}$  is a dipole operator  $\{\hat{x}, \hat{y}, \hat{z}\}$ , such that  $\chi(\omega)$  represents the resonant contribution to dipole polarizability, whose imaginary part is related with the linear absorption of radiation  $\sigma_{\text{abs}}(\omega)$  by a randomly oriented molecular sample in the electric-dipole approximation (3), viz.,  $\sigma_{\text{abs}}(\omega) = \frac{4\pi\omega}{c} \text{Im}\bar{\chi}(\omega)$  with  $\bar{\chi} = \frac{1}{3}(\chi_{xx} + \chi_{yy} + \chi_{zz})$  and  $c$  being the speed of light. Shapes of  $\sigma_{\text{abs}}(\omega)$  can be understood by noting that  $\text{Im}\chi(\omega) = \sum_n |\langle \Psi_n | \hat{V} | \Psi_0 \rangle|^2 \frac{\gamma}{(\omega_{n0} - \omega)^2 + \gamma^2}$  is a weighted superposition of Lorentzians with a common full width at half maximum (FWHM)  $2\gamma$ .

Exact calculations of  $\chi(\omega)$  are intractable on classical computers, as the number of excited states scales exponentially with the system size. To compute  $\chi(\omega)$  with quantum processors, the first step is to map the problem of interacting electrons to a corresponding problem of qubits, each of which is a two-level quantum system and forms the fundamental unit of quantum computers. As shown in Fig. 1A, this preprocessing step starts with a classical quantum

chemical calculation of molecules, typically using self-consistent field methods, to obtain a set of molecular orbitals (MOs). Then, a fermion-to-qubit mapping (29, 30) is chosen to transform the second-quantized  $\hat{H}_0$  and  $\hat{V}$  for electrons to their counterparts for  $n$  qubits, which are linear combinations of Pauli terms, e.g.,  $\hat{H}_0 = \sum_k h_k P_k$  with  $P_k = \sigma_0^k \otimes \sigma_1^k \otimes \cdots \otimes \sigma_{n-1}^k$  being a tensor product of Pauli operators ( $\sigma_i \in \{I, X, Y, Z\}$ ). The next step is to prepare the ground state  $|\Psi_0\rangle$  using VQE (18, 19). As exemplified in Fig. 1B, a shallow parameterized quantum circuit (PQC)  $U_0(\vec{\theta}_0)$  composed of parameterized single-qubit gates with a set of free angles  $\vec{\theta}_0$  (e.g., the rotation gate  $Z_\theta$  around the Z axis) and two-qubit entangling gates (e.g.,  $\sqrt{\text{iSWAP}}$  or CNOT) is designed to evolve the initial state  $|0\rangle$  to a target state, i.e.,  $|\Psi_0\rangle = U_0(\vec{\theta}_0)|0\rangle$ . The optimal parameters  $\vec{\theta}_0^{\text{opt}}$  are determined by classically minimizing the energy function  $E(\vec{\theta}_0) = \langle \Psi_0 | \hat{H} | \Psi_0 \rangle = \sum_k h_k \langle \Psi_0 | P_k | \Psi_0 \rangle$ , with the necessary expectation values  $\langle \Psi_0 | P_k | \Psi_0 \rangle$  measured on quantum processors.

Having the ground state, we introduce a two-step VQR approach for computing  $\chi(\omega)$  in an interested frequency region (see Fig. 1C). In the frequency-domain framework (25), to circumvent the prohibitive sum over excited states in Eq. 1, an auxiliary response state  $|\Psi(\omega)\rangle$  is defined by a linear response equation,

$$\hat{A}(\omega)|\Psi(\omega)\rangle = \hat{V}|\Psi_0\rangle, \quad \hat{A}(\omega) = \hat{H}_0 - E_0 - (\omega + i\gamma), \quad (2)$$

such that  $\chi(\omega)$  becomes a simple expectation value  $\chi(\omega) = \langle \Psi(\omega) | \hat{A}^\dagger(\omega) | \Psi(\omega) \rangle$ , similar to the energy expression. On classical computers, both solving the linear system of equations in Eq. 2 and computing the expectation value for  $\chi(\omega)$  scale exponentially in  $n$ . In this work, following the variational hybrid quantum-classical algorithm (31, 32) for linear system of equations, we present a pragmatic algorithmic primitive for solving the linear response equation on NISQ devices, which can also be extended to high-order response equations for nonlinear response properties. We first introduce a PQC for the normalized response state

$|x\rangle = |\Psi(\omega)\rangle / \|\Psi(\omega)\| = U_1(\vec{\theta}_1)|0\rangle$ , and then find the optimal parameters  $\vec{\theta}_1^{\text{opt}}$  by minimizing a cost function

$$L(\vec{\theta}_1) = \langle \Psi_0 | \hat{V}^\dagger \hat{V} | \Psi_0 \rangle \langle x | \hat{A}^\dagger(\omega) \hat{A}(\omega) | x \rangle - |\langle \Psi_0 | \hat{V}^\dagger \hat{A}(\omega) | x \rangle|^2. \quad (3)$$

Figure 1C displays the quantum circuits designed for evaluating  $\langle x | \hat{A}^\dagger(\omega) \hat{A}(\omega) | x \rangle$  and  $|\langle \Psi_0 | \hat{V}^\dagger \hat{A}(\omega) | x \rangle|^2$  in  $L(\vec{\theta}_1)$ . The newly introduced quantum circuits for computing the most difficult term  $|\langle \Psi_0 | \hat{V}^\dagger \hat{A}(\omega) | x \rangle|^2$  have a depth at most equal to the sum of depths for  $U_0(\vec{\theta}_0)$  and  $U_1(\vec{\theta}_1)$ , and do not involve any controlled operation on  $U_0(\vec{\theta}_0)$  nor  $U_1(\vec{\theta}_1)$  unlike in previous works (31, 32). This simplicity makes VQR more feasible for NISQ devices than those quantum algorithms requiring deep quantum circuits for computing response properties (22–25). For special  $\hat{V}^\dagger \hat{A}(\omega)$  in this work, the evaluation of  $|\langle \Psi_0 | \hat{V}^\dagger \hat{A}(\omega) | x \rangle|^2$  is further reduced using symmetries to quantum circuits without involving the ancilla qubit (see Supplementary Materials in detail). Once  $\vec{\theta}_1^{\text{opt}}$  have been found,  $\chi(\omega)$  at a given frequency can be computed from

$$\chi(\omega) = \langle x | \hat{A}^\dagger(\omega) | x \rangle \frac{\langle \Psi_0 | \hat{V}^\dagger \hat{V} | \Psi_0 \rangle}{\langle x | \hat{A}^\dagger(\omega) \hat{A}(\omega) | x \rangle}, \quad (4)$$

by measuring the individual expectation value on quantum computers.

To mitigate the impact of noises in NISQ devices, we further introduce a EM strategy based on symmetry projection for expectation values in VQE/VQR. Specifically, if a quantum state  $|\Psi\rangle$  (ground or response state) resides in a subspace with spatial or spin symmetry, a projector  $\mathcal{P}$  can be associated with this subspace such that  $\mathcal{P}|\Psi\rangle = |\Psi\rangle$ . In the presence of noises in experiments, the quantum system needs to be described a density matrix (33)  $\rho_{\text{exp}}$  instead of  $|\Psi\rangle$ , which can have undesirable components outside the correct subspace. To get a better estimation of the expectation value  $\langle \Psi | \hat{O} | \Psi \rangle$  for an operator  $\hat{O}$  that commutes with  $\mathcal{P}$  (e.g.,  $\hat{H}_0$ ,  $\hat{A}(\omega)$ ,  $\hat{A}^\dagger(\omega)\hat{A}(\omega)$ , and  $\hat{V}^\dagger\hat{V}$ ), we can use  $\langle \Psi | \hat{O} | \Psi \rangle^{\text{EM}} \equiv \text{tr}(\tilde{\rho}\hat{O}) = \text{tr}(\rho_{\text{exp}}\hat{O}\mathcal{P})/\text{tr}(\rho_{\text{exp}}\mathcal{P})$  with  $\tilde{\rho} = \mathcal{P}\rho_{\text{exp}}\mathcal{P}/\text{tr}(\rho_{\text{exp}}\mathcal{P})$  being the symmetry projected density matrix. This EM strategy may require a small amount of additional measurements for computing the expectation values

of  $\hat{O}\mathcal{P}$  and  $\mathcal{P}$ , but the payoff for a more accurate estimation for expectation values such as  $\langle x|\hat{A}^\dagger(\omega)\hat{A}(\omega)|x\rangle$  is crucial for the accurate computation of  $\chi(\omega)$ . The choice of  $\mathcal{P}$  for different problems is presented in Materials and Methods.

The present VQR approach allows to directly compute spectra in an interested frequency region without explicitly addressing excited states. This is particularly advantageous in the region with a large density of states or a region of high energy such as the X-ray region. We implement it on a programmable superconducting quantum processor (27) (see Fig. 2A), which consists of 20 frequency-tunable transmon qubits connected via a central resonator. A special feature of this device is that the  $\sqrt{i\text{SWAP}}_{i,j}$  gate can be realized between any pair of qubits  $Q_i$  and  $Q_j$  (see Supplementary Materials). Fermion-to-qubit mappings used in the experiments for  $\text{H}_2$  (or polyacenes) and CO are shown in Figs. 2B and 2C, respectively. As the first proof-of-principle experimental demonstration of VQR, we employ PQC capable of encoding the exact ground or response state as variational ansätze, and perform numerical optimizations by scanning the entire parameter space. This allows us to focus on the limitation of VQR solely due to noises on NISQ devices. Extensions to the uses of low-depth wavefunction ansätze scalable for larger systems (34) and quantum gradients for optimizations (28) are straightforward.

### **Benchmark: dynamic polarizabilities of $\text{H}_2$ from two-qubit simulations**

Due to its conceptual simplicity,  $\text{H}_2$  in a minimal basis set has become a test bed for new quantum algorithms (16, 18, 34–37). We benchmark the feasibility of VQR by comparing the simulated  $\chi(\omega)$  with the corresponding FCI results for  $\text{H}_2$  at three representative bond lengths ( $R = R_e$  (38),  $2R_e$ , and  $3R_e$ ), which cover the weak, intermediate, and strong electron correlation regimes. We first compute the ground state using VQE (18, 19) with the PQC ansatz in Fig. 3A. The computed ground-state energies in Fig. 3B shows that the EM strategy improves the VQE(raw) energies considerably, making the difference with the FCI reference on the order

of chemical accuracy (see Table S5). With the optimized ground states, we compute  $\chi(\omega)$  for  $\hat{V} = \hat{z}$  and  $\gamma = 0.1$  a.u. using VQR with the PQC in Fig. 3C for  $|x(\theta_1)\rangle$ . As shown in Fig. 3D,  $\chi(\omega)$  computed using VQR(EM) agrees well with the FCI reference in most of the studied frequency region at all the three geometries. In particular, the absorption peaks responsible for the transition from the ground state to the first singlet excited states  $|\Psi_u\rangle = \frac{1}{\sqrt{2}}(|10\rangle + |01\rangle)$  are well-reproduced.

Meanwhile, small deviations from the FCI results are observed at  $\omega$  around 0.6, 0.1, and 0.0 a.u. for  $R = R_e, 2R_e,$  and  $3R_e,$  respectively. These frequencies turn out to be exactly the position of the first triplet excited state at each geometry (see Supplementary Materials). In these regions, the two terms in  $L(\theta_1)$  are very close to each other and the difference is on the order of  $\gamma^2$ . Thus, the computation of  $L(\theta_1)$  is prone to noises, such that the optimized angle  $\theta_1^{\text{opt}}$  is less accurate (see Fig. S9). To verify that the error in the experimental response state is dominated by the inaccuracy in the optimized angle rather than experimental imperfections in realizing the quantum circuit in Fig. 3C, we characterized the output state  $|x(\theta_1^{\text{opt}})\rangle$  using quantum state tomography (33) (QST) at three representative frequencies ( $\omega = 0, 0.6,$  and  $0.96$  a.u.) for  $R = R_e$ . The experimental response state  $\rho_{\text{exp}}$ , the ideal response state  $\rho_{\text{ideal}} = |\Psi_u\rangle\langle\Psi_u|$ , and the fidelity (33)  $F(\rho_{\text{exp}}, |\Psi_u\rangle) = \sqrt{\langle\Psi_u|\rho_{\text{exp}}|\Psi_u\rangle}$  as a measure for the similarity between  $\rho_{\text{exp}}$  and  $|\Psi_u\rangle$  are shown in Fig. 3E. It is clear that at the absorption peak position  $\omega = 0.96$ , where  $\theta_1^{\text{opt}}$  is accurately determined, the fidelity  $F$  can be very close to one. Thus, the low fidelity at  $\omega = 0.6$  is mainly due to the inaccurate  $\theta_1^{\text{opt}}$  determined at this frequency. Future improvements on quantum hardware will enable more accurate calculation of the cost function  $L(\theta_1)$  and hence alleviate this problem.

For comparison, we also compute  $\chi(\omega)$  using DFT, the method of choice for computing dynamic polarizabilities of large molecules (3), with three popular exchange-correlation (XC) functionals (see Fig. S11). For clarity, only the results obtained from the Hartree-Fock (HF)

method, viewed as a special XC functional here, in spin-restricted (RHF) and spin-unrestricted (UHF) variants are displayed in Fig. 3C. We find that while different XC functionals give comparable results close to the FCI reference at the equilibrium, their performances deteriorate rapidly towards bond dissociation, where the occupied  $\sigma_g$  orbital and the unoccupied  $\sigma_u$  orbital become nearly degenerate. Besides, it is interesting to see that even though the symmetry-breaking UHF provides a good energy at  $R = 3R_e$ , the computed  $\chi(\omega)$  are qualitatively wrong. These results highlight the failure of DFT with approximate density functionals in computing response properties of strongly correlated systems, for which VQR may become a better alternative for large systems in future.

## UV-Vis absorption spectra of polyacenes from two-qubit simulations

Having established the feasibility of VQR on NISQ devices, we explore its potential in solving more challenging problems of potential technological importance. We exemplify this capability by simulating UV-Vis absorption spectra of polyacenes (39) made up of linearly fused benzene rings. Specifically, we simulate the first absorption band (the so-called  $^1L_a$  or  $p$  band (39)) due to the transition from the highest occupied molecular orbital (HOMO) to the lowest unoccupied molecular orbital (LUMO), which is the most relevant band for their applications as optoelectronic devices (40). As qubit resources are very limited on NISQ devices, simulating the entire molecule is currently impossible for polyacenes. To overcome this problem, we combine VQR with the complete active space (CAS) model (41) (see Fig. 4A), in which only a selected number of electrons and orbitals are treated at the FCI level. For polyacenes including naphthalene, anthracene, tetracene, and pentacene (see Fig. 4B), we choose a minimal active space composed of HOMO and LUMO with two active electrons, denoted by CAS(2e,2o). VQE and VQR are then applied to the reduced problem, for which the same experimental settings for  $H_2$  can be used. To take into account the missing dynamic electron correlation due to the active space

approximation, all the computed spectra  $\sigma_{\text{abs}}(\omega)$  are shifted by -1.9 eV estimated using perturbation theory (see Supplementary Materials). As shown in Fig. 4C, the FCI spectra reproduce the key feature of the experimental spectra for polyacenes (39), viz., the remarkable red shift as the number of rings increases. The major difference is that the simulated spectra are not vibrationally resolved, as the effects of nuclear motions are neglected, which will be taken into account in future.

We find that the VQR(raw) spectra are less accurate compared with those for H<sub>2</sub>. This is because a much smaller broadening parameter ( $\gamma = 0.01$  a.u.) is used here for a better resolution in the UV-Vis region, such that the computation of the denominator in Eq. 4 is more sensitive to noises. Even in this case, the EM strategy leads to a remarkable agreement with the FCI spectra. For naphthalene, a small artificial peak around 2.3 eV is observed in the VQR(EM) spectrum, for the same problem found for H<sub>2</sub>. For the other three molecules, the excitation energies of the first triplet states are smaller than 1.5 eV, and hence the simulated UV-Vis absorption spectra are not impaired. Although not illustrated in this work, we mention that VQR is also applicable to simulating emission spectra, provided the initial excited state is prepared on quantum computers, e.g., using the variational quantum deflation method (42). In combination with more sophisticated methods for treating dynamic correlations and vibrational effects, we expect VQR to become a useful computational tool for studying photophysics and photochemistry of molecules as qubit resources become abundant.

## **X-ray absorption spectra of CO from four-qubit simulations**

The distinct advantage of VQR for directly simulating spectra in an interested energy window without computing all the excited states below makes it very attractive for applications in X-ray spectroscopies, which are widely utilized for probing local molecular and electronic structures, but remain challenging for theoretical prediction (43, 44). We demonstrate the ca-

pability and scalability of VQR by simulating the carbon K-edge and oxygen K-edge absorption spectra of CO within a CAS(4e,3o) model using four qubits (see Fig. 2C). The active space is composed of  $\sigma_{1s_O}$ ,  $\sigma_{1s_C}$ , and  $\pi_x^*$  orbitals (see Fig. 5A), and the ground state is well-approximated by the Hartree-Fock state,  $|\Psi_0\rangle = U_0|0\rangle = |1111\rangle$  with  $U_0 = X_0X_1X_2X_3$  (see Supplementary Materials). For  $\hat{V} = \hat{x}$ , a response state can be exactly parameterized by  $|x(\theta, \phi)\rangle = U_1(\theta, \phi)|0\rangle = \cos\frac{\theta}{2}|^1\Psi_{\sigma_{1s_O}\rightarrow\pi_x^*}\rangle + \sin\frac{\theta}{2}e^{i\phi}|^1\Psi_{\sigma_{1s_C}\rightarrow\pi_x^*}\rangle$  with two free angles  $\theta$  and  $\phi$ , where  $U_1(\theta, \phi)$  is the PQC in Fig. 5B and  $|^1\Psi_{\sigma_{1s_O}\rightarrow\pi_x^*}\rangle$  ( $|^1\Psi_{\sigma_{1s_C}\rightarrow\pi_x^*}\rangle$ ) represents the singlet excited state due to the transition from the core orbital  $\sigma_{1s_O}$  ( $\sigma_{1s_C}$ ) to the unoccupied orbital  $\pi_x^*$ .

The simulated absorption spectra  $\sigma_{\text{abs}}(\omega)$  by VQR are shown in Fig. 5C. It is seen that while the VQR(raw) spectrum is almost vanishing, the improvement by EM is dramatic, giving rise to two visible absorption peaks in the VQR(EM) spectrum. Compared with the above two-qubit simulations, the deviation of the VQR(EM) spectrum from the FCI reference is larger. To better understand the discrepancy, we also measure  $\sigma_{\text{abs}}(\omega)$  at the ideal angles  $(\theta^*, \phi^*)$  at each frequency, labelled by VQR(EM\*) in Fig. 5C. The absorption spectra in the region around 500 eV are improved, where the computation of the cost function  $L(\theta, \phi)$  is prone to noises due to the proximity of the two terms (see Supplementary Materials). However, the heights of the two absorption peaks are not improved by VQR(EM\*). The comparison suggests that the larger deviation from the FCI spectrum is not due to the inaccuracy in the optimized angles, but experimental imperfections in preparation of the quantum state  $|x(\theta, \phi)\rangle$  with the quantum circuit in Fig. 5B, which makes the computation of the denominator in Eq. 4 less accurate even with the ideal angles (see Fig. S15). We verify this by characterizing the output state  $|x(\theta, \phi)\rangle$  using QST (33) at two special points  $(\theta, \phi) = (0, 0)$  and  $(\theta, \phi) = (\pi, 0)$  (see Fig. 5D), which correspond to  $|^1\Psi_{\sigma_{1s_O}\rightarrow\pi_x^*}\rangle$  and  $|^1\Psi_{\sigma_{1s_C}\rightarrow\pi_x^*}\rangle$ , respectively. The fidelity  $F(\rho_{\text{exp}}, |\Psi\rangle)$  between an experimental state  $\rho_{\text{exp}}$  and an ideal state  $|\Psi\rangle$  is 0.783 (0.791) for  $|^1\Psi_{\sigma_{1s_O}\rightarrow\pi_x^*}\rangle$  ( $|^1\Psi_{\sigma_{1s_C}\rightarrow\pi_x^*}\rangle$ ),

which is lower than that for the response state at the peak position of  $\text{Im}\chi(\omega)$  for  $\text{H}_2$  at  $R = R_e$  in Fig. 3E. The lowering of fidelity is attributed to the doubling of the number of  $\sqrt{\text{iSWAP}}$  gates and the lowering of gate fidelities (see Materials and Methods).

Note that even though the peak height given by VQR(EM) is not ideal, the more important peak positions, which determine core excitation energies, are still reasonably good. The remaining discrepancy with the experimental core excitation energies obtained from high-resolution photoabsorption spectra (45, 46) can be improved by employing a larger active space and a better basis set in future. These multi-qubit experimental results demonstrate that VQR can potentially scale up to larger systems on improved quantum hardware with higher two-qubit gate fidelities.

## Discussion

Compared with classical computers, quantum computers naturally have a storage advantage in representing quantum states with a computational resource that grows only linearly instead of exponentially with the molecular size. However, the presence of noises in NISQ devices makes the effective use of their computational power nontrivial, and necessitates a careful algorithm design. The proposed VQR approach circumvents the requirement of deep quantum circuits in previous quantum algorithms (22–25), and hence enables the first ever quantum simulation of molecular electronic spectroscopy on a superconducting quantum processor. In particular, we demonstrate a feasible and universal algorithmic primitive for solving the linear response equation on NISQ devices, which can be easily extended to simulate other properties such as Green’s functions (47) and nonlinear response properties (25). Our simulation results suggest that a potential quantum computational advantage over standard methods on classical computers may exist in the strong electron correlation regime, for which VQR may provide an accurate and efficient solution when combined with the CAS model and EM techniques. Important appli-

cations in this category include simulating spectra for challenging systems involving transition metals such as high-temperature superconductors. For large systems, such advantage also crucially hinges on the variational ansatz (18, 19, 34, 48) and the magnitude of noises in multi-qubit cases, which need to be carefully studied in future. We emphasize that the VQR approach is not limited to superconducting devices, but also applicable to other platforms such as trapped-ion quantum computers (36, 49). With the advent of more powerful large-scale quantum processors with lower error rates, wide application of this general approach can be anticipated in simulating response properties of more complex molecules and condense-phase systems in the near future.

## Materials and Methods

**Device information** The qubits ( $Q_3$ ,  $Q_6$ ,  $Q_{13}$ ,  $Q_{14}$ , and  $Q_{20}$ ) used in our experiments are selected based on the decoherence time and the coupling strength  $g_i$  between a qubit  $Q_i$  and the bus resonator. Longer decoherence time will enable more accurate basic qubit operations, while larger  $g_i$  can improve the effective coupling strength between qubits mediated by the bus resonator, and hence reduces the characteristic time of the two-qubit gate. Qubit frequencies are carefully arranged to minimize unwanted interactions and crosstalk errors among qubits during single-qubit operations. Each qubit has its own flux bias line for Z rotations  $Z_\theta = e^{-i\frac{\theta}{2}Z}$ , which are realized by amplitude-adjustable Z square pulses with a width of 20 ns. The four qubits ( $Q_3$ ,  $Q_6$ ,  $Q_{13}$ , and  $Q_{20}$ ) have their own microwave control lines for implementing XY rotations ( $X_\theta = e^{-i\frac{\theta}{2}X}$  or  $Y_\theta = e^{-i\frac{\theta}{2}Y}$ ), while for the qubit  $Q_{14}$  the Z-control line is shared by XY and Z signals (see Fig. 2a), which are combined at room temperature by a directional coupler. Each qubit is dispersively coupled to its own readout resonator for measuring qubit states, and all the qubits can be measured simultaneously using the frequency-domain multiplexing technique. The  $\sqrt{i}$ SWAP gate is generated by tuning the involved qubits on-resonance but detuned from

the bus resonator in frequency after certain evolution time  $t_{\sqrt{\text{iSWAP}}}$  (see Supplementary Section 2.3). Two-qubit gate fidelities characterized by quantum process tomography are 0.9806, 0.9766, 0.9679, and 0.9508 for Q<sub>14</sub>-Q<sub>20</sub>, Q<sub>3</sub>-Q<sub>6</sub>, Q<sub>3</sub>-Q<sub>13</sub>, and Q<sub>6</sub>-Q<sub>20</sub>, respectively. More detailed information about the device and experimental setup can be found in Supplementary Materials.

**Two-qubit simulations for H<sub>2</sub> and polyacenes** For H<sub>2</sub> in the STO-3G basis, the Bravyi-Kitaev mapping (29, 30) with the  $Z_2$  reduction (50) leads to a mapping of occupation number vectors (ONVs) shown in Fig. 2b, i.e.,  $|n_0 n_1 n_2 n_3\rangle = |n_{\sigma_g^\alpha} n_{\sigma_u^\alpha} n_{\sigma_g^\beta} n_{\sigma_u^\beta}\rangle \rightarrow |q_0 q_1\rangle = |n_0 n_2\rangle$ , where  $n_i \in \{0, 1\}$  is the occupation number of a spin-orbital,  $q_i \in \{0, 1\}$  is the status of a qubit, and the symbol  $g$  ( $u$ ) refers to the RHF molecular orbital with gerade (ungerade) symmetry. The resulting Hamiltonian and perturbation operator are  $\hat{H}_0 = h_0 I + h_1 Z_0 + h_2 Z_1 + h_3 Z_0 Z_1 + h_4 X_0 X_1$  and  $\hat{V} = v_0 (X_0 + X_1)$ , respectively, where the coefficients  $h_i$  and  $v_0$  are obtained using the PySCF package (51). The quantum circuit in Fig. 3a gives a parameterized quantum state  $|\Psi(\theta_0)\rangle = U_0(\theta_0)|0\rangle = \cos \frac{\theta_0}{2}|11\rangle + \sin \frac{\theta_0}{2}|00\rangle$  up to an irrelevant global phase, while that in Fig. 3b leads to  $|x(\theta_1)\rangle = U_1(\theta_1)|0\rangle = \cos \frac{\theta_1}{2}|10\rangle + \sin \frac{\theta_1}{2}|01\rangle$  up to a global phase. The spatial symmetry projectors used in EM are  $\mathcal{P}_g = |00\rangle\langle 00| + |11\rangle\langle 11| = \frac{1}{2}(I + Z_0 Z_1)$  and  $\mathcal{P}_u = |01\rangle\langle 01| + |10\rangle\langle 10| = \frac{1}{2}(I - Z_0 Z_1)$  for  $|\Psi(\theta_0)\rangle$  and  $|x(\theta_1)\rangle$ , respectively. The CAS(2e,2o) model for polyacenes can be described in the same settings. Details of the quantum circuit for computing  $|\langle \Psi_0 | \hat{V}^\dagger \hat{A}(\omega) | x \rangle|^2$ , formulae for EM, measured results for individual terms, and optimizations for  $L(\theta_1)$  can be found in Supplementary Materials.

**Four-qubit simulations for CO** For the CAS(4e,3o) model of CO, the parity mapping (30) with the  $Z_2$  reduction (29) leads to a mapping of ONVs shown in Fig. 2c, i.e.,  $|n_0 n_1 n_2 n_3 n_4 n_5\rangle = |n_{\sigma_{1s_O}^\alpha} n_{\pi_x^{\alpha*}} n_{\sigma_{1s_C}^\alpha} n_{\sigma_{1s_O}^\beta} n_{\pi_x^{\beta*}} n_{\sigma_{1s_C}^\beta}\rangle \rightarrow |q_0 q_1 q_2 q_3\rangle = |n_0(n_0 + n_1 \bmod 2)n_3(n_3 + n_4 \bmod 2)\rangle$ . Consequently, the Hartree-Fock state becomes  $|\Psi_0\rangle = |1111\rangle = U_0|0\rangle$  with  $U_0 = X_0 X_1 X_2 X_3$ , and the singlet excited states are  $|^1\Psi_{\sigma_{1s_O} \rightarrow \pi_x^*}\rangle = \frac{1}{\sqrt{2}}(|0111\rangle + |1101\rangle)$  and  $|^1\Psi_{\sigma_{1s_C} \rightarrow \pi_x^*}\rangle =$

$\frac{1}{\sqrt{2}}(|1011\rangle + |1110\rangle)$ , respectively. The active space Hamiltonian can be well-approximated by  $\hat{H}_0 = \sum_{k=0}^{15} h_k P_k$  with  $P_k \in \{I, Z\}^{\otimes 4}$ , and the perturbation operator is  $\hat{V} = v_0(X_0 + X_2) + v_1(X_1 + X_3)$ . The spin symmetry projector used in EM for  $|x(\theta, \phi)\rangle$  is  $\mathcal{P}_S = \mathcal{P}_S^O + \mathcal{P}_S^C$  with  $\mathcal{P}_S^O = \frac{1}{2}(|0111\rangle + |1101\rangle)(\langle 0111| + \langle 1101|) = \frac{1}{16}(I - Z_0 Z_2 + X_0 X_2 + Y_0 Y_2)(I - Z_1)(I - Z_3)$  and  $\mathcal{P}_S^C = \frac{1}{2}(|1011\rangle + |1110\rangle)(\langle 1011| + \langle 1110|) = \frac{1}{16}(I - Z_1 Z_3 + X_1 X_3 + Y_1 Y_3)(I - Z_0)(I - Z_2)$ . Details of the quantum circuits for computing  $|\langle \Psi_0 | \hat{V}^\dagger \hat{A}(\omega) | x \rangle|^2$ , formulae for EM, landscapes of individual terms in  $L(\theta, \phi)$ , and optimization results can be found in Supplementary Materials.

## References

1. N. Marzari, A. Ferretti, C. Wolverton, Electronic-structure methods for materials design. *Nat. Mater.* **20**, 736–749 (2021).
2. T. Helgaker, S. Coriani, P. Jørgensen, K. Kristensen, J. Olsen, K. Ruud, Recent advances in wave function-based methods of molecular-property calculations. *Chem. Rev.* **112**, 543–631 (2012).
3. P. Norman, K. Ruud, T. Saue, *Principles and practices of molecular properties: Theory, modeling, and simulations* (John Wiley & Sons, 2018).
4. A. J. Cohen, P. Mori-Sánchez, W. Yang, Insights into current limitations of density functional theory. *Science* **321**, 792–794 (2008).
5. R. P. Feynman, Simulating physics with computers. *Int. J. Theor. Phys.* **21**, 467–488 (1982).
6. F. Arute, K. Arya, R. Babbush, D. Bacon, J. C. Bardin, R. Barends, R. Biswas, S. Boixo, F. G. S. L. Brandao, D. A. Buell, B. Burkett, Y. Chen, Z. Chen, B. Chiaro, R. Collins, W. Courtney, A. Dunsworth, E. Farhi, B. Foxen, A. Fowler, C. Gidney, M. Giustina, R. Graff, K. Guerin, S. Habegger, M. P. Harrigan, M. J. Hartmann, A. Ho, M. Hoffmann,

- T. Huang, T. S. Humble, S. V. Isakov, E. Jeffrey, Z. Jiang, D. Kafri, K. Kechedzhi, J. Kelly, P. V. Klimov, S. Knysh, A. Korotkov, F. Kostritsa, D. Landhuis, M. Lindmark, E. Lucero, D. Lyakh, S. Mandr, J. R. McClean, M. McEwen, A. Megrant, X. Mi, K. Michielsen, M. Mohseni, J. Mutus, O. Naaman, M. Neeley, C. Neill, M. Y. Niu, E. Ostby, A. Petukhov, J. C. Platt, C. Quintana, E. G. Rieffel, P. Roushan, N. C. Rubin, D. Sank, K. J. Satzinger, V. Smelyanskiy, K. J. Sung, M. D. Trevithick, A. Vainsencher, B. Villalonga, T. White, Z. J. Yao, P. Yeh, A. Zalcman, H. Neven, J. M. Martinis, Quantum supremacy using a programmable superconducting processor. *Nature* **574**, 505–510 (2019).
7. Y. Wu, W.-S. Bao, S. Cao, F. Chen, M.-C. Chen, X. Chen, T.-H. Chung, H. Deng, Y. Du, D. Fan, M. Gong, C. Guo, C. Guo, S. Guo, L. Han, L. Hong, H.-L. Huang, Y.-H. Huo, L. Li, N. Li, S. Li, Y. Li, F. Liang, C. Lin, J. Lin, H. Qian, D. Qiao, H. Rong, H. Su, L. Sun, L. Wang, S. Wang, D. Wu, Y. Xu, K. Yan, W. Yang, Y. Yang, Y. Ye, J. Yin, C. Ying, J. Yu, C. Zha, C. Zhang, H. Zhang, K. Zhang, Y. Zhang, H. Zhao, Y. Zhao, L. Zhou, Q. Zhu, C.-Y. Lu, C.-Z. Peng, X. Zhu, J.-W. Pan, Strong quantum computational advantage using a superconducting quantum processor. *Phys. Rev. Lett.* **127**, 180501 (2021).
  8. Y. Cao, J. Romero, J. P. Olson, M. Degroote, P. D. Johnson, M. Kieferová, I. D. Kivlichan, T. Menke, B. Peropadre, N. P. Sawaya, S. Sim, L. Veis, A. Aspuru-Guzik, Quantum chemistry in the age of quantum computing. *Chem. Rev.* **119**, 10856–10915 (2019).
  9. S. McArdle, S. Endo, A. Aspuru-Guzik, S. C. Benjamin, X. Yuan, Quantum computational chemistry. *Rev. Mod. Phys.* **92**, 015003 (2020).
  10. B. Bauer, S. Bravyi, M. Motta, G. K.-L. Chan, Quantum algorithms for quantum chemistry and quantum materials science. *Chem. Rev.* **120**, 12685–12717 (2020).
  11. J. Preskill, Quantum computing in the nisq era and beyond. *Quantum* **2**, 79 (2018).

12. M. Reiher, N. Wiebe, K. M. Svore, D. Wecker, M. Troyer, Elucidating reaction mechanisms on quantum computers. *Proc. Natl. Acad. Sci. U.S.A.* **114**, 7555–7560 (2017).
13. Z. Li, J. Li, N. S. Dattani, C. Umrigar, G. K.-L. Chan, The electronic complexity of the ground-state of the fmo cofactor of nitrogenase as relevant to quantum simulations. *J. Chem. Phys.* **150**, 024302 (2019).
14. M. Motta, E. Ye, J. R. McClean, Z. Li, A. J. Minnich, R. Babbush, G. K.-L. Chan, Low rank representations for quantum simulation of electronic structure. *npj Quantum Inf.* **7**, 1–7 (2021).
15. A. Aspuru-Guzik, A. D. Dutoi, P. J. Love, M. Head-Gordon, Simulated quantum computation of molecular energies. *Science* **309**, 1704–1707 (2005).
16. B. P. Lanyon, J. D. Whitfield, G. G. Gillett, M. E. Goggin, M. P. Almeida, I. Kassal, J. D. Biamonte, M. Mohseni, B. J. Powell, M. Barbieri, A. Aspuru-Guzik, A. G. White, Towards quantum chemistry on a quantum computer. *Nat. Chem.* **2**, 106-111 (2010).
17. J. D. Whitfield, J. Biamonte, A. Aspuru-Guzik, Simulation of electronic structure hamiltonians using quantum computers. *Mol. Phys.* **109**, 735–750 (2011).
18. A. Peruzzo, J. McClean, P. Shadbolt, M.-H. Yung, X.-Q. Zhou, P. J. Love, A. Aspuru-Guzik, J. L. O’Brien, A variational eigenvalue solver on a photonic quantum processor. *Nat. Commun.* **5**, 4213 (2014).
19. J. R. McClean, J. Romero, R. Babbush, A. Aspuru-Guzik, The theory of variational hybrid quantum-classical algorithms. *New J. Phys.* **18**, 023023 (2016).

20. M. Cerezo, A. Arrasmith, R. Babbush, S. C. Benjamin, S. Endo, K. Fujii, J. R. McClean, K. Mitarai, X. Yuan, L. Cincio, P. J. Coles, Variational quantum algorithms. *Nature Reviews Physics* **3**, 625–644 (2021).
21. J. E. Rice, T. P. Gujarati, M. Motta, T. Y. Takeshita, E. Lee, J. A. Latone, J. M. Garcia, Quantum computation of dominant products in lithium–sulfur batteries. *J. Chem. Phys.* **154**, 134115 (2021).
22. R. Somma, G. Ortiz, J. E. Gubernatis, E. Knill, R. Laflamme, Simulating physical phenomena by quantum networks. *Phys. Rev. A* **65**, 042323 (2002).
23. A. Chiesa, F. Tacchino, M. Grossi, P. Santini, I. Tavernelli, D. Gerace, S. Carretta, Quantum hardware simulating four-dimensional inelastic neutron scattering. *Nat. Phys.* **15**, 455–459 (2019).
24. S.-N. Sun, M. Motta, R. N. Tazhigulov, A. T. Tan, G. K.-L. Chan, A. J. Minnich, Quantum computation of finite-temperature static and dynamical properties of spin systems using quantum imaginary time evolution. *PRX Quantum* **2**, 010317 (2021).
25. X. Cai, W.-H. Fang, H. Fan, Z. Li, Quantum computation of molecular response properties. *Phys. Rev. Res.* **2**, 033324 (2020).
26. A. W. Harrow, A. Hassidim, S. Lloyd, Quantum algorithm for linear systems of equations. *Phys. Rev. Lett.* **103**, 150502 (2009).
27. C. Song, K. Xu, H. Li, Y.-R. Zhang, X. Zhang, W. Liu, Q. Guo, Z. Wang, W. Ren, J. Hao, H. Feng, H. Fan, D. Zheng, D.-W. Wang, H. Wang, S.-Y. Zhu, Generation of multicomponent atomic schrödinger cat states of up to 20 qubits. *Science* **365**, 574–577 (2019).

28. K. Haung, Z.-A. Wang, C. Song, K. Xu, H. Li, Z. Wang, Q. Guo, Z. Song, Z.-B. Liu, D. Zheng, D.-L. Deng, H. Wang, J.-G. Tian, H. Fan, Quantum generative adversarial networks with multiple superconducting qubits. *npj Quantum Inf.* **5**, 1-5 (2021).
29. S. Bravyi, A. Y. Kitaev, Fermionic quantum computation. *Ann. Phys.* **298**, 210–226 (2002).
30. J. T. Seeley, M. J. Richard, P. J. Love, The bravyi-kitaev transformation for quantum computation of electronic structure. *J. Chem. Phys.* **137**, 224109 (2012).
31. X. Xu, J. Sun, S. Endo, Y. Li, S. C. Benjamin, X. Yuan, Variational algorithms for linear algebra. *arXiv preprint arXiv:1909.03898* (2019).
32. C. Bravo-Prieto, R. LaRose, M. Cerezo, Y. Subasi, L. Cincio, P. J. Coles, Variational quantum linear solver. *arXiv preprint arXiv:1909.05820* (2019).
33. M. A. Nielsen, I. L. Chuang, *Quantum computation and quantum information* (Cambridge University Press, 2010).
34. A. Kandala, A. Mezzacapo, K. Temme, M. Takita, M. Brink, J. M. Chow, J. M. Gambetta, Hardware-efficient variational quantum eigensolver for small molecules and quantum magnets. *Nature* **549**, 242 (2017).
35. P. J. J. O’Malley, R. Babbush, I. D. Kivlichan, J. Romero, J. R. McClean, R. Barends, J. Kelly, P. Roushan, A. Tranter, N. Ding, B. Campbell, Y. Chen, Z. Chen, B. Chiaro, A. Dunsworth, A. G. Fowler, E. Jeffrey, E. Lucero, A. Megrant, J. Y. Mutus, M. Neeley, C. Neill, C. Quintana, D. Sank, A. Vainsencher, J. Wenner, T. C. White, P. V. Coveney, P. J. Love, H. Neven, A. Aspuru-Guzik, J. M. Martinis, Scalable quantum simulation of molecular energies. *Phys. Rev. X* **6**, 031007 (2016).

36. C. Hempel, C. Maier, J. Romero, J. McClean, T. Monz, H. Shen, P. Jurcevic, B. P. Lanyon, P. Love, R. Babbush, A. Aspuru-Guzik, R. Blatt, C. F. Roos, Quantum chemistry calculations on a trapped-ion quantum simulator. *Phys. Rev. X* **8**, 031022 (2018).
37. R. Sagastizabal, X. Bonet-Monroig, M. Singh, M. A. Rol, C. Bultink, X. Fu, C. Price, V. Ostroukh, N. Muthusubramanian, A. Bruno, M. Beekman, N. Haider, T. E. O'Brien, L. DiCarlo, Experimental error mitigation via symmetry verification in a variational quantum eigensolver. *Phys. Rev. A* **100**, 010302 (2019).
38. K. P. Huber, G. Herzberg, *Molecular Spectra and Molecular Structure IV. Constants of Diatomic Molecules* (Van Nostrand Reinhold, New York, 1979).
39. E. Clar, R. Schoental, *Polycyclic hydrocarbons*, vol. 1 (Springer, 1964).
40. J. E. Anthony, Functionalized acenes and heteroacenes for organic electronics. *Chem. Rev.* **106**, 5028–5048 (2006).
41. P. G. Szalay, T. Muller, G. Gidofalvi, H. Lischka, R. Shepard, Multiconfiguration self-consistent field and multireference configuration interaction methods and applications. *Chem. Rev.* **112**, 108–181 (2012).
42. O. Higgott, D. Wang, S. Brierley, Variational quantum computation of excited states. *Quantum* **3**, 156 (2019).
43. P. Norman, A. Dreuw, Simulating x-ray spectroscopies and calculating core-excited states of molecules. *Chem. Rev.* **118**, 7208–7248 (2018).
44. N. A. Besley, Modeling of the spectroscopy of core electrons with density functional theory. *Wiley Interdiscip. Rev. Comput. Mol. Sci.* p. e1527 (2021).

45. Y. Ma, C. Chen, G. Meigs, K. Randall, F. Sette, High-resolution k-shell photoabsorption measurements of simple molecules. *Phys. Rev. A* **44**, 1848 (1991).
46. R. Püttner, I. Dominguez, T. Morgan, C. Cisneros, R. Fink, E. Rotenberg, T. Warwick, M. Domke, G. Kaindl, A. Schlachter, Vibrationally resolved o 1s core-excitation spectra of co and no. *Phys. Rev. A* **59**, 3415 (1999).
47. H. Chen, M. Nusspickel, J. Tilly, G. H. Booth, Variational quantum eigensolver for dynamic correlation functions. *Phys. Rev. A* **104**, 032405 (2021).
48. J. R. McClean, S. Boixo, V. N. Smelyanskiy, R. Babbush, H. Neven, Barren plateaus in quantum neural network training landscapes. *Nat. Commun.* **9**, 1–6 (2018).
49. Y. Nam, J.-S. Chen, N. C. Pienti, K. Wright, C. Delaney, D. Maslov, K. R. Brown, S. Allen, J. M. Amini, J. Apisdorf, K. M. Beck, A. Blinov, V. Chaplin, M. Chmielewski, C. Collins, S. Debnath, K. M. Hudek, A. M. Ducore, M. Keesan, S. M. Kreikemeier, J. Mizrahi, P. Solomon, M. Williams, J. D. Wong-Campos, D. Moehring, C. Monroe, J. Kim, Ground-state energy estimation of the water molecule on a trapped-ion quantum computer. *npj Quantum Inf.* **6**, 33 (2020).
50. S. Bravyi, J. M. Gambetta, A. Mezzacapo, K. Temme, Tapering off qubits to simulate fermionic hamiltonians. *arXiv preprint arXiv:1701.08213* (2017).
51. Q. Sun, T. C. Berkelbach, N. S. Blunt, G. H. Booth, S. Guo, Z. Li, J. Liu, J. D. McClain, E. R. Sayfutyarova, S. Sharma, S. Wouters, G. K.-L. Chan, Pyscf: the python-based simulations of chemistry framework. *Wiley Interdiscip. Rev. Comput. Mol. Sci.* **8**, e1340 (2018).
52. T. Helgaker, P. Jørgensen, J. Olsen, *Molecular electronic-structure theory* (John Wiley & Sons, 2014).

53. P. Jordan, E. Wigner, About the pauli exclusion principle. *Z. Phys.* **47**, 631 (1928).
54. W. J. Huggins, J. R. McClean, N. C. Rubin, Z. Jiang, N. Wiebe, K. B. Whaley, R. Babbush, Efficient and noise resilient measurements for quantum chemistry on near-term quantum computers. *npj Quantum Inf.* **7**, 1–9 (2021).
55. R. W. Boyd, *Nonlinear optics* (Elsevier, 2003).
56. Y. Ibe, Y. O. Nakagawa, N. Earnest, T. Yamamoto, K. Mitarai, Q. Gao, T. Kobayashi, Calculating transition amplitudes by variational quantum deflation. *arXiv preprint arXiv:2002.11724* (2020).
57. F. Motzoi, J. M. Gambetta, P. Rebentrost, F. K. Wilhelm, Simple pulses for elimination of leakage in weakly nonlinear qubits. *Phys. Rev. Lett.* **103**, 110501 (2009).
58. Y. Zheng, C. Song, M.-C. Chen, B. Xia, W. Liu, Q. Guo, L. Zhang, D. Xu, H. Keqiang, Y. Wu, Z. Yan, D. Zheng, L. Lu, J.-W. Pan, H. Wang, C.-Y. Lu, X. Zhu, Solving systems of linear equations with a superconducting quantum processor. *Phys. Rev. Lett.* **118**, 210504 (2017).
59. C. Song, K. Xu, W. Liu, C.-P. Zheng, S.-B. Zheng, D. Hui, Q. Xie, K. Haung, Q. Guo, L. Zhang, P. Zhang, D. Xu, D. Zheng, X. Zhu, H. Wang, Y.-A. Chen, C.-Y. Lu, S. Han, J.-W. Pan, 10-qubit entanglement and parallel logic operations with a superconducting circuit. *Phys. Rev. Lett.* **119**, 180511 (2017).
60. I. L. Chuang, M. A. Nielsen, Prescription for experimental determination of the dynamics of a quantum black box. *J. Mod. Opt.* **44**, 2455 (1997).
61. Q. Guo, S.-B. Zheng, J. Wang, C. Song, P. Zhang, K. Li, W. Liu, H. Deng, K. Huang, D. Zheng, X. Zhu, H. Wang, C.-Y. Lu, J.-W. Pan, Dephasing-insensitive quantum infor-

- mation storage and processing with superconducting qubits. *Phys. Rev. Lett.* **121**, 130501 (2018).
62. S. Trotzky, P. Cheinet, S. Fölling, M. Feld, U. Schnorrberger, A. M. Rey, A. Polkovnikov, E. A. Demler, M. D. Lukin, I. Bloch, Time-resolved observation and control of superexchange interactions with ultracold atoms in optical lattices. *Science* **319**, 295–299 (2008).
63. A. D. Becke, Becke’s three parameter hybrid method using the lyp correlation functional. *J. Chem. Phys* **98**, 5648–5652 (1993).
64. P. J. Stephens, F. J. Devlin, C. F. Chabalowski, M. J. Frisch, Ab initio calculation of vibrational absorption and circular dichroism spectra using density functional force fields. *J. Phys. Chem.* **98**, 11623–11627 (1994).
65. C. Angeli, R. Cimiraglia, S. Evangelisti, T. Leininger, J.-P. Malrieu, Introduction of n-electron valence states for multireference perturbation theory. *J. Chem. Phys.* **114**, 10252–10264 (2001).

## Acknowledgments

### Funding

This work was supported by the National Natural Science Foundation of China (Grant Nos. 21973003, 21688102, T2121001, 11934018, 11904393, 92065114 and 12174207), the Strategic Priority Research Program of Chinese Academy of Sciences (Grant Nos. XDB28000000) and the Beijing Natural Science Foundation (Z2000009).

### Author contributions

Z.L. and X.C. conceived the research. K.H. and H.L. conducted the experiments, supervised by Z.B.L., K.X. and F.H.. K.H., X.C., Z.Y.G., H.L. and R.H. performed the numerical simulations.

K.H., H.L., T.L., Y.S. and C.C. participated in the development of measurement and control system. H.K.L. and D.Z. fabricated the device. K.H., X.C., H.L., K.X., Z.L., H.F. and W.-H.F. wrote the manuscript. All authors contributed to the discussion of the results and development of the manuscript.

### **Competing interests**

The authors declare that they have no competing interests.

### **Data and materials availability**

All data needed to evaluate the conclusions in the paper are present in the paper and/or the Supplementary Materials. Additional data related to this paper may be requested from the authors.

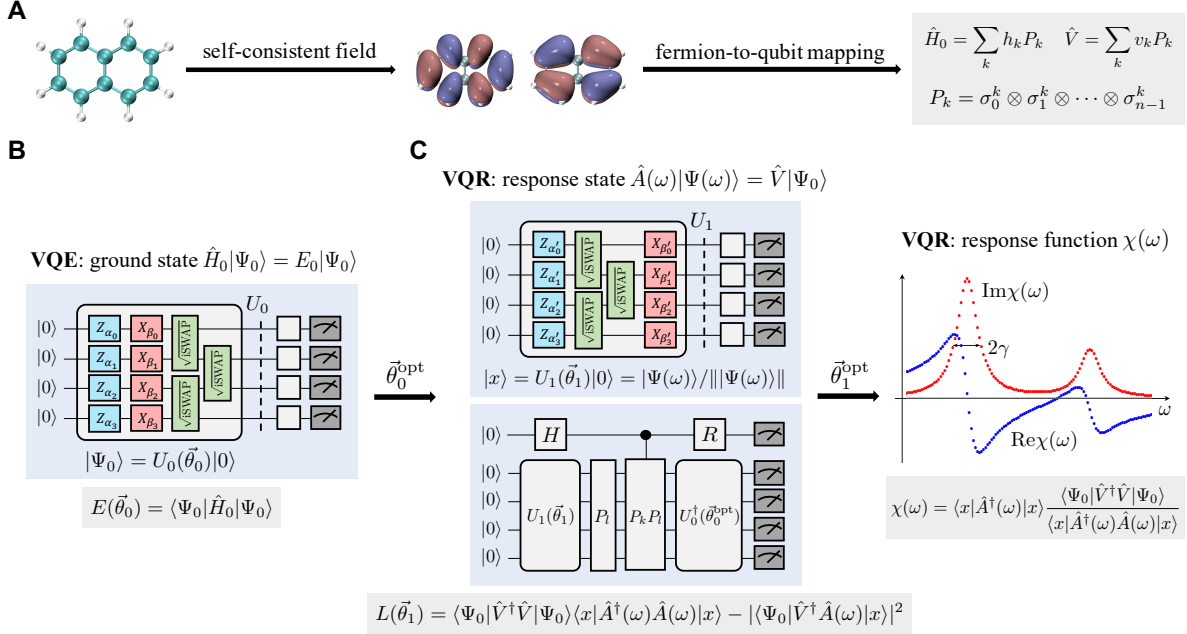


**Fig. 1. Quantum computational strategy for linear response properties of molecules.** (A) Preprocessing step on classical computers. An initial set of molecular orbitals is first prepared for a given molecule using self-consistent field calculations, and then a fermion-to-qubit mapping is employed to transform  $\hat{H}_0$  and  $\hat{V}$  to their counterparts for  $n$  qubits as linear combinations of Pauli terms  $P_k$ . (B) VQE for the ground state. A wavefunction ansatz is defined for  $|\Psi_0\rangle = U_0(\vec{\theta}_0)|0\rangle$ , where  $U_0(\vec{\theta}_0)$  is a PQC with a set of variational parameters  $\vec{\theta}_0$ , usually composed of parameterized single-qubit rotations (e.g.,  $Z_{\alpha_k}$  and  $X_{\beta_i}$ ) and two-qubit entangling gates (e.g.,  $\sqrt{i}$ SWAP). The optimized parameters  $\vec{\theta}_0^{\text{opt}}$  are found by minimizing the energy function  $E(\vec{\theta}_0)$  on classical computers, with the necessary expectation values  $\langle \Psi_0 | P_k | \Psi_0 \rangle$  computed using the presented quantum circuit on quantum computers. For each  $P_k$ , appropriate single-qubit rotations ( $I$ ,  $X_{-\pi/2}$  or  $Y_{\pi/2}$ ) are added for polarizations along different axes before measurements. (C) VQR for linear response properties. Given a frequency  $\omega$  and a broadening parameter  $\gamma$  as input, the linear response equation is first solved by minimizing a cost function  $L(\vec{\theta}_1)$  with a PQC for the normalized response state  $|x\rangle$ . The term  $\langle x | \hat{A}^\dagger(\omega) \hat{A}(\omega) | x \rangle$  is computed using the upper quantum circuit in a similar way as the energy, and the cross term  $|\langle \Psi_0 | \hat{V}^\dagger \hat{A}(\omega) | x \rangle|^2$  can be evaluated using the lower quantum circuit (see Supplementary Materials). Once  $\vec{\theta}_1^{\text{opt}}$  is obtained at the specific  $\omega$ , the response function  $\chi(\omega)$  is computed by measuring expectation values in Eq. 4 on quantum computers.

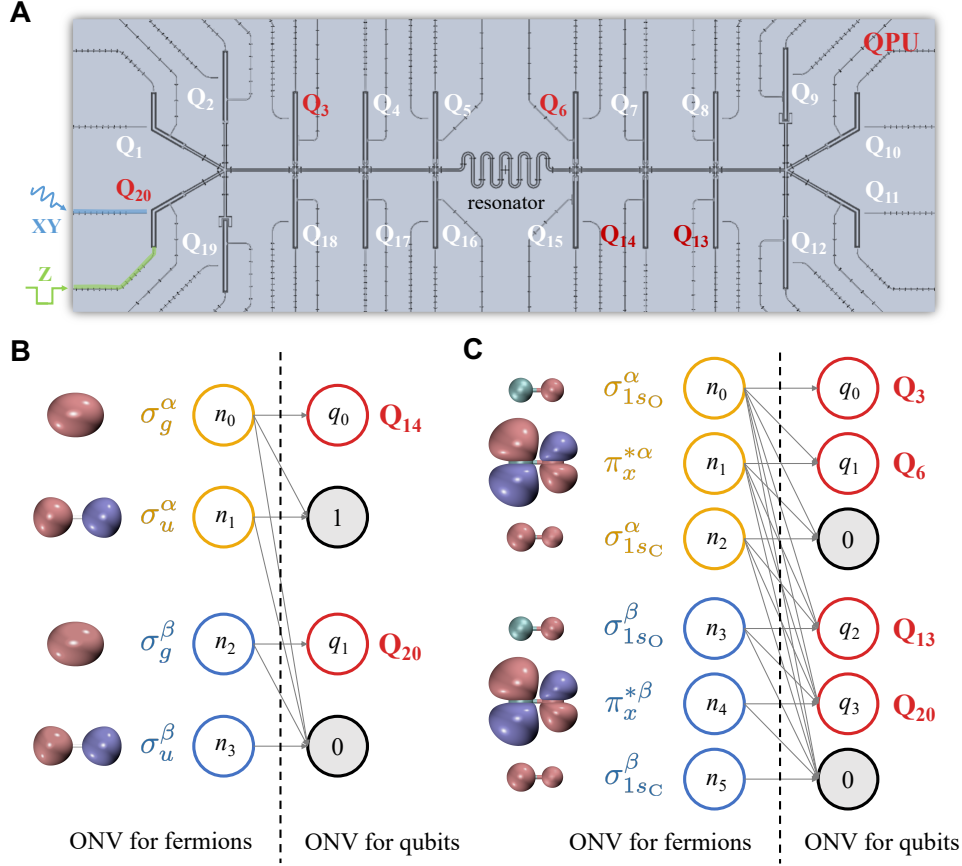


**Fig. 2. Quantum processor unit (QPU) and fermion-to-qubit mappings.** (A) False-color optical micrograph of the 20-qubit superconducting quantum device, with qubits used in experiments (red), unused qubits (white), the bus resonator (black), qubit XY-control lines (blue), and Z-control lines (green) highlighted. (B) The Bravyi-Kitaev mapping (29, 30) with the  $Z_2$  reduction (50) used in the simulations of  $H_2$  in a minimal basis set and polyacenes within a CAS(2e,2o) model for transforming the occupation number vectors (ONVs) for fermions  $|n_0 n_1 n_2 n_3\rangle = |n_{\sigma_g^\alpha} n_{\sigma_u^\alpha} n_{\sigma_g^\beta} n_{\sigma_u^\beta}\rangle$  ( $n \in \{0, 1\}$ ) to the ONVs for two qubits  $|q_0 q_1\rangle = |n_0 n_2\rangle$ . (C) The parity mapping (30) with the  $Z_2$  reduction (50) used in the simulation of CO within a CAS(4e,3o) model for transforming the ONVs for fermions  $|n_0 n_1 n_2 n_3 n_4 n_5\rangle = |n_{\sigma_{1sO}^\alpha} n_{\pi_x^{*\alpha}} n_{\sigma_{1sC}^\alpha} n_{\sigma_{1sO}^\beta} n_{\pi_x^{*\beta}} n_{\sigma_{1sC}^\beta}\rangle$  to the ONVs for four qubits  $|q_0 q_1 q_2 q_3\rangle = |n_0(n_0 + n_1 \bmod 2) n_3(n_3 + n_4 \bmod 2)\rangle$ . The grey arrows going into the same qubit indicate a sum of the input occupation numbers modulo two. In both (B) and (C), the conservations of the total number of electrons and the spin projection lead to two reducible qubits (grey circles) with constant status (referred as the  $Z_2$  reduction).

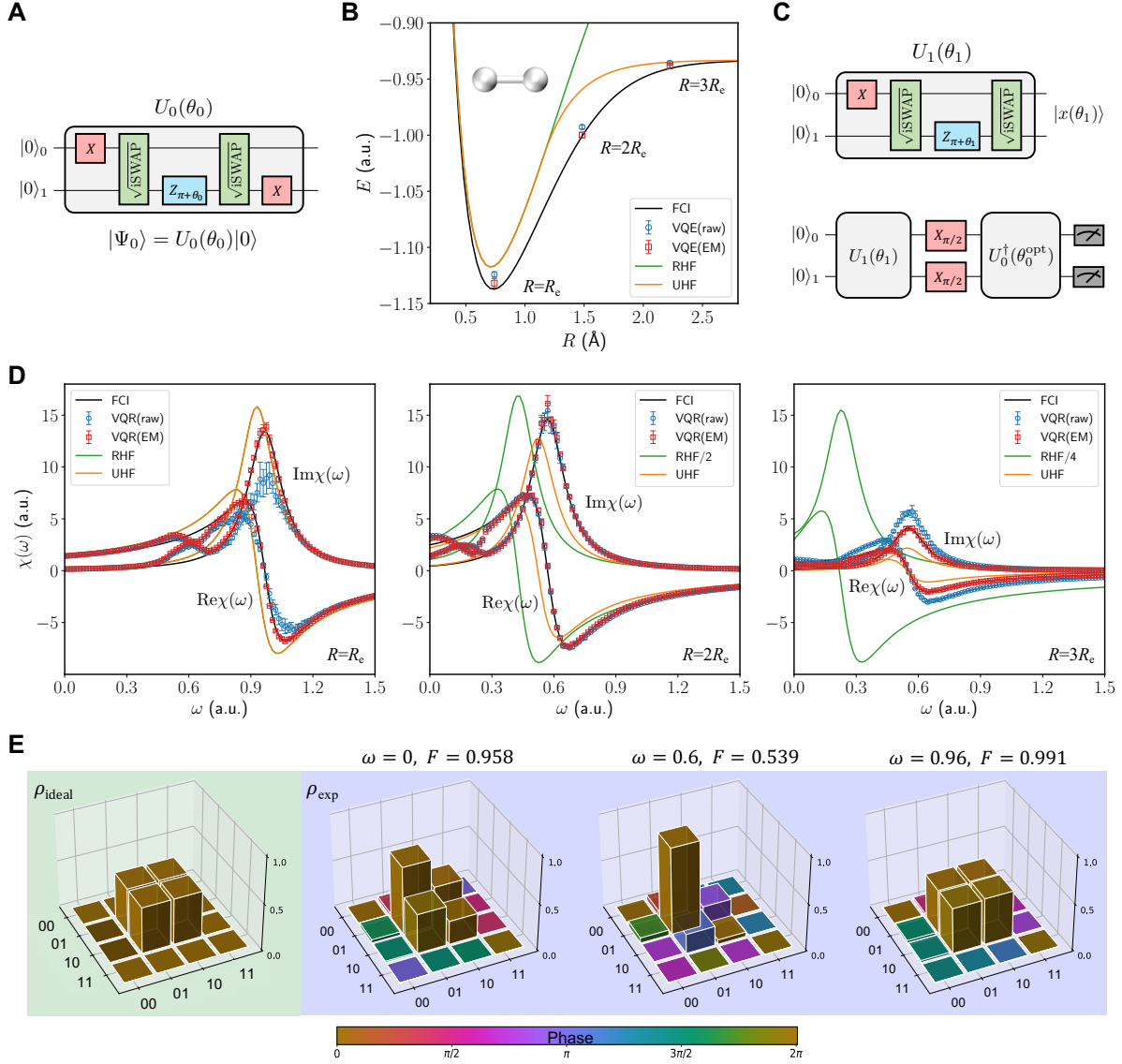


**Fig. 3. Ground-state energies and dipole polarizabilities of  $H_2$  from two-qubit simulations.** (A) PQC for the ground state  $|\Psi_0(\theta_0)\rangle$  in VQE. (B) Ground-state energies obtained by VQE (blue circles for raw results and red squares for error mitigated results) at three bond distances, i.e.,  $R_e$  (the experimental equilibrium bond distance),  $2R_e$ , and  $3R_e$ . The potential energy curves obtained from FCI (black), RHF (green) and UHF (orange) are also displayed for comparison. (C) PQC for the response state  $|x(\theta_1)\rangle$  in VQR (upper) and the quantum circuit used for evaluating the cross term  $|\langle \Psi_0 | \hat{V}^\dagger \hat{A}(\omega) | x \rangle|^2$  (lower). (D) Real and imaginary parts of  $\chi(\omega)$  computed with  $\gamma = 0.1$  a.u. at three different geometries. Note that the RHF spectrum coincides with the UHF spectrum at  $R = R_e$ , while those at  $R = 2R_e$  and  $R = 3R_e$  are scaled by  $1/2$  and  $1/4$ , respectively, in order to fit into the same figure. (E) Experimental density matrices  $\rho_{\text{exp}}$  of response states characterized by QST at three representative frequencies for  $R = R_e$ . The ideal density matrix  $\rho_{\text{ideal}} = |\Psi_u\rangle\langle\Psi_u|$  and the fidelity  $F(\rho_{\text{exp}}, |\Psi_u\rangle\langle\Psi_u|)$  are shown for comparison.

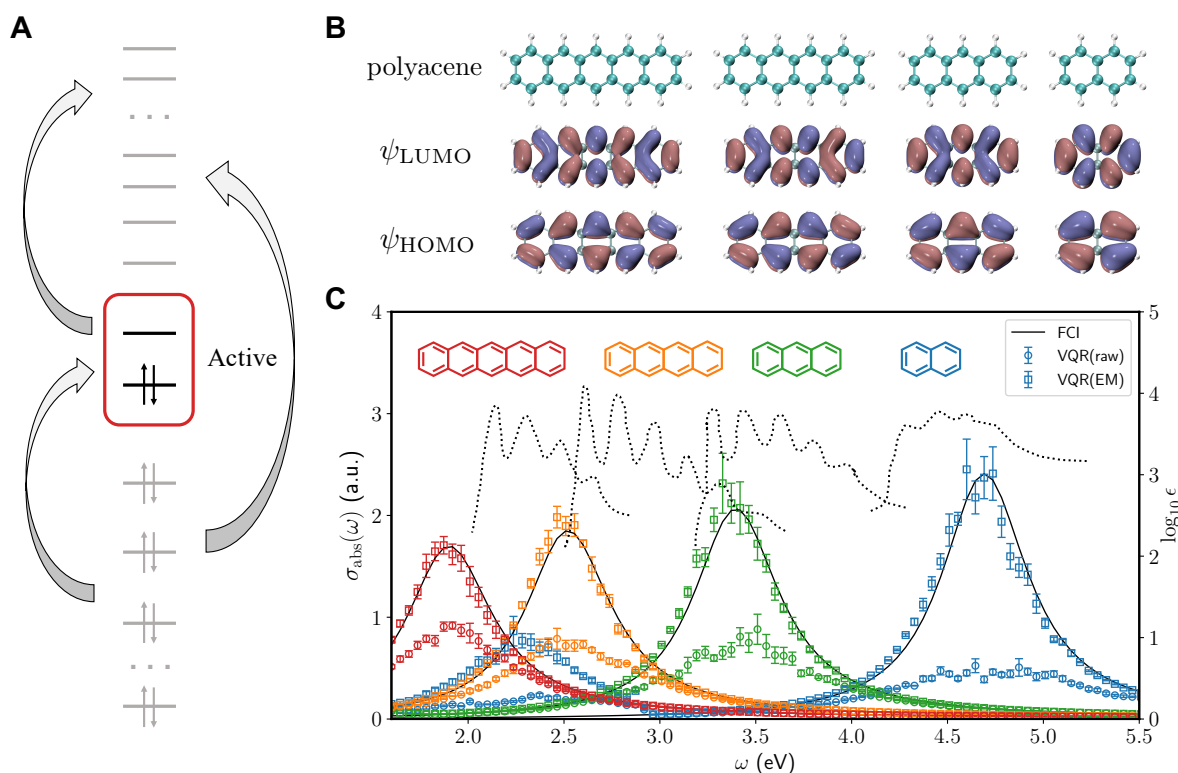


**Fig. 4. UV-Vis absorption spectra of polyacenes from two-qubit simulations.** (A) Active space model in which only a selected number of electrons and orbitals within the active space (red box) are treated at the FCI level. Grey arrows represent excitations responsible for dynamic electron correlation missed by the active space approximation. (B) Structures of the polyacenes with different number of rings and the CAS(2e,2o) model composed of HOMO and LUMO for each molecule. (C) Simulated absorption spectra  $\sigma_{\text{abs}}(\omega)$  with  $\gamma = 0.01$  a.u. (open circles for raw results and squares for error mitigated results) compared against the FCI results (black lines). All the computed spectra have been shifted by  $-1.9$  eV to take into account the missing dynamic correlation. Experimental absorption spectra (dotted lines) are taken from Ref. (39).

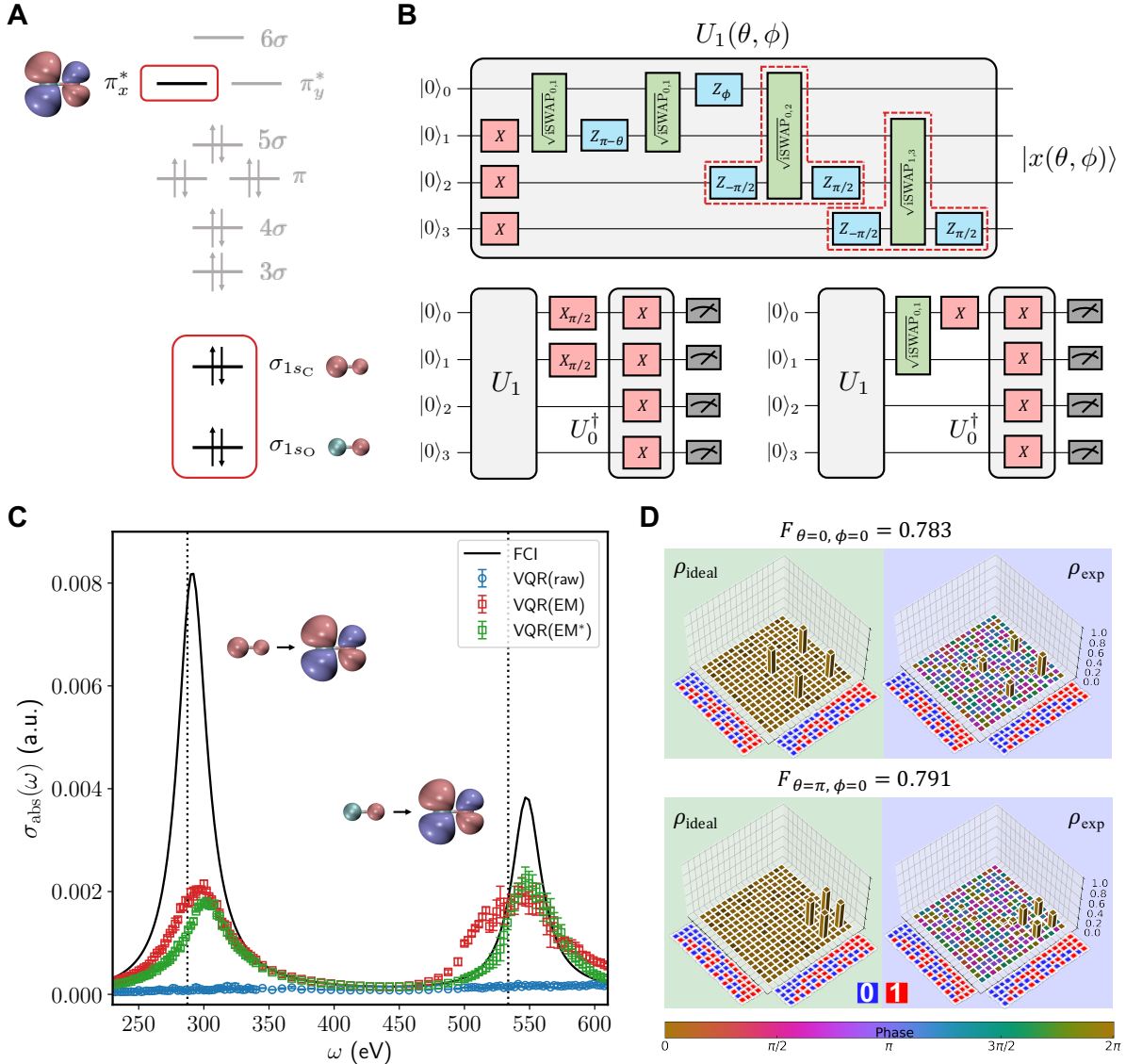


**Fig. 5. X-ray absorption spectra of CO from four-qubit simulations.** (A) Molecular orbital diagram and the CAS(4e,3o) model composed of  $\sigma_{1sO}$ ,  $\sigma_{1sC}$ , and  $\pi_x^*$  orbitals (red boxes). (B) PQC for  $|x(\theta, \phi)\rangle$  in VQR (upper) and the two quantum circuits for evaluating the cross term  $|\langle \Psi_0 | \hat{V}^\dagger \hat{A}(\omega) | x \rangle|^2$  (lower). (C) Simulated absorption spectra  $\sigma_{\text{abs}}(\omega)$  with  $\gamma = 0.5$  a.u. (open circles for raw results and squares for error mitigated results) in comparison with the FCI results (black lines). The VQR(EM\*) results are measured at the ideal angles  $(\theta^*, \phi^*)$  at each frequency. Vertical dotted lines indicate the positions of core excitation energies determined from high-resolution photoabsorption spectra (45,46). (D) Experimental density matrices  $\rho_{\text{exp}}$  characterized by QST for  $|x(\theta, \phi)\rangle$  at two special points  $(\theta, \phi) = (0, 0)$  and  $(\theta, \phi) = (\pi, 0)$ , which correspond to  $|^1\Psi_{\sigma_{1sO} \rightarrow \pi_x^*}\rangle$  and  $|^1\Psi_{\sigma_{1sC} \rightarrow \pi_x^*}\rangle$ , respectively. The ideal density matrix  $\rho_{\text{ideal}} = |\Psi\rangle\langle\Psi|$  (with  $|\Psi\rangle$  being  $|^1\Psi_{\sigma_{1sO} \rightarrow \pi_x^*}\rangle$  or  $|^1\Psi_{\sigma_{1sC} \rightarrow \pi_x^*}\rangle$ ) and the fidelity  $F(\rho_{\text{exp}}, |\Psi\rangle)$  are shown for comparison.

# Supplementary Materials for “Quantum computation of molecular electronic spectroscopy on a superconducting quantum processor”

Kaixuan Huang<sup>2,3†</sup>, Xiaoxia Cai<sup>1†</sup>, Hao Li<sup>3,7†</sup>, Zi-Yong Ge<sup>5</sup>, Ruijuan Hou<sup>1</sup>,  
Hekang Li<sup>3</sup>, Tong Liu<sup>3,4</sup>, Yunhao Shi<sup>3,4</sup>, Chitong Chen<sup>3,4</sup>, Dongning Zheng<sup>3,4,6</sup>,  
Kai Xu<sup>3,4,6\*</sup>, Zhi-Bo Liu<sup>2\*</sup>, Zhendong Li<sup>1\*</sup>, Heng Fan<sup>3,4,6\*</sup>, Wei-Hai Fang<sup>1</sup>

<sup>1</sup> Key Laboratory of Theoretical and Computational Photochemistry, Ministry of Education,  
College of Chemistry, Beijing Normal University, Beijing 100875, China

<sup>2</sup> The Key Laboratory of Weak Light Nonlinear Photonics, Ministry of Education,  
Teda Applied Physics Institute and School of Physics, Nankai University, Tianjin 300457, China

<sup>3</sup> Institute of Physics, Chinese Academy of Sciences, Beijing 100190, China

<sup>4</sup> School of Physical Sciences, University of Chinese Academy of Sciences, Beijing 100190, China

<sup>5</sup> Theoretical Quantum Physics Laboratory, RIKEN Cluster for Pioneering Research,  
Wako-shi, Saitama 351-0198, Japan

<sup>6</sup> CAS Center for Excellence in Topological Quantum Computation,  
University of Chinese Academy of Sciences, Beijing 100190, China

<sup>7</sup> School of Physics, Northwest University, Xi'an 710127, China

† These authors contributed equally;

\* To whom correspondence should be addressed;

E-mail: kaixu@iphy.ac.cn, liuzb@nankai.edu.cn, zhendongli@bnu.edu.cn, hfan@iphy.ac.cn

## Contents

S1 Variational quantum response (VQR) approach

3

S1.1	Algorithm for linear response properties . . . . .	3
S1.2	Algorithms for the cross term $ \langle \Psi_0   \hat{V}^\dagger \hat{A}(\omega)   x \rangle ^2$ . . . . .	7
<b>S2</b>	<b>Device information</b>	<b>11</b>
S2.1	Qubit information . . . . .	11
S2.2	Crosstalks . . . . .	12
S2.3	$\sqrt{i}$ SWAP gate . . . . .	14
<b>S3</b>	<b>Two-qubit simulations for H<sub>2</sub> and polyacenes</b>	<b>17</b>
S3.1	Fermion-to-qubit mapping and wavefunction ansätze . . . . .	17
S3.2	Details of VQR algorithm . . . . .	18
S3.3	Error mitigation via spatial symmetry projection . . . . .	20
S3.4	VQE experiments . . . . .	21
S3.5	VQR experiments . . . . .	22
S3.6	Additional results from quantum chemistry calculations . . . . .	24
S3.6.1	Dipole polarizabilities of H <sub>2</sub> from FCI, HF, and DFT . . . . .	24
S3.6.2	Estimation of dynamic correlation by perturbation theory for polyacenes	25
<b>S4</b>	<b>Four-qubit simulations for CO</b>	<b>30</b>
S4.1	Fermion-to-qubit mapping and wavefunction ansatz . . . . .	30
S4.2	Details of VQR algorithm . . . . .	31
S4.3	Error mitigation via spin symmetry projection . . . . .	33
S4.4	VQR experiments . . . . .	34

# S1 Variational quantum response (VQR) approach

## S1.1 Algorithm for linear response properties

To compute linear response properties of molecules such as the electronic absorption spectra, we adopted the Born-Oppenheimer approximation and neglected relativistic effects (3). Consequently, the status of a molecule is described by the time-independent Schrödinger equation,

$$\hat{H}_0|\Psi\rangle = E|\Psi\rangle, \quad (\text{S1})$$

with the electronic Hamiltonian  $\hat{H}_0$  being

$$\hat{H}_0 = \sum_{i=1}^N \hat{h}_i + \sum_{i<j}^N \frac{1}{r_{ij}} + E_{\text{NN}}, \quad \hat{h}_i = -\frac{1}{2}\nabla_i^2 + \sum_{A=1}^M -\frac{Z_A}{r_{iA}} \quad (\text{S2})$$

where  $E_{\text{NN}} = \sum_{A<B}^M \frac{Z_A Z_B}{R_{AB}}$  is a constant for a fixed nuclei configuration  $\{(Z_A, \vec{R}_A)\}_{A=1}^M$  with  $Z_A$  being the nuclear charge of the  $A$ -th nucleus. Given a set of orthonormal molecular spin-orbitals  $\{\phi_p(x)\}_{p=1}^n$  with the composite coordinate  $x \equiv (\vec{r}, \zeta)$  composed of position  $\vec{r}$  and spin  $\zeta \in \{\alpha, \beta\}$ , the second quantized form (52) of  $\hat{H}_0$  reads

$$\hat{H}_0 = \sum_{pq} [p|h|q] a_p^\dagger a_q + \sum_{pqrs} \frac{1}{2} [ps|qr] a_p^\dagger a_q^\dagger a_r a_s + E_{\text{NN}}, \quad (\text{S3})$$

$$[p|h|q] = \int dx \phi_p^*(x) \hat{h} \phi_q(x), \quad (\text{S4})$$

$$[ps|qr] = \int dx_1 dx_2 \phi_p^*(x_1) \phi_s(x_1) r_{12}^{-1} \phi_q(x_2) \phi_r(x_2), \quad (\text{S5})$$

where  $a_p^\dagger$  ( $a_p$ ) are fermionic creation (annihilation) operators. The coefficients  $[p|h|q]$  and  $[ps|qr]$  are the one-electron and two-electron molecular integrals in Mulliken notations, respectively, which can be computed from quantum chemistry packages. With a fermion-to-qubit mapping (29, 30, 53),  $\hat{H}_0$  can be transformed to qubit operators,

$$\hat{H}_0 = \sum_k h_k P_k, \quad P_k = \sigma_0^k \otimes \sigma_1^k \otimes \cdots \otimes \sigma_{n-1}^k, \quad (\text{S6})$$

with  $\sigma_i \in \{I, X, Y, Z\}$ . Following from the two-body nature of electron-electron interaction, the number of Pauli terms ( $P_k$ ) in  $\hat{H}_0$  scales as  $O(n^4)$ . Similarly, a one-body perturbation operator  $\hat{V}$  such as the electric dipole operator can be expressed as

$$\hat{V} = \sum_k v_k P_k, \quad (\text{S7})$$

where the number of terms scales as  $O(n^2)$ .

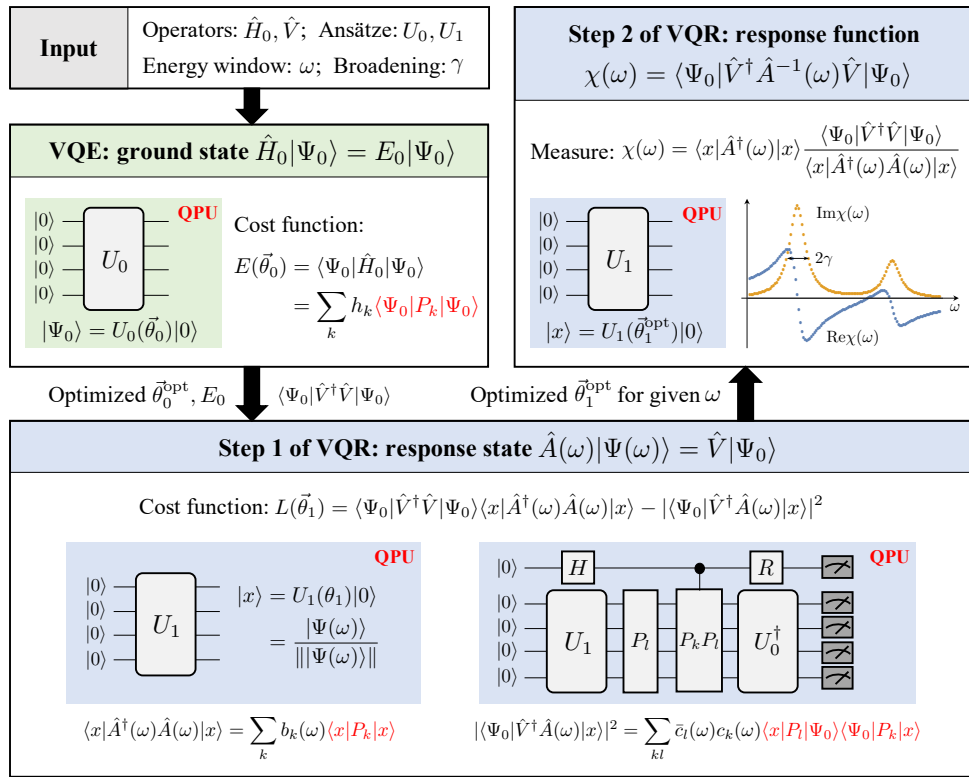


**Fig. S1. Variational hybrid quantum-classical algorithms for linear response properties of molecules.** Terms highlighted in red are computed on quantum processor units (QPU).

The flowchart of variational hybrid quantum-classical algorithms for linear response properties of molecules is shown in Fig. S1. The variational quantum eigensolver (18, 19) (VQE) is first applied to compute the ground state, by optimizing the energy function of a variational

ansatz  $|\Psi_0\rangle = U(\vec{\theta}_0)|0\rangle$  with respect to the set of parameters  $\vec{\theta}_0$ ,

$$E(\vec{\theta}_0) = \langle \Psi_0 | \hat{H}_0 | \Psi_0 \rangle = \sum_k h_k \langle \Psi_0 | P_k | \Psi_0 \rangle. \quad (\text{S8})$$

The expectation values  $\langle \Psi_0 | P_k | \Psi_0 \rangle$  are measured on quantum computers.

The variational quantum response (VQR) approach for linear response properties of molecules includes two steps: obtaining the response state  $|\Psi(\omega)\rangle$  at a given frequency in the interested regime and measuring the response function  $\chi(\omega)$ . The response state is determined from the linear response equation (25)

$$\hat{A}(\omega)|\Psi(\omega)\rangle = \hat{V}|\Psi_0\rangle, \quad \hat{A}(\omega) = \hat{H}_0 - E_0 - (\omega + i\gamma), \quad (\text{S9})$$

which can be solved by minimizing a cost function constructed using the Cauchy-Schwarz inequality,

$$L(\vec{\theta}_1) = \langle \Psi_0 | \hat{V}^\dagger \hat{V} | \Psi_0 \rangle \langle x | \hat{A}^\dagger(\omega) \hat{A}(\omega) | x \rangle - |\langle \Psi_0 | \hat{V}^\dagger \hat{A}(\omega) | x \rangle|^2, \quad (\text{S10})$$

with a variational ansatz for the normalized response state  $|x\rangle = |\Psi(\omega)\rangle / \|\Psi(\omega)\| = U_1(\vec{\theta}_1)|0\rangle$ . For brevity, we will omit the frequency dependence of the optimized set of parameters  $\vec{\theta}_1$  and  $|x\rangle$  in the following context. This cost function obeys  $L(\vec{\theta}_1) \geq 0$ , and the minimum is achieved for  $|x\rangle \propto \hat{A}^{-1}(\omega) \hat{V} |\Psi_0\rangle$ . Note that the choice of cost functions for solving linear systems of equations is not unique (31,32). For instance, another natural choice is  $L(\vec{\theta}_1) = \|\hat{A}(\omega)|\Psi(\omega)\rangle - \hat{V}|\Psi_0\rangle\|^2$ . In this work, we chose Eq. (S10) due to the appearance of  $|\langle \Psi_0 | \hat{V}^\dagger \hat{A}(\omega) | x \rangle|^2$ , which enables a computation scheme with less controlled operations discussed in detail in the next subsection. Both  $\langle \Psi_0 | \hat{V}^\dagger \hat{V} | \Psi_0 \rangle$  and  $\langle x | \hat{A}^\dagger(\omega) \hat{A}(\omega) | x \rangle$  can be computed from measurements after preparing  $|\Psi_0\rangle$  and  $|x\rangle$ , respectively. According to Eq. (S9),  $\hat{A}^\dagger(\omega) \hat{A}(\omega)$  can be written as

$$\hat{A}^\dagger(\omega) \hat{A}(\omega) = (\hat{H}_0 - E_0 - \omega)^2 + \gamma^2 = \sum_k b_k(\omega) P_k, \quad (\text{S11})$$

where the number of terms scales as  $O(n^8)$ . This scaling can be improved by using low-rank decompositions (14, 54).

After  $|x\rangle$  is obtained at a given frequency, the response function  $\chi(\omega)$  can be computed from (25)

$$\begin{aligned}
\chi(\omega) &= \langle \Psi_0 | \hat{V}^\dagger \hat{A}^{-1}(\omega) \hat{V} | \Psi_0 \rangle \\
&= \langle \Psi_0 | \hat{V}^\dagger (\hat{A}^\dagger(\omega))^{-1} \hat{A}^\dagger(\omega) \hat{A}^{-1}(\omega) \hat{V} | \Psi_0 \rangle \\
&= \langle \Psi(\omega) | \hat{A}^\dagger(\omega) | \Psi(\omega) \rangle \\
&= \langle x | \hat{A}^\dagger(\omega) | x \rangle \| |\Psi(\omega)\rangle \|^2.
\end{aligned} \tag{S12}$$

Using Eq. (S9), the square of the norm  $\| |\Psi(\omega)\rangle \|^2$  is expressed as

$$\| |\Psi(\omega)\rangle \|^2 = \frac{\langle \Psi_0 | \hat{V}^\dagger \hat{V} | \Psi_0 \rangle}{\langle x | \hat{A}^\dagger(\omega) \hat{A}(\omega) | x \rangle}. \tag{S13}$$

The final expression for computing  $\chi(\omega)$  is

$$\chi(\omega) = \langle x | \hat{A}^\dagger(\omega) | x \rangle \frac{\langle \Psi_0 | \hat{V}^\dagger \hat{V} | \Psi_0 \rangle}{\langle x | \hat{A}^\dagger(\omega) \hat{A}(\omega) | x \rangle}, \tag{S14}$$

which requires the measurements of  $\langle x | \hat{A}^\dagger(\omega) | x \rangle$  and  $\langle x | \hat{A}^\dagger(\omega) \hat{A}(\omega) | x \rangle$  given the optimized  $|x\rangle$  at a given frequency. Eq. (S14) can be written in a more revealing way by separating out the real and imaginary parts,

$$\text{Re}\chi(\omega) = \langle x | \hat{H}_0 - E_0 - \omega | x \rangle \| |\Psi(\omega)\rangle \|^2 = \langle x | \hat{H}_0 - E_0 - \omega | x \rangle \frac{\langle \Psi_0 | \hat{V}^\dagger \hat{V} | \Psi_0 \rangle}{\langle x | \hat{A}^\dagger(\omega) \hat{A}(\omega) | x \rangle}, \tag{S15}$$

$$\text{Im}\chi(\omega) = \gamma \| |\Psi(\omega)\rangle \|^2 = \gamma \frac{\langle \Psi_0 | \hat{V}^\dagger \hat{V} | \Psi_0 \rangle}{\langle x | \hat{A}^\dagger(\omega) \hat{A}(\omega) | x \rangle}. \tag{S16}$$

This shows that the peaks in  $\text{Im}\chi(\omega)$ , which is related with the absorption cross section, depend mainly on  $1/\langle x | \hat{A}^\dagger(\omega) \hat{A}(\omega) | x \rangle$ . To get a deeper understanding, we can find from Eq. (S13) using the spectral decomposition for  $|\Psi(\omega)\rangle$

$$\langle x | \hat{A}^\dagger(\omega) \hat{A}(\omega) | x \rangle = \frac{\langle \Psi_0 | \hat{V}^\dagger \hat{V} | \Psi_0 \rangle}{\| |\Psi(\omega)\rangle \|^2} = \frac{\langle \Psi_0 | \hat{V}^\dagger \hat{V} | \Psi_0 \rangle}{\sum_n \frac{|\langle \Psi_n | \hat{V} | \Psi_0 \rangle|^2}{(\omega_{n0} - \omega)^2 + \gamma^2}}, \tag{S17}$$

such that

$$\text{Im}\chi(\omega) = \sum_n |\langle \Psi_n | \hat{V} | \Psi_0 \rangle|^2 \frac{\gamma}{(\omega_{n0} - \omega)^2 + \gamma^2}, \quad (\text{S18})$$

which shows that  $\text{Im}\chi(\omega)$  is a weighted superposition of Lorentzians, which have peaks at  $\omega = \omega_{n0} = E_n - E_0$  and a common full width at half maximum (FWHM)  $2\gamma$ .

Linear response properties of molecules can be computed from the generic term  $\chi(\omega)$  by choosing different  $\hat{V}$ . For instance, the  $zz$ -component of the dynamic polarizabilities can be written as

$$\begin{aligned} \alpha_{zz}(\omega) &= \sum_{n>0} \frac{\langle \Psi_0 | \hat{z} | \Psi_n \rangle \langle \Psi_n | \hat{z} | \Psi_0 \rangle}{\omega_{n0} - (\omega + i\gamma)} + \sum_{n>0} \frac{\langle \Psi_0 | \hat{z} | \Psi_n \rangle \langle \Psi_n | \hat{z} | \Psi_0 \rangle}{\omega_{n0} + (\omega + i\gamma)} \\ &= \chi(\omega) \Big|_{\hat{V} \rightarrow \hat{z}} + \chi(\omega) \Big|_{\hat{V} \rightarrow \hat{z}, \omega \rightarrow -\omega, \gamma \rightarrow -\gamma}. \end{aligned} \quad (\text{S19})$$

In this work, we only consider the first term which is the resonant contribution (55). The second anti-resonant contribution is usually small and can be included using the same VQR approach if necessary. Other off-diagonal components can be computed by invoking the polarization identity (25). Similarly, the single-particle Green's functions  $G_{ij}(\omega) = \langle \Psi_0 | a_i \hat{A}^{-1}(\omega) a_j^\dagger | \Psi_0 \rangle$  can also be computed from  $\chi(\omega)$  using the same algorithm, simply by setting  $\hat{V}$  as the fermionic creation/annihilation operators.

## S1.2 Algorithms for the cross term $|\langle \Psi_0 | \hat{V}^\dagger \hat{A}(\omega) | x \rangle|^2$

The cross term  $|\langle \Psi_0 | \hat{V}^\dagger \hat{A}(\omega) | x \rangle|^2$  can be computed in different ways. Using Eqs. (S6) and (S7),  $\hat{V}^\dagger \hat{A}(\omega)$  can be written as

$$\hat{V}^\dagger \hat{A}(\omega) = \sum_k c_k(\omega) P_k, \quad (\text{S20})$$

where the number of terms scales as  $O(n^6)$ . To reduce the number of terms, using the fact that  $|\Psi_0\rangle$  is also an eigenfunction of  $\hat{A}(\omega)$ , we can rewrite  $\langle \Psi_0 | \hat{V}^\dagger \hat{A}(\omega) | x \rangle$  as

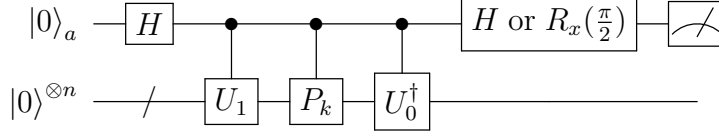
$$\langle \Psi_0 | \hat{V}^\dagger \hat{A}(\omega) | x \rangle = \langle \Psi_0 | [\hat{V}^\dagger, \hat{A}(\omega)] + \hat{A}(\omega) \hat{V}^\dagger | x \rangle = \langle \Psi_0 | [\hat{V}^\dagger, \hat{A}(\omega)] - (\omega + i\gamma) \hat{V}^\dagger | x \rangle. \quad (\text{S21})$$

The resulting effective operator  $(\hat{V}^\dagger \hat{A}(\omega))_{\text{eff}} = [\hat{V}^\dagger, \hat{A}(\omega)] - (\omega + i\gamma)\hat{V}^\dagger$  is a two-body fermionic operator and the corresponding qubit operator will only contain  $O(n^4)$  terms.

Given an appropriate expansion for  $\hat{V}^\dagger \hat{A}(\omega)$  or its effective version, the most obvious way to compute  $|\langle \Psi_0 | \hat{V}^\dagger \hat{A}(\omega) | x \rangle|^2$  is via the Hadamard test (22, 31). With the following expansion,

$$\langle \Psi_0 | \hat{V}^\dagger \hat{A}(\omega) | x \rangle = \sum_k c_k(\omega) \langle 0 | U_0^\dagger P_k U_1 | 0 \rangle, \quad (\text{S22})$$

the expectation value of the unitary  $U_0^\dagger P_k U_1$  can be computed with the following Hadamard test circuit



The disadvantage of this approach is that the large number of controlled unitaries is infeasible for realizations on near-term devices.

To avoid this deficiency, we propose a new strategy for computing the cross term, which can be viewed as trading controlled unitaries by measuring more circuits. The resulting circuits require less controlled Pauli operators than those presented in Ref. (32, 56). The same method can also be applied to compute transition amplitudes between two states  $|\langle \Psi_i | \hat{O} | \Psi_j \rangle|^2 = |\langle 0 | U_i^\dagger (\sum_k o_k P_k) U_j | 0 \rangle|^2$ . To begin with, we divide the terms in the expansion

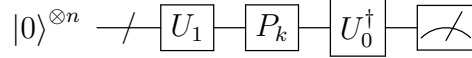
$$\begin{aligned} |\langle \Psi_0 | \hat{V}^\dagger \hat{A}(\omega) | x \rangle|^2 &= |\langle 0 | U_0^\dagger \left( \sum_k c_k(\omega) P_k \right) U_1 | 0 \rangle|^2 \\ &= \sum_{lk} \bar{c}_l(\omega) c_k(\omega) \langle 0 | U_1^\dagger P_l U_0 | 0 \rangle \langle 0 | U_0^\dagger P_k U_1 | 0 \rangle. \end{aligned} \quad (\text{S23})$$

into the diagonal ( $l = k$ ) and off-diagonal ( $l \neq k$ ) parts

$$\mathcal{E} = \sum_k |c_k(\omega)|^2 \langle 0|U_1^\dagger P_k U_0|0\rangle \langle 0|U_0^\dagger P_k U_1|0\rangle, \quad (\text{S24})$$

$$\begin{aligned} \mathcal{O} &= \sum_{l \neq k} \bar{c}_l(\omega) c_k(\omega) \langle 0|U_1^\dagger P_l U_0|0\rangle \langle 0|U_0^\dagger P_k U_1|0\rangle \\ &= 2 \sum_{l < k} [\text{Re}(\bar{c}_l(\omega) c_k(\omega)) \text{Re}(\langle 0|U_1^\dagger P_l U_0|0\rangle \langle 0|U_0^\dagger P_k U_1|0\rangle) \\ &\quad - \text{Im}(\bar{c}_l(\omega) c_k(\omega)) \text{Im}(\langle 0|U_1^\dagger P_l U_0|0\rangle \langle 0|U_0^\dagger P_k U_1|0\rangle)]. \end{aligned} \quad (\text{S25})$$

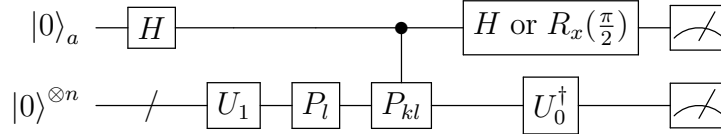
Then, each term in  $\mathcal{E}$  can be simply obtained using



$$\langle 0|U_1^\dagger P_k U_0|0\rangle \langle 0|U_0^\dagger P_k U_1|0\rangle = |\langle 0|U_0^\dagger P_k U_1|0\rangle|^2 = P_{0_0 \dots 0_{n-1}}, \quad (\text{S26})$$

where  $P_{0_0 \dots 0_{n-1}}$  represents the probability of  $|0_0 \dots 0_{n-1}\rangle$  observed for the prepared state  $U_0^\dagger P_k U_1|0\rangle$ .

For the off-diagonal terms,  $\text{Re}(\langle 0|U_1^\dagger P_l U_0|0\rangle \langle 0|U_0^\dagger P_k U_1|0\rangle)$  and  $\text{Im}(\langle 0|U_1^\dagger P_l U_0|0\rangle \langle 0|U_0^\dagger P_k U_1|0\rangle)$  can be computed via the following circuit



where  $P_{kl} \equiv P_k P_l$  and  $H$  (or  $R_x(\frac{\pi}{2})$ ) is used for the real (imaginary) part, viz.,

$$\begin{aligned} \text{Re}(\langle 0|U_1^\dagger P_l U_0|0\rangle \langle 0|U_0^\dagger P_k U_1|0\rangle) &= \frac{1}{4} (\langle x_l | (1 + P_{kl})^\dagger U_0 |0\rangle \langle 0|U_0^\dagger (1 + P_{kl}) |x_l\rangle \\ &\quad - \langle x_l | (1 - P_{kl})^\dagger U_0 |0\rangle \langle 0|U_0^\dagger (1 - P_{kl}) |x_l\rangle) \\ &= P_{0_0 0_1 \dots 0_n} - P_{1_0 0_1 \dots 0_n}, \end{aligned} \quad (\text{S27})$$

where  $|x_l\rangle \equiv P_l U_1|0\rangle$ . This scheme does not require controlled  $U_0$  nor  $U_1$ , but only controlled- $P_{kl}$ , which is more feasible on near-term devices. In total, this general scheme requires  $O(n^6)$  measurements for computing the cross term.

Further simplifications are possible for special cases. In this work, we utilize the facts that for our tests, the set of  $P_k$  can be simplified to single-qubit Pauli X operators  $X_k$ , as well as  $\langle 0|U_0^\dagger U_1|0\rangle = 0$  and  $\langle 0|U_0^\dagger X_k X_l U_1|0\rangle = 0$  due to spatial symmetry of the problems investigated. With these conditions, the real and imaginary parts of  $\langle 0|U_1^\dagger X_l U_0|0\rangle \langle 0|U_0^\dagger X_k U_1|0\rangle$  ( $k \neq l$ ) can be computed without using the ancilla qubit as follows:

(1)  $\text{Re}(\langle 0|U_1^\dagger X_l U_0|0\rangle \langle 0|U_0^\dagger X_k U_1|0\rangle)$ : By noting

$$\begin{aligned} |\langle 0|U_0^\dagger e^{-i\frac{\pi}{4}X_k} e^{-i\frac{\pi}{4}X_l} U_1|0\rangle|^2 &= \frac{1}{4} |\langle 0|U_0^\dagger (1 - i(X_k + X_l) - X_k X_l) U_1|0\rangle|^2 = \frac{1}{4} |\langle 0|U_0^\dagger (X_k + X_l) U_1|0\rangle|^2 \\ &= \frac{1}{4} (|\langle 0|U_0^\dagger X_k U_1|0\rangle|^2 + |\langle 0|U_0^\dagger X_l U_1|0\rangle|^2) + \frac{1}{2} \text{Re}(\langle 0|U_1^\dagger X_l U_0|0\rangle \langle 0|U_0^\dagger X_k U_1|0\rangle) \end{aligned} \quad (\text{S28})$$

the real part becomes

$$\text{Re}(\langle 0|U_1^\dagger X_l U_0|0\rangle \langle 0|U_0^\dagger X_k U_1|0\rangle) = 2|\langle 0|U_0^\dagger e^{-i\frac{\pi}{4}X_k} e^{-i\frac{\pi}{4}X_l} U_1|0\rangle|^2 - \frac{1}{2} \left( |\langle 0|U_0^\dagger X_k U_1|0\rangle|^2 + |\langle 0|U_0^\dagger X_l U_1|0\rangle|^2 \right) \quad (\text{S29})$$

where the first term can be computed by preparing the state  $U_0^\dagger R_{x,k}(\frac{\pi}{2}) R_{x,l}(\frac{\pi}{2}) U_1|0\rangle$ .

(2)  $\text{Im}(\langle 0|U_1^\dagger X_l U_0|0\rangle \langle 0|U_0^\dagger X_k U_1|0\rangle)$ : By using

$$|\langle 0|U_0^\dagger (X_l + iX_k) U_1|0\rangle|^2 = |\langle 0|U_0^\dagger X_l (1 + iX_l X_k) U_1|0\rangle|^2 = 2|\langle 0|U_0^\dagger X_l e^{i\frac{\pi}{4}X_l X_k} U_1|0\rangle|^2, \quad (\text{S30})$$

the imaginary part becomes

$$\text{Im}(\langle 0|U_1^\dagger X_l U_0|0\rangle \langle 0|U_0^\dagger X_k U_1|0\rangle) = -|\langle 0|U_0^\dagger X_l e^{i\frac{\pi}{4}X_l X_k} U_1|0\rangle|^2 + \frac{1}{2} \left( |\langle 0|U_0^\dagger X_l U_1|0\rangle|^2 + |\langle 0|U_0^\dagger X_k U_1|0\rangle|^2 \right) \quad (\text{S31})$$

where the first term can be computed by preparing the state  $U_0^\dagger X_l e^{i\frac{\pi}{4}X_l X_k} U_1|0\rangle$ .

In summary, we have derived a general scheme using Eq. (S27) for evaluating the cross term in the cost function. In addition, the ancilla qubit can be removed for special cases. Eqs. (S29) and (S31) are the actual expressions used for systems investigated in the present work.

## S2 Device information

### S2.1 Qubit information

The superconducting quantum processor used in our experiment consists of 20 transmon qubits, which are interconnected by a central bus resonator with frequency fixed at around  $\omega_R/2\pi \approx 5.51$  GHz, as shown in Fig. 2a in the main text. The detailed fabrication processes and basic circuit elements can be found in Ref. (27). Five qubits, denoted by Q<sub>3</sub>, Q<sub>6</sub>, Q<sub>13</sub>, Q<sub>14</sub>, Q<sub>20</sub>, are used in this work, where Q<sub>14</sub> and Q<sub>20</sub> are used in the experiments for H<sub>2</sub> and polyacenes, while Q<sub>3</sub>, Q<sub>6</sub>, Q<sub>13</sub>, and Q<sub>20</sub> are employed for studying the CO molecule. Their resonant frequencies, denoted by  $\omega_{\text{idle}}/2\pi$ , are carefully arranged to minimize any possible unwanted interaction and crosstalk error among qubits during single-qubit operations. All relevant information about the employed qubits are summarized in Table S1. The anharmonicity of the six qubits are about 245 MHz. The measured qubit characteristic decoherence parameters (energy relaxation time  $T_1$  and Ramsey Gaussian dephasing time  $T_2^*$ ) can be found in Table S1, which are far greater than the circuit length (several hundred nanoseconds). Single qubit operations, including the  $X/2$  ( $=R_x(\pi/2)$ ) and  $X$  ( $=R_x(\pi)$ ) gates, have a timescale length of 30 ns and a FWHM of 15 ns, respectively. The quadrature correction term with DRAG coefficient  $\alpha$  are optimized following the DRAG theory to minimize the leakage to higher energy levels (57). The readout pulses for all qubits are 1.5  $\mu\text{s}$  in length, and the readout powers and frequencies are optimized for a high-visibility and low-state-error readout. As shown in Table S1, the readout fidelities, denoted by  $F_0$  and  $F_1$ , are no less than 0.981 and 0.918 for  $|0\rangle$  and  $|1\rangle$  state, respectively. During the experiment, we periodically calibrate the amplitude of DC source output for the idle frequency and the pulse amplitude of single-qubit gates of each qubit to avoid the performance drifts with time. We also monitor the readout fidelities in Fig. S2 during the experiment in order to perform the real-time correction of readout errors (58), by applying the inverse of the tensor product of

matrices  $\begin{pmatrix} F_0 & 1 - F_1 \\ 1 - F_0 & F_1 \end{pmatrix}$  for the involved qubits to the measured occupation probabilities.

Table S1: Qubit characteristics.  $\omega_{\text{idle}}$  is the idle frequency of qubit where decoherence parameters (including energy relaxation time  $T_1$  and Ramsey Gaussian dephasing time  $T_2^*$ ) are measured.  $F_0$  ( $F_1$ ) is the measurement probability of  $|0\rangle$  ( $|1\rangle$ ) when the qubit is prepared in  $|0\rangle$  ( $|1\rangle$ ), which is used to mitigate the readout errors.

	H <sub>2</sub> and polyacenes		CO			
	Q <sub>14</sub>	Q <sub>20</sub>	Q <sub>3</sub>	Q <sub>6</sub>	Q <sub>13</sub>	Q <sub>20</sub>
$\omega_{\text{idle}}/2\pi$ (GHz)	5.200	5.260	5.190	5.130	5.080	5.025
$T_1$ ( $\mu\text{s}$ )	23.4	33.9	16.1	28.8	15.5	22.9
$T_2^*$ ( $\mu\text{s}$ )	3.7	3.6	2.5	3.5	2.2	2.4
$F_0$	0.989	0.986	0.985	0.989	0.981	0.986
$F_1$	0.952	0.948	0.918	0.934	0.920	0.922

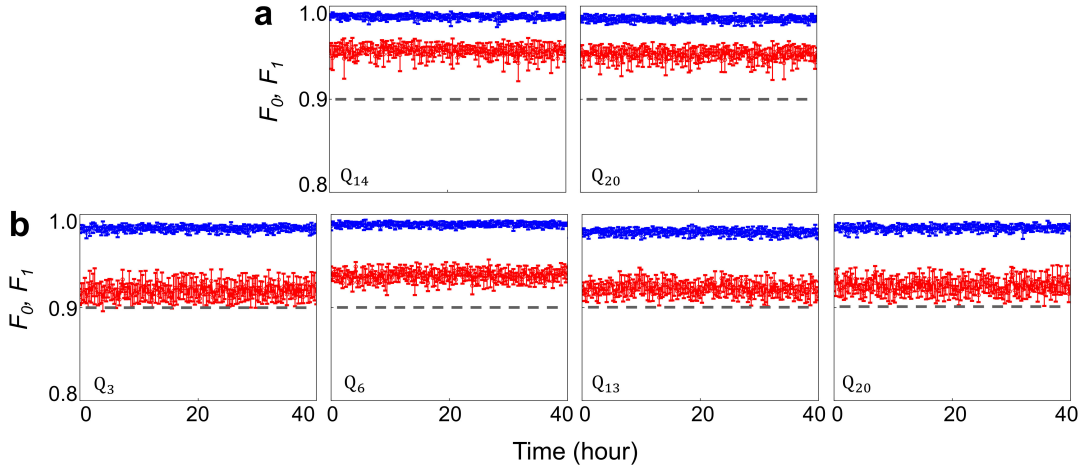


**Fig. S2. The readout fidelities of the used qubits with error bars monitored over 40 hours.** The results corresponding to  $|0\rangle$  and  $|1\rangle$  state are denoted by  $F_0$  (blue) and  $F_1$  (red), respectively. a, Qubits used in experiments for H<sub>2</sub> and polyacenes. b, Qubits used in experiments for CO.

## S2.2 Crosstalks

The Z line crosstalks between different qubit pairs are calibrated based on the Z-crosstalk matrix  $\widetilde{M}_Z$  as done in Ref. (59), where each element denotes the zpa (Z pulse amplitude) sensed

by  $Q_j$  when a unitary zpa is applied to  $Q_i$ . Note that all  $(\widetilde{M}_Z)_{i,j}$  elements are less than 2.5%, as shown in Fig. S3a. All zpa applied to qubits are calibrated based on the mapping relationship  $\widetilde{Z}_{\text{sensed}} = \widetilde{M}_Z \cdot \widetilde{Z}_{\text{applied}}$ , where  $\widetilde{Z}_{\text{sensed}}$  and  $\widetilde{Z}_{\text{applied}}$  represent the zpa sensed and applied to qubits, respectively. We also characterize the XY line crosstalks by measuring the occupation probabilities of  $Q_j$  when  $Q_i$  is prepared in  $|0\rangle$  and  $|1\rangle$ , respectively. The crosstalks between XY lines are caused by insufficient crossover bonding or the frequency leakage, while the latter can be efficiently ameliorated by calibrating the room temperature electronics and carefully arranging the idle frequency of qubits. The XY-crosstalk matrix  $\widetilde{M}_{XY}$  are shown in Fig. S3b, and all  $(\widetilde{M}_{XY})_{i,j}$  elements do not exceed 0.8%, indicating the feasibility for stimulating all qubits simultaneously.

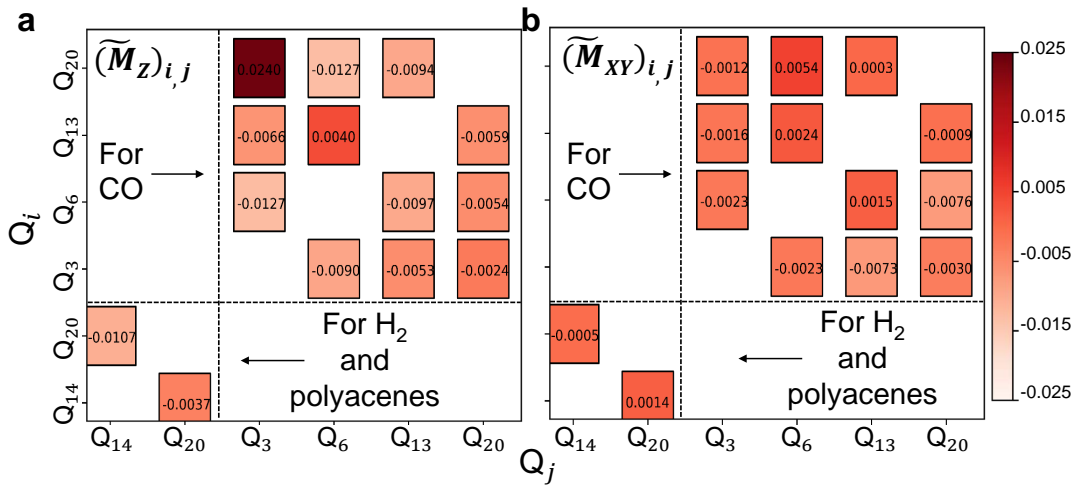


**Fig. S3. Z- and XY-crosstalk matrices  $\widetilde{M}_Z$  and  $\widetilde{M}_{XY}$ .** a, Z-crosstalk matrix  $\widetilde{M}_Z$ , where each element  $(\widetilde{M}_Z)_{i,j}$  denotes the needed zpa of  $Q_j$  when a unitary zpa is applied to  $Q_i$ . b, XY-crosstalk matrix  $\widetilde{M}_{XY}$ , where each element  $(\widetilde{M}_{XY})_{i,j}$  represents the difference of measured occupation probabilities of  $Q_j$  when  $Q_i$  is stimulated to  $|1\rangle$  with a  $X$  gate.

### S2.3 $\sqrt{i\text{SWAP}}$ gate

In our experiment, the two-qubit entangling gate  $\sqrt{i\text{SWAP}}$ , with the matrix form

$$\sqrt{i\text{SWAP}} = \begin{pmatrix} 1 & 0 & 0 & 0 \\ 0 & \frac{\sqrt{2}}{2} & \frac{\sqrt{2}}{2}i & 0 \\ 0 & \frac{\sqrt{2}}{2}i & \frac{\sqrt{2}}{2} & 0 \\ 0 & 0 & 0 & 1 \end{pmatrix}, \quad (\text{S32})$$

is generated by tuning all the involved qubits on-resonance with a certain characteristic interaction time  $t_{\sqrt{i\text{SWAP}}} = \frac{\pi}{4|\lambda|}$ , where  $\lambda$  is negative and approximately equals to  $\tilde{g}^2/\Delta$ ,  $\tilde{g}$  is defined as the average coupling strength between qubit and central bus resonator, and  $\Delta$  denotes the detuning between the on-resonance frequency and bus resonator frequency. Here,  $t_{\sqrt{i\text{SWAP}}}$  is optimized to be 43.8 ns, 43.5 ns, 48.1 ns and 56.6 ns for different pairs of qubits Q<sub>14</sub>-Q<sub>20</sub>, Q<sub>3</sub>-Q<sub>6</sub>, Q<sub>3</sub>-Q<sub>13</sub>, and Q<sub>6</sub>-Q<sub>20</sub>, respectively, see Table S2.

To cancel out the dynamical phases accumulated during the entangling interaction, single-qubit phase gates are employed (28), which are optimized by numerical calculations and then added on each qubit before and after the interaction process. The front phase gates guarantee that the  $x$  axes of the Bloch spheres for all qubits are aligned at the beginning of the interaction in the rotating frame of the on-resonance frequency, while the latter ones are to make sure that  $x$  axis of each qubit is aligned in the rotating frame of its idle frequency at the end of the interaction. All phase gates are realized by amplitude-adjustable Z square pulses with a width of 20 ns, indicating a frequency shift of 25 MHz corresponding to the idle point for the phase accumulation of  $\pi$ . We can easily map the relationship between Z pulse amplitude and phase by inserting an amplitude-tunable Z square pulses between two  $X/2$  gates and change the microwave phase of the last  $X/2$  gate, as shown in Fig. S4.

To characterize the performance of  $\sqrt{i\text{SWAP}}$  gates, quantum process tomography (60, 61) (QPT) is performed by preparing a full set of  $6^n$  input states  $\bigotimes_j^n \{I, \pm X/2, \pm Y/2, X\}$  ( $n$  denotes the number of qubits, and  $n = 2$  here). We compare the ideal and experimental process

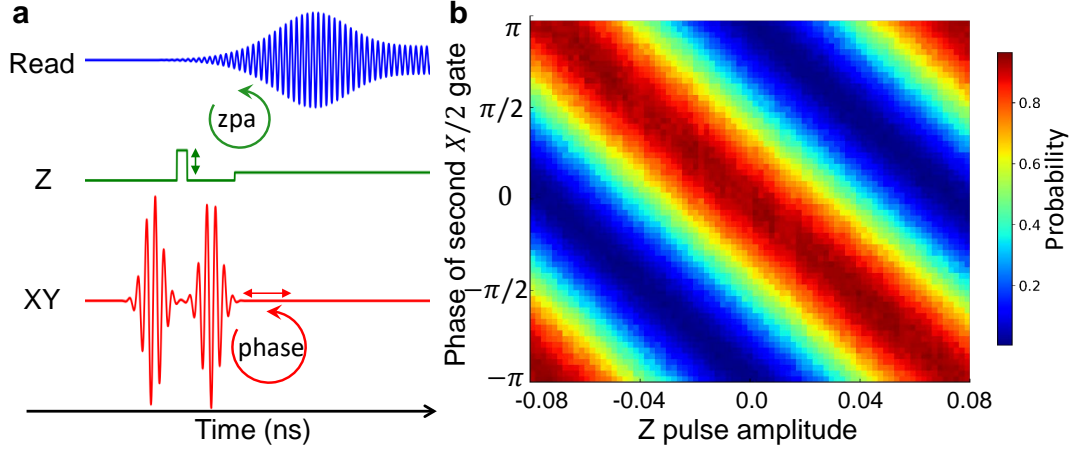


**Fig. S4. Generation of single-qubit phase gate.** a, Pulse sequence for getting the relationship between Z pulse amplitude and phase. b, The measured probability of  $|1\rangle$  state with the change of Z pulse amplitude (zpa) and microwave phase of the second X/2 gate.

matrices (33)  $\chi_{\text{ideal}}$  and  $\chi_{\text{exp}}$ , and calculate the gate fidelities  $F = \text{tr}(\chi_{\text{exp}}\chi_{\text{ideal}})$ . The interaction frequencies  $\omega_I/2\pi$  and fidelities characterized by QPT for different qubit pairs (Q<sub>14</sub>-Q<sub>20</sub>, Q<sub>3</sub>-Q<sub>6</sub>, Q<sub>3</sub>-Q<sub>13</sub>, and Q<sub>6</sub>-Q<sub>20</sub>) involved in our experiments are summarized in Table S2. We have optimized some important parameters of the  $\sqrt{\text{iSWAP}}$  gate by QPT strategy, e.g. the characteristic gate time  $t_{\sqrt{\text{iSWAP}}}$  and zpa for tuning qubits on-resonance with each other. Take the gate Q<sub>14</sub>-Q<sub>20</sub> for an instance, we firstly estimate  $t_{\sqrt{\text{iSWAP}}}$  and zpa through the superexchange (SE) (62) interaction mediated by the central bus resonator at the idle frequency of Q<sub>14</sub> (detuned from the bus resonator frequency by 310 MHz), as the probability evolutions show in Fig. S5a. Then, we perform QPT measurement dependent on the offset of  $t_{\sqrt{\text{iSWAP}}}$  and zpa of Q<sub>20</sub>, with the calculated fidelities plotted in Fig. S5b and c, respectively. Fidelities of all 36 characteristic input states with error bars after optimization are shown in Fig. S5d, yielding a gate fidelity over 0.98.

Table S2: Characteristics of two-qubit  $\sqrt{i\text{SWAP}}$  gates. Working points ( $\omega_I$ ), characteristic gate times ( $t_{\sqrt{i\text{SWAP}}}$ ) and gate fidelities ( $F$ ) estimated by quantum process tomography (QPT) for the four two-qubit gates used in our experiments.

	H <sub>2</sub> and polyacenes		CO	
	Q <sub>14</sub> -Q <sub>20</sub>	Q <sub>3</sub> -Q <sub>6</sub>	Q <sub>3</sub> -Q <sub>13</sub>	Q <sub>6</sub> -Q <sub>20</sub>
$\omega_I/2\pi$ (GHz)	5.160	5.190	5.170	5.130
$t_{\sqrt{i\text{SWAP}}}$ (ns)	43.8	43.5	48.1	56.6
$F$	$0.9806 \pm 0.0012$	$0.9766 \pm 0.0005$	$0.9679 \pm 0.0061$	$0.9508 \pm 0.0050$

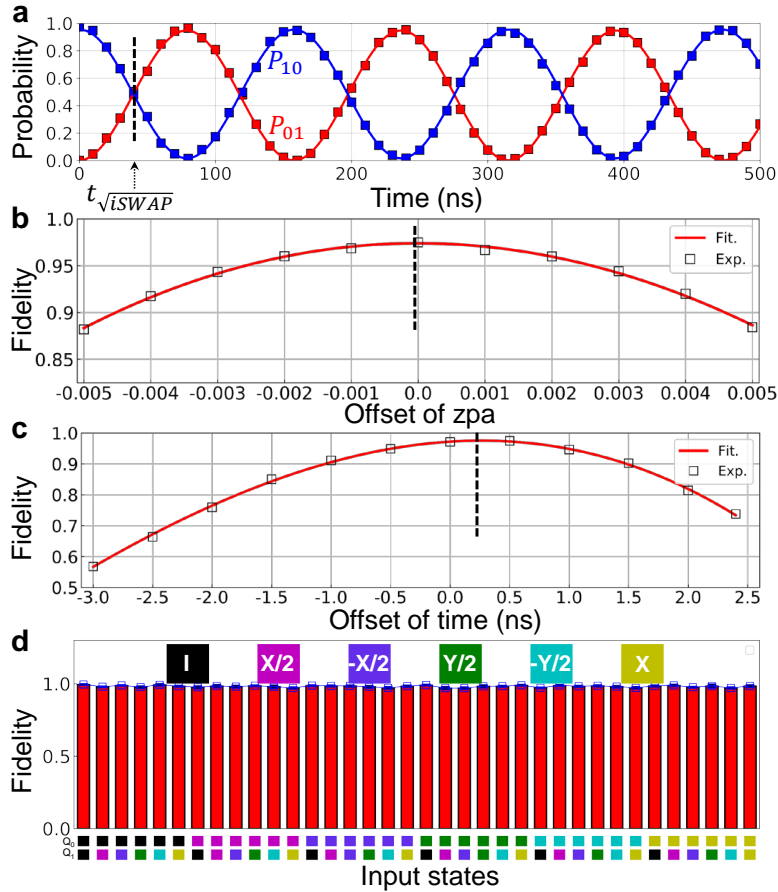


**Fig. S5. Optimization of the  $\sqrt{i\text{SWAP}}$  gate by QPT.** a, Superexchange interaction for Q<sub>14</sub>-Q<sub>20</sub>. A characteristic gate time  $t_{\sqrt{i\text{SWAP}}}$  can be identified by the time-modulated probabilities  $P_{10}$  (blue squares) and  $P_{01}$  (red squares) for state  $|10\rangle$  and  $|01\rangle$ , respectively. b,c, Gate fidelity with the change of zpa and interaction time  $t_{\sqrt{i\text{SWAP}}}$ . The blank squares are experimental results and the red lines are fitted data. d, The calculated fidelities for 36 input states  $\otimes_j^{n=2} \{I, \pm X/2, \pm Y/2, X\}$ .

## S3 Two-qubit simulations for H<sub>2</sub> and polyacenes

### S3.1 Fermion-to-qubit mapping and wavefunction ansätze

The two-qubit simulations are carried out for H<sub>2</sub> in the STO-3G basis and polyacenes within a two-electron-in-two-orbital active space model including the highest occupied molecular orbital (HOMO) and the lowest unoccupied molecular orbital (LUMO). The prototypical molecule H<sub>2</sub> is investigated at three bond distances,  $R_e$ ,  $2R_e$ , and  $3R_e$ , where  $R_e = 0.74144 \text{ \AA}$  is the experimental equilibrium bond distance (38). Geometries of polyacenes are optimized at the density functional theory (DFT) level of theory using the B3LYP (63, 64) hybrid functional and the 6-31G\* basis set. For these two kinds of systems, the molecular orbitals obtained from spin-restricted Hartree-Fock (RHF) calculations are taken as the one-electron orbital basis for quantum simulations based on second quantization.

Consider H<sub>2</sub> as example, the Bravyi-Kitaev (BK) transformation (29, 30) leads to the following mapping of occupation number vectors (ONVs),

$$\begin{aligned} |n_0 n_1 n_2 n_3\rangle &= |n_g n_u n_{\bar{g}} n_{\bar{u}}\rangle \\ \rightarrow |n_g(n_u + n_g \bmod 2) n_{\bar{g}}(n_{\bar{u}} + n_{\bar{g}} + n_u + n_g \bmod 2)\rangle &= |n_g p_e^\alpha n_{\bar{g}} p_e\rangle. \end{aligned} \quad (\text{S33})$$

where  $n \in \{0, 1\}$  denotes the occupation of an molecular spin-orbital (MO),  $g$  ( $u$ ) refers to the MO with gerade (ungerade) symmetry due to the existence of inversion symmetry in H<sub>2</sub>,  $p_e$  ( $p_e^\alpha$ ) represents the parity of the number of total (alpha) electrons  $N_e$  ( $N_e^\alpha$ ). For particle number and spin projection conserving Hamiltonian, we can restrict the space of interest to the subspace with well-defined  $p_e$  and  $p_e^\alpha$ . This is referred as the  $Z_2$  reduction (50), which enables the removal of two qubits. The final ONV of qubits after the  $Z_2$  reduction becomes

$$|q_0 q_1\rangle = |n_g n_{\bar{g}}\rangle, \quad (\text{S34})$$

which implies the following mapping of determinants with  $N_e = 2$  and  $N_e^\alpha = 1$  to ONVs of

qubits

$$|g\bar{g}\rangle \rightarrow |11\rangle, \quad |u\bar{u}\rangle \rightarrow |00\rangle, \quad |g\bar{u}\rangle \rightarrow |10\rangle, \quad |u\bar{g}\rangle \rightarrow |01\rangle. \quad (\text{S35})$$

The same mapping works for polyacenes within the active space model, except that the labels  $g$  and  $u$  will interchange for HOMO and LUMO, depending on the number of rings, see Fig. 4 in the main text.

The ground state is in the subspace  $V_g = \{|g\bar{g}\rangle, |u\bar{u}\rangle\} = \{|11\rangle, |00\rangle\}$ , while the response state for the dipole perturbation  $\hat{V} = \hat{z}$  resides in the subspace  $V_u = \{|g\bar{u}\rangle, |u\bar{g}\rangle\} = \{|10\rangle, |01\rangle\}$ . The wavefunction ansatz shown in Fig. 3a in the main text gives a parameterization

$$|\Psi(\theta_0)\rangle = U_0(\theta_0)|0\rangle = |11\rangle \cos(\theta_0/2) + |00\rangle \sin(\theta_0/2), \quad (\text{S36})$$

up to an irrelevant global phase. The ansatz for  $|x(\theta_1)\rangle$  in Fig. 3c for the dipole perturbation  $\hat{V} = \hat{z}$  gives

$$|x(\theta_1)\rangle = U_1(\theta_1)|0\rangle = X_1 U_0(\theta_1)|0\rangle = |10\rangle \cos(\theta_1/2) + |01\rangle \sin(\theta_1/2), \quad (\text{S37})$$

up to a global phase. These are exact parameterizations for the ground and response states. In particular, the exact response state can always be found at  $\theta_1 = \pi/2$  due to spin symmetry, as  $|x(\theta_1 = \pi/2)\rangle = \frac{1}{\sqrt{2}}(|10\rangle + |01\rangle)$  corresponds to the singlet excited state due to the single excitation from  $g$  to  $u$ .

### S3.2 Details of VQR algorithm

The Hamiltonian  $\hat{H}_0$  after the BK mapping with the  $Z_2$  reduction reads

$$\hat{H}_0 = h_0 I + h_1 Z_0 + h_2 Z_1 + h_3 Z_0 Z_1 + h_4 X_0 X_1. \quad (\text{S38})$$

For the dipole perturbation  $\hat{V} = \hat{z} = z_{ug}(a_u^\dagger a_g + a_u^\dagger a_{\bar{g}}) + \text{h.c.}$  with  $z_{ug} = \langle u|\hat{z}|g\rangle$ , the corresponding qubit operator after the BK transformation and the  $Z_2$  reduction becomes

$$\hat{V} = v_0(X_0 + X_1), \quad v_0 = z_{ug}, \quad (\text{S39})$$

The coefficients  $h_k$  and  $v_0$  for different systems are summarized in Table S3.

Table S3: Coefficients (in atomic unit) of Pauli operators in  $\hat{H}_0$  Eq. (S38) and  $\hat{V}$  Eq. (S39) for  $H_2$  at different bond distances  $R = sR_e$  ( $s = 1, 2, 3$ ) and polyacenes with different number of rings ( $n = 2, 3, 4, 5$ ).

	$H_2$			polyacenes			
	$s = 1$	$s = 2$	$s = 3$	$n = 2$	$n = 3$	$n = 4$	$n = 5$
$h_0 (h_{II})$	-1.053716	-1.012393	-0.895897	-0.611117	-0.558265	-0.524089	-0.499055
$h_1 (h_{ZI})$	0.393959	0.132405	0.042584	0.098308	0.077231	0.062505	0.051971
$h_2 (h_{IZ})$	0.393959	0.132405	0.042584	0.098308	0.077231	0.062505	0.051971
$h_3 (h_{ZZ})$	0.011236	0.004326	0.000815	0.001972	0.001323	-0.000958	0.000731
$h_4 (h_{XX})$	0.181291	0.228430	0.270319	0.044417	0.037979	0.034403	0.032027
$v_0$	-0.931343	-1.452302	-2.108703	1.444951	1.510664	1.593675	1.680618

With Eqs. (S38) and (S39), the following expansions can be found

$$\hat{V}^\dagger \hat{V} = w_0 I + w_1 X_0 X_1, \quad (\text{S40})$$

$$\hat{A}(\omega) = h'_0(\omega) I + h_1 Z_0 + h_2 Z_1 + h_3 Z_0 Z_1 + h_4 X_0 X_1, \quad (\text{S41})$$

$$\hat{A}^\dagger(\omega) \hat{A}(\omega) = b_0(\omega) I + b_1(\omega) Z_0 + b_2(\omega) Z_1 + b_3(\omega) Z_0 Z_1 + b_4(\omega) X_0 X_1 + b_5(\omega) Y_0 Y_1, \quad (\text{S42})$$

$$\begin{aligned} \hat{V}^\dagger \hat{A}(\omega) &= v_0 [(h'_0(\omega) X_0 + h_1(-iY_0) + h_2 X_0 Z_1 + h_3(-iY_0) Z_1 + h_4 X_1) \\ &\quad + (h'_0(\omega) X_1 + h_1 X_1 Z_0 + h_2(-iY_1) + h_3 Z_0(-iY_1) + h_4 X_0)], \end{aligned} \quad (\text{S43})$$

where  $h'_0(\omega) = h_0 - E_0 - (\omega + i\gamma)$ . For  $\langle \Psi_0 | \hat{V}^\dagger \hat{A}(\omega) | x \rangle$ , where  $|\Psi_0\rangle \in V_g$  and  $|x\rangle \in V_u$ , an effective operator  $(\hat{V}^\dagger \hat{A}(\omega))_{\text{eff}}$ , which leads to the same matrix element, can be obtained from  $\hat{V}^\dagger \hat{A}(\omega)$  by the replacements  $X_i Z_j \rightarrow iY_i$  and  $Y_i Z_j \rightarrow -iX_i$  ( $i \neq j$ ). Together with the condition  $h_1 = h_2$ , this leads to

$$(\hat{V}^\dagger \hat{A}(\omega))_{\text{eff}} = v_0 [h'_0(\omega) - h_3 + h_4] (X_0 + X_1) \equiv c_0(\omega) (X_0 + X_1). \quad (\text{S44})$$

The coefficients of Pauli operators in  $\hat{A}^\dagger(\omega) \hat{A}(\omega)$  and  $(\hat{V}^\dagger \hat{A}(\omega))_{\text{eff}}$  are summarized in Table S4.

Using Eqs. (S44) and (S29), the cross term in Eq. (S23) can be expressed as

$$\begin{aligned} |\langle \Psi_0 | \hat{V}^\dagger \hat{A}(\omega) | x \rangle|^2 &= |c_0(\omega)|^2 |\langle \Psi_0 | (X_0 + X_1) | x \rangle|^2 \\ &= |c_0(\omega)|^2 (|\langle \Psi_0 | X_0 | x \rangle|^2 + |\langle \Psi_0 | X_1 | x \rangle|^2 + 2\text{Re}(\langle \Psi_0 | X_0 | x \rangle \langle x | X_1 | \Psi_0 \rangle)) \\ &= 4|c_0(\omega)|^2 |\langle 0 | U_0^\dagger R_{x,0}(\frac{\pi}{2}) R_{x,1}(\frac{\pi}{2}) U_1 | 0 \rangle|^2. \end{aligned} \quad (\text{S45})$$

This simple expression only requires the quantum circuit shown in Fig. 3b in the main text to construct the cross term.

Table S4: Expressions for the coefficients of Pauli operators in  $\hat{A}^\dagger(\omega)\hat{A}(\omega)$  (S42) and  $(\hat{V}^\dagger\hat{A}(\omega))_{\text{eff}}$  (S44) for the two-qubit problem.

	expressions
$b_0(\omega)$ ( $b_{II}(\omega)$ )	$\gamma^2 + (h_{II} - E_0 - \omega)^2 + h_{IZ}^2 + h_{ZI}^2 + h_{ZZ}^2 + h_{XX}^2$
$b_1(\omega)$ ( $b_{ZI}(\omega)$ )	$2[h_{ZI}(h_{II} - E_0 - \omega) + h_{IZ}h_{ZZ}]$
$b_2(\omega)$ ( $b_{IZ}(\omega)$ )	$2[h_{IZ}(h_{II} - E_0 - \omega) + h_{ZI}h_{ZZ}]$
$b_3(\omega)$ ( $b_{ZZ}(\omega)$ )	$2[h_{ZZ}(h_{II} - E_0 - \omega) + h_{IZ}h_{ZI}]$
$b_4(\omega)$ ( $b_{XX}(\omega)$ )	$2h_{XX}(h_{II} - E_0 - \omega)$
$b_5(\omega)$ ( $b_{YY}(\omega)$ )	$-2h_{XX}h_{ZZ}$
$c_0(\omega)$	$v_0[h_{II} - h_{ZZ} + h_{XX} - E_0 - (\omega + i\gamma)]$

### S3.3 Error mitigation via spatial symmetry projection

For the subspaces  $V_g$  and  $V_u$ , the symmetry projectors can be found as

$$\mathcal{P}_g = |00\rangle\langle 00| + |11\rangle\langle 11| = \frac{1}{4}[(I_1 + Z_1)(I_0 + Z_0) + (I_1 - Z_1)(I_0 - Z_0)] = \frac{1}{2}(I + Z_0Z_1) \quad (\text{S46})$$

$$\mathcal{P}_u = |01\rangle\langle 01| + |10\rangle\langle 10| = \frac{1}{4}[(I_1 + Z_1)(I_0 - Z_0) + (I_1 - Z_1)(I_0 + Z_0)] = \frac{1}{2}(I - Z_0Z_1) \quad (\text{S47})$$

For the ground state, instead of computing  $E_0$  from  $|\Psi_0\rangle$  via

$$E_0^{\text{raw}} = \langle \Psi_0 | \hat{H}_0 | \Psi_0 \rangle = h_{II} + h_{IZ}(\langle I_1 Z_0 \rangle + \langle Z_1 I_0 \rangle) + h_{ZZ}\langle Z_1 Z_0 \rangle + h_{XX}\langle X_1 X_0 \rangle + h_{YY}\langle Y_1 Y_0 \rangle \quad (\text{S48})$$

an improved error-mitigated (EM) estimator with the symmetry-projected state  $|\tilde{\Psi}_0\rangle = \frac{\mathcal{P}_g|\Psi_0\rangle}{\sqrt{\langle \Psi_0 | \mathcal{P}_g | \Psi_0 \rangle}}$

can be derived using

$$\hat{H}_0 Z_1 Z_0 = h_{II} Z_1 Z_0 + h_{IZ}(Z_1 I_0 + I_1 Z_0) + h_{ZZ} I_1 I_0 - h_{XX} Y_1 Y_0 - h_{YY} X_1 X_0, \quad (\text{S49})$$

such that

$$\begin{aligned} E_0^{\text{EM}} &= \langle \tilde{\Psi}_0 | \hat{H}_0 | \tilde{\Psi}_0 \rangle = \frac{\langle \Psi_0 | \hat{H}_0 \mathcal{P}_g | \Psi_0 \rangle}{\langle \Psi_0 | \mathcal{P}_g | \Psi_0 \rangle} \\ &= (h_{II} + h_{ZZ}) + \frac{2h_{IZ}(\langle I_1 Z_0 \rangle + \langle Z_1 I_0 \rangle) + (h_{XX} - h_{YY})(\langle X_1 X_0 \rangle - \langle Y_1 Y_0 \rangle)}{1 + \langle Z_1 Z_0 \rangle} \quad (\text{S50}) \end{aligned}$$

using the commutativity property  $[\mathcal{P}_g, \hat{H}_0] = 0$ . The same strategy can be applied to estimate  $\langle \Psi_0 | \hat{V}^\dagger \hat{V} | \Psi_0 \rangle$  in Eq. (S40).

For  $\langle x | \hat{A}^\dagger(\omega) \hat{A}(\omega) | x \rangle$  and  $\langle x | \hat{A}^\dagger(\omega) | x \rangle$  required in the VQR calculations,  $\mathcal{P}_u$  in Eq. (S47) can be used in a similar way. Consider the quantity  $\langle x | \hat{A}^\dagger(\omega) \hat{A}(\omega) | x \rangle$  as example, which is crucial for computing the imaginary part of  $\chi(\omega)$  in Eq. (S16),

$$\langle x | \hat{A}^\dagger(\omega) \hat{A}(\omega) | x \rangle^{\text{raw}} = b_{II} + b_{IZ}(\langle I_1 Z_0 \rangle + \langle Z_1 I_0 \rangle) + b_{ZZ} \langle Z_1 Z_0 \rangle + b_{XX} \langle X_1 X_0 \rangle + b_{YY} \langle Y_1 Y_0 \rangle \quad (\text{S51})$$

The error mitigated estimator with  $\mathcal{P}_u$  is

$$\langle x | \hat{A}^\dagger(\omega) \hat{A}(\omega) | x \rangle^{\text{EM}} = \frac{\langle x | \hat{A}^\dagger(\omega) \hat{A}(\omega) \mathcal{P}_u | x \rangle}{\langle x | \mathcal{P}_u | x \rangle} = (b_{II} - b_{ZZ}) + \frac{(b_{XX} + b_{YY})(\langle X_1 X_0 \rangle + \langle Y_1 Y_0 \rangle)}{1 - \langle Z_1 Z_0 \rangle} \quad (\text{S52})$$

In our experiments, to improve the accuracy this expression is used in both estimating  $\langle x | \hat{A}^\dagger(\omega) \hat{A}(\omega) | x \rangle$  in the cost function  $L(\theta_1)$  in Eq. (S10) as well as estimating  $\langle x | \hat{A}^\dagger(\omega) \hat{A}(\omega) | x \rangle$  and  $\langle x | \hat{A}^\dagger(\omega) | x \rangle$  for  $\chi(\omega)$  in Eq. (S14).

### S3.4 VQE experiments

To find the ground state, we perform VQE experiments by scanning the entire parameter space. The individual terms  $\langle \Psi_0(\theta_0) | P | \Psi_0(\theta_0) \rangle$  with  $P \in \{Z_0, Z_1, Z_1 Z_0, X_1 X_0, Y_1 Y_0\}$  at a list of angles  $\theta_0 \in [0, 2\pi)$  are computed by preparing  $|\Psi_0(\theta_0)\rangle$  using the circuit shown in Fig. 3a in the main text and adding appropriate post-rotations ( $I$ ,  $-X/2$  or  $Y/2$ ) for polarizations along different axes before measurements. Considering these estimates would be affected by stochastic fluctuations due to finite samplings, we maintain a fixed sample size of 60000 and repeat 5 times for estimating the mean values and standard deviations of each  $\langle \Psi_0(\theta_0) | P | \Psi_0(\theta_0) \rangle$  at a given  $\theta_0$ . The obtained results are shown in Fig. S6.

With the expansion for  $\hat{H}_0$  in Eq. (S38),  $E(\theta_0)$  can be computed using Eq. (S50) with EM to find the optimal angle  $\theta_0^{\text{opt}}$  corresponding to the position of the minimum of  $E(\theta_0)$ . The results are summarized in Table S5. It is seen that for all systems we studied, the error-mitigated

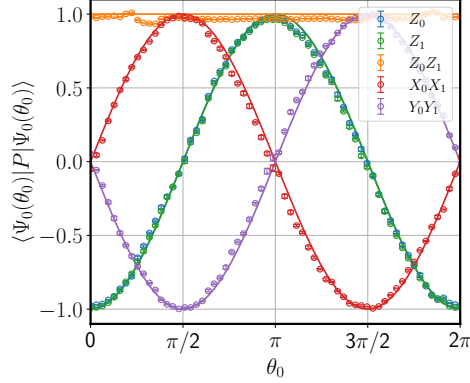


**Fig. S6. Measured expectation values  $\langle \Psi_0(\theta_0) | P | \Psi_0(\theta_0) \rangle$  of Pauli operators with respect to the ground state  $|\Psi_0(\theta_0)\rangle$  for VQE calculations.** The theoretical values are shown as solid lines, while the experimental results are shown in open circles. Error bars are smaller than the markers.

energies  $E_0^{\text{EM}}$  in Eq. (S50) are closer to the exact values than the raw energies  $E_0^{\text{raw}}$  in Eq. (S48). The accuracy of  $E_0^{\text{EM}}$  is on the order of the chemical accuracy (ca. 1 milli-Hartree). We also characterize the obtained ground states by quantum state tomography (33, 60) (QST). The ideal and measured density matrices are compared in Fig. S7. The similarity between the ideal ( $\rho_{\text{ideal}}$ ) and experimental ( $\rho_{\text{exp}}$ ) density matrices is quantified by the state fidelity (60)  $F(\rho_{\text{ideal}}, \rho_{\text{exp}}) = \text{tr}(\sqrt{\sqrt{\rho_{\text{ideal}}}\rho_{\text{exp}}\sqrt{\rho_{\text{ideal}}}})$ . For all cases, the values of  $F$  are greater than 0.990. With the determined ground states, we can evaluate the expectation values  $\langle \Psi_0 | \hat{V}^\dagger \hat{V} | \Psi_0 \rangle$  for later VQR calculations. As shown in Table S5, similar to the energies, the error-mitigated results for  $\langle \Psi_0 | \hat{V}^\dagger \hat{V} | \Psi_0 \rangle$  are significantly better than the raw results. This demonstrates the effectiveness of EM via symmetry projection also for properties other than energies.

### S3.5 VQR experiments

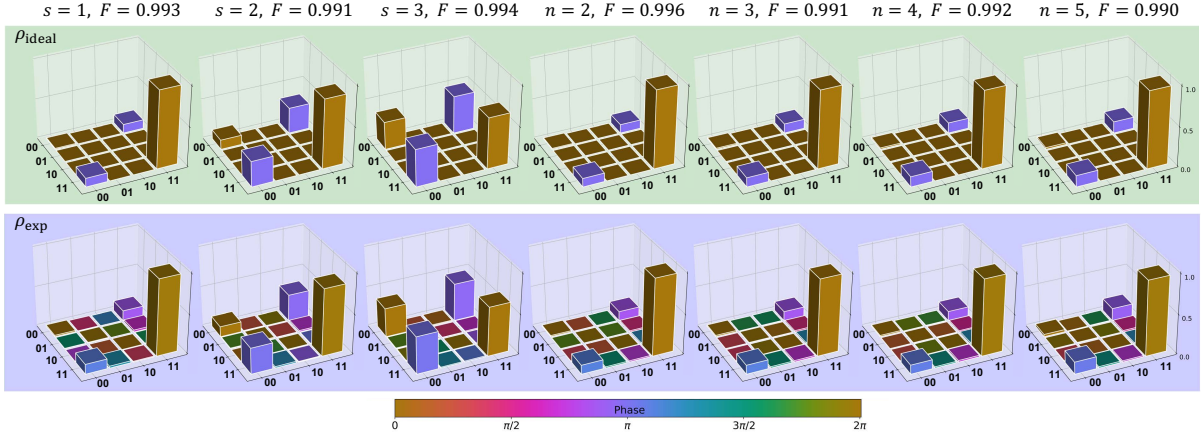
The VQR calculations start with constructing the cost function  $L(\theta_1)$  in Eq. (S10) for each interested frequency  $\omega$ . To construct  $\langle x | \hat{A}^\dagger(\omega) \hat{A}(\omega) | x \rangle$  in the cost function  $L(\theta_1)$ , we first measured the individual terms  $\langle x(\theta_1) | P | x(\theta_1) \rangle$  with  $P \in \{Z_0, Z_1, Z_1 Z_0, X_1 X_0, Y_1 Y_0\}$  at a list of angles

Table S5: VQE results for the ground states of  $H_2$  at different bond distances  $R = sR_e$  ( $s = 1, 2, 3$ ) and polyacenes with different number of rings ( $n = 2, 3, 4, 5$ ).  $\theta_0^*$ : theoretical angle,  $\theta_0^{\text{opt}}$ : VQE optimized angle,  $F$ : fidelity of the VQE ground state,  $E_0^*$ : theoretical ground-state energy,  $E_0^{\text{raw}}$ : raw energy in Eq. (S48),  $E_0^{\text{EM}}$ : error-mitigated energy in Eq. (S50).

	$H_2$			polyacenes			
	$s = 1$	$s = 2$	$s = 3$	$n = 2$	$n = 3$	$n = 4$	$n = 5$
$\theta_0^*$	6.0570	5.5714	5.0176	6.0610	6.0421	6.0146	5.9843
$\theta_0^{\text{opt}}$	6.0502	5.5481	4.9902	6.0494	6.0337	6.0034	5.9704
$F$	0.993	0.991	0.994	0.996	0.991	0.992	0.990
$E_0^*$	-1.85099	-1.35779	-1.17850	-0.81072	-0.71600	-0.65279	-0.60709
$E_0^{\text{raw}}$	-1.83785	-1.34957	-1.17368	-0.80822	-0.71202	-0.64977	-0.60421
$E_0^{\text{EM}}$	-1.84563	-1.35669	-1.17625	-0.80924	-0.71431	-0.65172	-0.60591
$\langle \Psi_0   \hat{V}^\dagger \hat{V}   \Psi_0 \rangle^*$	1.34575	1.46295	0.41024	3.25560	3.47443	3.73180	3.98554
$\langle \Psi_0   \hat{V}^\dagger \hat{V}   \Psi_0 \rangle^{\text{raw}}$	1.37122	1.53765	0.64011	3.31827	3.66090	3.82275	4.13154
$\langle \Psi_0   \hat{V}^\dagger \hat{V}   \Psi_0 \rangle^{\text{EM}}$	1.34519	1.43912	0.40241	3.27984	3.59898	3.75911	4.07832

$\theta_1 \in [0, 2\pi)$ . To compute the cross term in Eq. (S45), the quantity  $|\langle 0 | U_0^\dagger(\theta_0^{\text{opt}}) R_{x,0}(\frac{\pi}{2}) R_{x,1}(\frac{\pi}{2}) U_1(\theta_1) | 0 \rangle|^2$  are measured using the circuit shown in Fig. 3c at the same list of  $\theta_1$ , with  $\theta_0^{\text{opt}}$  obtained in the previous VQE experiments (see Table S5). The experimental results are depicted in Fig. S8. The errors of  $|\langle 0 | U_0^\dagger(\theta_0^{\text{opt}}) R_{x,0}(\frac{\pi}{2}) R_{x,1}(\frac{\pi}{2}) U_1(\theta_1) | 0 \rangle|^2$  are larger than those for  $\langle x(\theta_1) | P | x(\theta_1) \rangle$ , due to the doubling of the number of two-qubit gates and the longer circuit length.

The experimentally determined  $\langle \Psi_0 | \hat{V}^\dagger \hat{V} | \Psi_0 \rangle \langle x | \hat{A}(\omega) \hat{A}(\omega) | x \rangle$  (green),  $\langle \Psi_0 | \hat{V}^\dagger \hat{A}(\omega) | x \rangle|^2$  (blue), and cost function  $L(\theta_1)$  (black) are shown in Fig. S9 for  $H_2$  at different bond lengths  $R = sR_e$  ( $s = 1, 2, 3$ ), and Fig. S10 for polyacenes with different number of rings ( $n = 2, 3, 4, 5$ ). The position of the red vertical dashed line shows the optimized angle  $\theta_1^{\text{opt}}$  from a local quadratic fitting (red line) around the minimum for  $L(\theta_1)$ . The theoretical angle (black vertical line) is always  $\theta_1^* = \frac{\pi}{2}$  as discussed after Eq. (S37). It is seen that in certain cases such as  $H_2$  at  $R = R_e$  with  $\omega = 0.6$ ,  $\theta_1^{\text{opt}}$  deviates from  $\theta_1^*$ . We find that this happens when  $\omega$  is close to the triplet excitation energy  $\omega_T$ , where the blue and green curves are very close to each other such that the resulting cost functions in Eq. (S10) as the difference between these two curves are very sensitive to experimental errors due to noises. The triplet excitation energies



**Fig. S7.** QST for the VQE ground states of  $\text{H}_2$  at  $R = sR_e$  ( $s = 1, 2, 3$ ) and polyacenes with different number of rings ( $n = 2, 3, 4, 5$ ). Upper row: ideal density matrices  $\rho_{\text{ideal}}$ ; Lower row: experimental density matrices  $\rho_{\text{exp}}$ .

$\omega_T$  (in a.u.) are 0.605, 0.113, 0.011, 0.153, 0.118, 0.093, and 0.075 for  $\text{H}_2$  at different bond lengths  $R = sR_e$  ( $s = 1, 2, 3$ ) and polyacenes with different number of rings ( $n = 2, 3, 4, 5$ ), respectively. Therefore, we can observe similar deviations around  $\omega_T$  in other cases in Figs. S9 and S10, except for the later two systems (tetracene and pentacene), where  $\omega_T$  does not lie in the energy window we are interested in, and hence do not affect the optimization, see Figs. S10c and S10d.

Finally, with the optimized  $\theta_1^{\text{opt}}$  at each frequency point  $\omega$ , we can compute  $\chi(\omega)$  from Eq. (S14) by preparing  $|x(\theta_1^{\text{opt}})\rangle$  and computing  $\langle x|\hat{A}^\dagger(\omega)|x\rangle$  and  $\langle x|\hat{A}^\dagger(\omega)\hat{A}(\omega)|x\rangle$  using the error mitigation technique shown in Eq. (S52). The results are given in Figs. 3 and 4 for  $\text{H}_2$  and polyacenes, respectively.

### S3.6 Additional results from quantum chemistry calculations

#### S3.6.1 Dipole polarizabilities of $\text{H}_2$ from FCI, HF, and DFT

In Fig. S11, we compare  $\chi(\omega)$  computed using standard quantum chemistry methods including FCI, HF, and DFT with two representative exchange-correlation functionals (LDA and B3LYP)

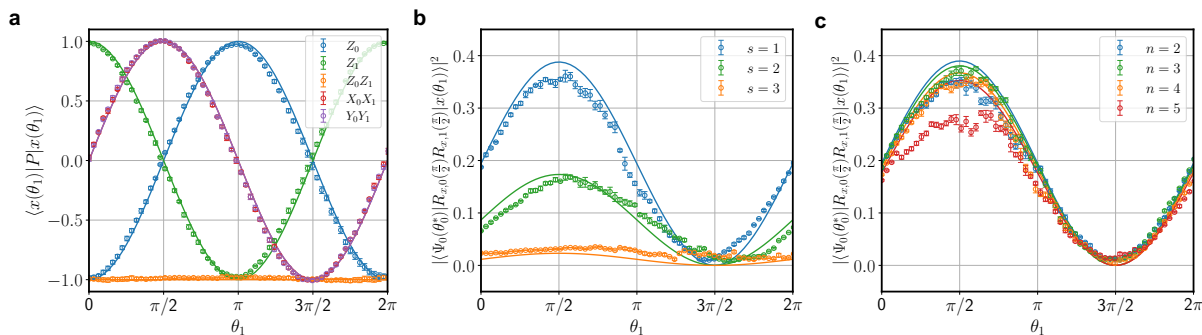


**Fig. S8. Experimental results for the construction of VQR cost function  $L(\theta_1)$  in Eq. (S10) for  $H_2$  at different bond distances  $R = sR_e$  ( $s = 1, 2, 3$ ) and polyacenes with different number of rings ( $n = 2, 3, 4, 5$ ).** a, Measured expectation values  $\langle x(\theta_1) | P | x(\theta_1) \rangle$  of Pauli operators with respect to the response state  $|x(\theta_1)\rangle$ . The theoretical values are shown as solid lines, while the experimental results are shown in open circles. Error bars are smaller than the markers. b,c, Measured  $|\langle 0 | U_0^\dagger(\theta_0^{\text{opt}}) R_{x,0}(\frac{\pi}{2}) R_{x,1}(\frac{\pi}{2}) U_1(\theta_1) | 0 \rangle|^2$  with  $\theta_0^{\text{opt}}$  in Table S5.

for  $H_2$  at  $R = sR_e$  ( $s = 1, 2, 3$ ), using a locally modified version of the PySCF package (51). It is seen that at the equilibrium HF and DFT give similar results, which are close to the FCI reference, and the spin-restricted and spin-unrestricted results coincide with each other for a given method, as symmetry breaking does not happen in the spin-unrestricted methods. However, at the stretched geometries ( $s = 2$  and  $s = 3$ ), where the electron correlation becomes much stronger than that at the equilibrium, both HF and DFT in either spin-restricted or spin-unrestricted fail even qualitatively.

### S3.6.2 Estimation of dynamic correlation by perturbation theory for polyacenes

Since we adopted the active space approximation for polyacenes, the interaction between the active electrons and the frozen electrons are only treated at the mean-field level. The neglected dynamic correlation can affect the accuracy of the computed spectra. To estimate the magnitude of such effects, we compute the first excited state using the  $N$ -electron valence state perturbation theory (65) (NEVPT2) based on a complete active space configuration interaction (CASCI) reference with the RHF orbitals. The lowering of CASCI excitation energies are found to be

-1.96 eV, -1.95 eV, -1.91 eV, and -1.85 eV for naphthalene ( $n = 2$ ), anthracene ( $n = 3$ ), tetracene ( $n = 4$ ), and pentacene ( $n = 5$ ), respectively. Thus, as a rough estimation of the effects of dynamic correlation on the computed spectra within the active space, we shift all the spectra by a constant -1.9 eV. The obtained results are in good agreement with the experimental spectra, see Fig. 4. The remaining discrepancy is mainly due to the lack of the treatment of nuclear degrees of freedom, which contribute to the vibrational structures of the experimental spectra. The simulation of vibrationally resolved electronic spectra will be a subject of future study.

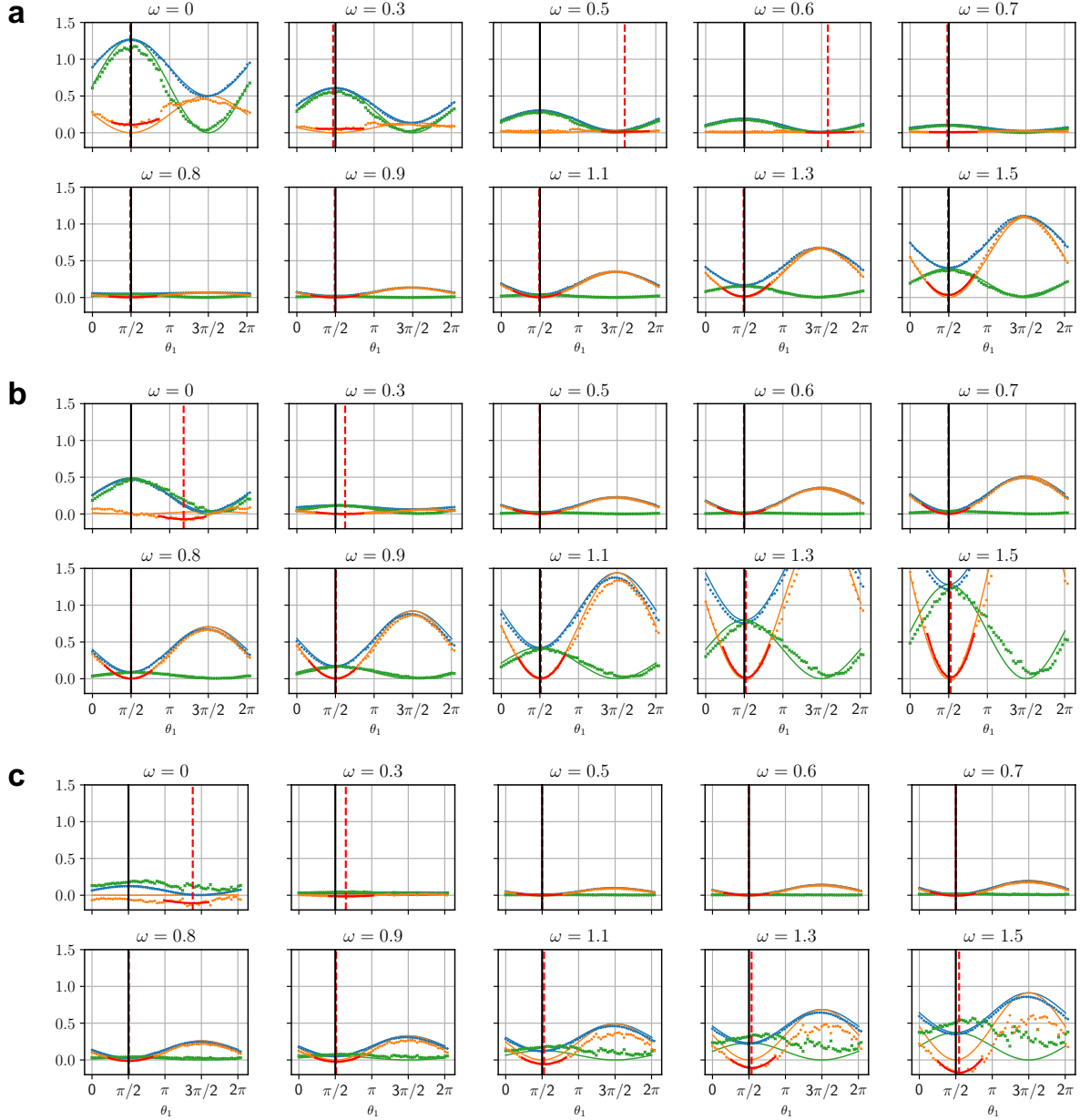


**Fig. S9.** Experimental  $\langle \Psi_0 | \hat{V}^\dagger \hat{V} | \Psi_0 \rangle \langle x | \hat{A}(\omega) \hat{A}(\omega) | x \rangle$  (blue dots),  $\langle \Psi_0 | \hat{V}^\dagger \hat{A}(\omega) | x \rangle^2$  (green dots), and cost function  $L(\theta_1)$  (orange dots) at ten representative frequencies  $\omega$  (in a.u.) for  $\text{H}_2$  at  $R = sR_e$  (a,b,c, for  $s = 1, 2, 3$ ). For comparison, the theoretical curves are shown in solid lines. The red solid line represents the fitted quadratic curve around the minimum for determining the optimal angle  $\theta_1^{\text{opt}}$  (red vertical dashed line). The theoretical angle  $\theta_1^* = \frac{\pi}{2}$  is represented by the black vertical line.

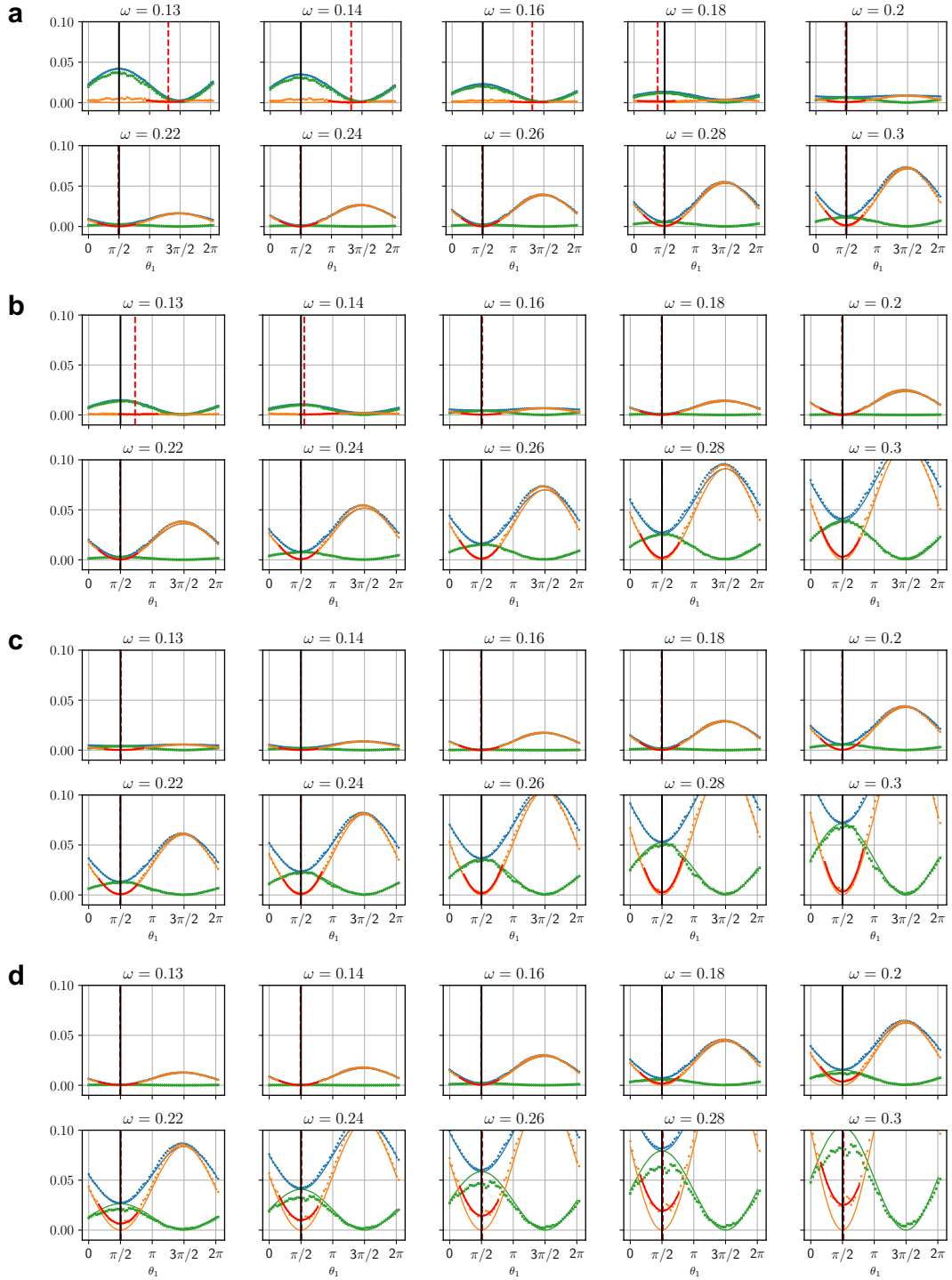


**Fig. S10.** Experimental  $\langle \Psi_0 | \hat{V}^\dagger \hat{V} | \Psi_0 \rangle \langle x | \hat{A}(\omega) \hat{A}(\omega) | x \rangle$  (blue dots),  $\langle \Psi_0 | \hat{V}^\dagger \hat{A}(\omega) | x \rangle^2$  (green dots), and cost function  $L(\theta_1)$  (orange dots) at ten representative frequencies  $\omega$  (in a.u.) for polyacenes with different number of rings (a,b,c,d for  $n = 2, 3, 4, 5$ ). For other explanations, see Fig. S9.

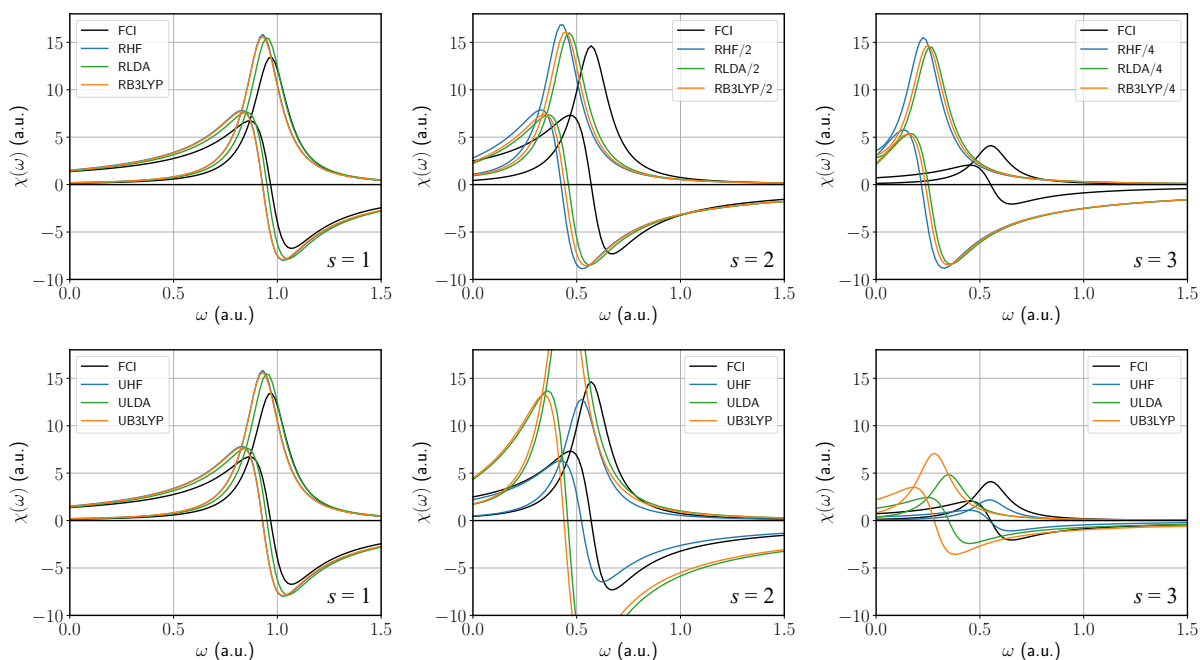


**Fig. S11.** Comparison of  $\chi(\omega)$  computed using standard quantum chemistry methods including FCI, HF, and DFT with two representative exchange-correlation functionals (LDA and B3LYP) for  $\text{H}_2$  at  $R = sR_e$  ( $s = 1, 2, 3$ ). Upper panel: spin-restricted (R) methods; Lower panel: spin-unrestricted (U) methods. For  $s = 2$  and  $s = 3$ , the results obtained with spin restricted methods are scaled by a factor of  $1/2$  and  $1/4$ , respectively, in order to fit into the figure.

## S4 Four-qubit simulations for CO

### S4.1 Fermion-to-qubit mapping and wavefunction ansatz

The carbon K-edge and oxygen K-edge absorption spectra of CO are simulated with a four-electron-in-three-orbital active space model including  $\sigma_{1s_O}$ ,  $\sigma_{1s_C}$ , and  $\pi_x^*$  orbitals obtained from RHF calculations with the STO-3G basis at the equilibrium bond length  $R_e = 1.128323 \text{ \AA}$  (38). To simplify the later simulations, we replace the active space Hamiltonian  $\hat{H}_0$  in Eq. (S3) by a simplified one, in which only the molecular integrals  $[p|h|p]$  and  $[pp|qq]$  are kept,

$$\hat{H}_0 = \sum_p [p|h|p] a_p^\dagger a_p + \sum_{pq} \frac{1}{2} [pp|qq] a_p^\dagger a_q^\dagger a_q a_p, \quad (\text{S53})$$

where the constant  $E_{\text{NN}}$  is removed for simplicity, since it does not affect the energy difference. This is a very good approximation due to the localized nature of the core orbitals,  $\sigma_{1s_O}$  and  $\sigma_{1s_C}$ . The computed excitation energies from this approximate Hamiltonian are  $\omega_C = 290.74 \text{ eV}$  and  $\omega_O = 547.55 \text{ eV}$  for the singlet excited states dominated by  $\sigma_{1s_C} \rightarrow \pi^*$  and  $\sigma_{1s_O} \rightarrow \pi^*$ , respectively, in close agreement with the values from the original active space Hamiltonian,  $\omega_C = 290.94 \text{ eV}$  and  $\omega_O = 547.36 \text{ eV}$ . The Hartree-Fock (HF) state  $|\Psi_{\text{HF}}\rangle = |\sigma_{1s_O} \sigma_{1s_C} \bar{\sigma}_{1s_O} \bar{\sigma}_{1s_C}\rangle$  is the ground state  $|\Psi_0\rangle$  of the Hamiltonian in Eq. (S53). Within the four-electron-in-three-orbital active space model, any singlet state with  $\Pi_x$  symmetry can be *exactly* parameterized by

$$|x(\theta, \phi)\rangle = \cos \frac{\theta}{2} |^1\Psi_{\sigma_{1s_O} \rightarrow \pi_x^*}\rangle + \sin \frac{\theta}{2} e^{i\phi} |^1\Psi_{\sigma_{1s_C} \rightarrow \pi_x^*}\rangle, \quad (\text{S54})$$

where the singlet excited states  $|^1\Psi_{\sigma_{1s_O} \rightarrow \pi_x^*}\rangle$  and  $|^1\Psi_{\sigma_{1s_C} \rightarrow \pi_x^*}\rangle$  are

$$\begin{aligned} |^1\Psi_{\sigma_{1s_O} \rightarrow \pi_x^*}\rangle &= \frac{1}{\sqrt{2}} (|\pi_x^* \sigma_{1s_C} \bar{\sigma}_{1s_O} \bar{\sigma}_{1s_C}\rangle + |\sigma_{1s_O} \sigma_{1s_C} \bar{\pi}_x^* \bar{\sigma}_{1s_C}\rangle), \\ |^1\Psi_{\sigma_{1s_C} \rightarrow \pi_x^*}\rangle &= \frac{1}{\sqrt{2}} (|\sigma_{1s_O} \pi_x^* \bar{\sigma}_{1s_O} \bar{\sigma}_{1s_C}\rangle + |\sigma_{1s_O} \sigma_{1s_C} \bar{\sigma}_{1s_O} \bar{\pi}_x^*\rangle). \end{aligned} \quad (\text{S55})$$

We chose the following ordering of orbitals, such that the parity mapping (30) with the  $Z_2$

reduction (29) for  $N_e = 4$  and  $N_e^\alpha = 2$  leads to

$$\begin{aligned} |n_0 n_1 n_2 n_3 n_4 n_5\rangle &= |n_{\sigma_{1s_O}} n_{\pi_x^*} n_{\sigma_{1s_C}} n_{\bar{\sigma}_{1s_O}} n_{\bar{\pi}_x^*} n_{\bar{\sigma}_{1s_C}}\rangle \\ \rightarrow |n_0(n_0 + n_1 \bmod 2) n_3(n_3 + n_4 \bmod 2)\rangle &= |q_0 q_1 q_2 q_3\rangle. \end{aligned} \quad (\text{S56})$$

As a result, the Hartree-Fock reference and the singlet excited states become

$$|\Psi_0\rangle = |1111\rangle = U_0|0000\rangle, \quad U_0 = X_0 X_1 X_2 X_3, \quad (\text{S57})$$

$$|^1\Psi_{\sigma_{1s_O} \rightarrow \pi_x^*}\rangle = \frac{1}{\sqrt{2}}(|0111\rangle + |1101\rangle), \quad (\text{S58})$$

$$|^1\Psi_{\sigma_{1s_C} \rightarrow \pi_x^*}\rangle = \frac{1}{\sqrt{2}}(|1011\rangle + |1110\rangle). \quad (\text{S59})$$

The circuit in Fig. 5b for Eq. (S54) can be found by first preparing  $|01\rangle \cos \frac{\theta}{2} + |10\rangle \sin \frac{\theta}{2} e^{i\phi}$  for the first two qubits, and then applying two entangling gates to create singlets,

$$\begin{aligned} |x(\theta, \phi)\rangle &= U_{1,3} U_{0,2} \left( |0111\rangle \cos \frac{\theta}{2} + |1011\rangle \sin \frac{\theta}{2} e^{i\phi} \right) \\ &= \frac{\cos \frac{\theta}{2}}{\sqrt{2}} (|0111\rangle + |1101\rangle) + \frac{\sin \frac{\theta}{2} e^{i\phi}}{\sqrt{2}} (|1011\rangle + |1110\rangle), \end{aligned} \quad (\text{S60})$$

where  $U_{i,j}$  ( $i < j$ ) is the entangling gate between  $Q_i$  and  $Q_j$  given by

$$U_{i,j} = \begin{bmatrix} 1 & 0 & 0 & 0 \\ 0 & \frac{1}{\sqrt{2}} & -\frac{1}{\sqrt{2}} & 0 \\ 0 & \frac{1}{\sqrt{2}} & \frac{1}{\sqrt{2}} & 0 \\ 0 & 0 & 0 & 1 \end{bmatrix} = R_{z,j}(\frac{\pi}{2}) \sqrt{i\text{SWAP}}_{i,j} R_{z,j}(-\frac{\pi}{2}). \quad (\text{S61})$$

## S4.2 Details of VQR algorithm

With the mapping in Eq. (S56), the active space Hamiltonian in Eq. (S53) can be written as

$$\hat{H} = \sum_{k=0}^{15} h_k P_k, \quad P_k \in \{I, Z\}^{\otimes 4}, \quad (\text{S62})$$

where the coefficients  $h_k$  are listed in Table S6. Consequently,  $\hat{A}^\dagger(\omega)\hat{A}(\omega)$  can be written as

$$\hat{A}^\dagger(\omega)\hat{A}(\omega) = \sum_{k=0}^{15} b_k(\omega) P_k, \quad P_k \in \{I, Z\}^{\otimes 4}. \quad (\text{S63})$$

Table S6: Coefficients of Pauli operators in  $\hat{H}_0$  (S62) for CO.

$h_{IIII}$	$h_{IIIZ}$	$h_{IIZZ}$	$h_{IIZI}$	$h_{IZII}$	$h_{ZZII}$	$h_{ZIII}$	$h_{IZIZ}$
-40.020060	6.444399	0.495229	11.498733	6.444399	0.495229	11.498733	0.877337
$h_{ZZIZ}$	$h_{ZIIZ}$	$h_{IZZZ}$	$h_{ZZZZ}$	$h_{ZIZZ}$	$h_{IZZI}$	$h_{ZZZI}$	$h_{ZIZI}$
0.187578	0.117327	0.187578	0.148295	0.160872	0.117327	0.160872	1.186150

with the coefficients  $b_k(\omega)$  can be computed from  $h_k$ .

Here, the perturbation operator  $\hat{V} = \hat{x}$  is the dipole moment operator in the  $x$  direction,

$$\hat{V} = x_O(X_0 + X_2) + x_C(X_1 + X_3), \quad x_O = -0.039321, \quad x_C = 0.079275. \quad (\text{S64})$$

By restricting the bra state to the Hartree-Fock state and the ket state in the space of the singlet excited state manifold in Eq. (S54), an effective operator for  $\hat{V}^\dagger \hat{A}(\omega)$  can be found as

$$\begin{aligned} (\hat{V}^\dagger \hat{A}(\omega))_{\text{eff}} &= c_0(\omega)X_0 + c_1(\omega)X_1, \\ c_0(\omega) &= 2x_O[\omega_O - (\omega + i\gamma)], \\ c_1(\omega) &= 2x_C[\omega_C - (\omega + i\gamma)]. \end{aligned} \quad (\text{S65})$$

With Eq. (S65), the cross term  $|\langle \Psi_0 | \hat{V}^\dagger \hat{A}(\omega) | x \rangle|^2$  can be derived as

$$\begin{aligned} |\langle \Psi_0 | \hat{V}^\dagger \hat{A}(\omega) | x \rangle|^2 &= |c_0(\omega)|^2 |\langle \Psi_0 | X_0 | x \rangle|^2 + |c_1(\omega)|^2 |\langle \Psi_0 | X_1 | x \rangle|^2 \\ &\quad + 2\text{Re}(\bar{c}_0(\omega)c_1(\omega))\text{Re}(\langle x | X_0 | \Psi_0 \rangle \langle \Psi_0 | X_1 | x \rangle) \\ &\quad - 2\text{Im}(\bar{c}_0(\omega)c_1(\omega))\text{Im}(\langle x | X_0 | \Psi_0 \rangle \langle \Psi_0 | X_1 | x \rangle). \end{aligned} \quad (\text{S66})$$

The two diagonal pairs  $|\langle 0 | U_0^\dagger X_k U_1 | 0 \rangle|^2$  ( $k \in \{0, 1\}$ ) are simple to compute, because  $|\Psi_0\rangle = |1111\rangle$  is a product state. Once the response state  $|x(\theta, \phi)\rangle$  in Eq. (S60) is prepared, the probabilities  $P_{0111}$  and  $P_{1011}$  give the values for the diagonal pairs. Thus, the diagonal pairs can be computed at the same time as computing  $\langle x | \hat{A}^\dagger(\omega) \hat{A}(\omega) | x \rangle$ . For the off-diagonal pairs, the real part  $\text{Re}(\langle x | X_0 | \Psi_0 \rangle \langle \Psi_0 | X_1 | x \rangle)$  can be computed using Eq. (S29), similar to the case for  $\text{H}_2$ . Based on Eq. (S31), the imaginary part  $\text{Im}(\langle 0 | U_1^\dagger X_0 U_0 | 0 \rangle \langle 0 | U_0^\dagger X_1 U_1 | 0 \rangle)$  can be computed by further noting  $\langle 1111 | X_0 e^{-i\frac{\pi}{4} X_0 X_1} = \langle 1111 | X_0 e^{-i\frac{\pi}{8}(X_0 X_1 + Y_0 Y_1)} = \langle 1111 | X_0 \sqrt{i\text{SWAP}}_{0,1}$ , such that

$$\text{Im}(\langle 0 | U_1^\dagger X_0 U_0 | 0 \rangle \langle 0 | U_0^\dagger X_1 U_1 | 0 \rangle) = -|\langle 0 | U_0^\dagger X_0 \sqrt{i\text{SWAP}}_{0,1} U_1 | 0 \rangle|^2 + \frac{1}{2} \left( |\langle 0 | U_0^\dagger X_0 U_1 | 0 \rangle|^2 + |\langle 0 | U_0^\dagger X_1 U_1 | 0 \rangle|^2 \right) \quad (\text{S67})$$

where the first term can be computed by preparing  $\sqrt{i\text{SWAP}}_{0,1}U_1|0\rangle$  and measuring the probability  $P_{0111}$ . All the necessary components for computing the cross term  $|\langle\Psi_0|\hat{V}^\dagger\hat{A}(\omega)|x\rangle|^2$  in Eq. (S66) are summarized in Table S7, and the necessary quantum circuits are shown in Fig. 5b.

Table S7: Components of  $|\langle\Psi_0|\hat{V}^\dagger\hat{A}(\omega)|x\rangle|^2$  (S66) in the VQR calculations for CO.

term	coefficient
$ \langle\Psi_0 X_0 x\rangle ^2$	$ c_0(\omega) ^2 - \text{Re}(\bar{c}_0(\omega)c_1(\omega)) - \text{Im}(\bar{c}_0(\omega)c_1(\omega))$
$ \langle\Psi_0 X_1 x\rangle ^2$	$ c_1(\omega) ^2 - \text{Re}(\bar{c}_0(\omega)c_1(\omega)) - \text{Im}(\bar{c}_0(\omega)c_1(\omega))$
$ \langle\Psi_0 R_{x,0}(\frac{\pi}{2})R_{x,1}(\frac{\pi}{2}) x\rangle ^2$	$4\text{Re}(\bar{c}_0(\omega)c_1(\omega))$
$ \langle\Psi_0 X_0\sqrt{i\text{SWAP}}_{0,1} x\rangle ^2$	$-2\text{Im}(\bar{c}_0(\omega)c_1(\omega))$

### S4.3 Error mitigation via spin symmetry projection

To improve the accuracy of computing  $\langle x|\hat{A}^\dagger(\omega)\hat{A}(\omega)|x\rangle$  and  $\langle x|\hat{A}^\dagger(\omega)|x\rangle$ , the error mitigation (EM) strategy via symmetry projection can be used with the symmetry projector for the singlet excited state manifold in Eq. (S54),

$$\begin{aligned}
\mathcal{P}_S &= \mathcal{P}_S^O + \mathcal{P}_S^C, \\
\mathcal{P}_S^O &= \frac{1}{2}(|0111\rangle + |1101\rangle)(\langle 0111| + \langle 1101|) \\
&= \frac{1}{16}(I - Z_0Z_2 + X_0X_2 + Y_0Y_2)(I - Z_1)(I - Z_3), \\
\mathcal{P}_S^C &= \frac{1}{2}(|1011\rangle + |1110\rangle)(\langle 1011| + \langle 1110|) \\
&= \frac{1}{16}(I - Z_1Z_3 + X_1X_3 + Y_1Y_3)(I - Z_0)(I - Z_2). \tag{S68}
\end{aligned}$$

The detailed expressions in terms of Pauli operators can be found in Table S8. Similar to the discussion for Eq. (S52), we can replace the expectation value  $\langle x|P_k|x\rangle$  for  $P_k$  in  $\hat{A}^\dagger(\omega)$  or  $\hat{A}^\dagger(\omega)\hat{A}(\omega)$  by the error-mitigated one  $\frac{\langle x|P_k\mathcal{P}_S|x\rangle}{\langle x|\mathcal{P}_S|x\rangle}$ . The correspondences have been summarized in Table S9. Apart from the measurements in the computational basis, it is seen that this EM

strategy requires  $4 + 4 = 8$  groups of additional measurements for estimating terms containing  $XX$ ,  $XY$ ,  $YX$ , or  $YY$  for  $Q_0$ - $Q_2$  or  $Q_1$ - $Q_3$ .

Table S8: Expressions for the projectors  $\mathcal{P}_S^O$ ,  $\mathcal{P}_S^C$  and  $\mathcal{P}_S$  in Eq. (S68) in terms of Pauli operators. Operators in the same parentheses are grouped to be measured simultaneously.

projector $\mathcal{P}$	expression for $16\mathcal{P}$
$\mathcal{P}_S^O$	$(IIII - ZZZZ - IIIZ - IZII + ZZZI + ZIZZ + IZIZ - ZIZI) + (XIXI - XIXZ - XZXI + XZXX) + (YIYI - YIYZ - YZYI + YZYZ)$
$\mathcal{P}_S^C$	$(IIII - ZZZZ - IIZI - ZIII + ZZIZ + IZZZ + ZIZI - IZIZ) + (IXIX - ZXIX - IXZX + ZXZX) + (IYIY - ZYIY - IYZY + ZYZY)$
$\mathcal{P}_S$	$(2IIII - 2ZZZZ - IIIZ - IIZI - IZII - ZIII + ZZZI + ZZIZ + ZIZZ + IZZZ) + (IXIX - ZXIX - IXZX + ZXZX) + (XIXI - XIXZ - XZXI + XZXX) + (IYIY - ZYIY - IYZY + ZYZY) + (YIYI - YIYZ - YZYI + YZYZ)$

## S4.4 VQR experiments

To study the X-ray absorption spectra of CO, we chose 118 frequency points ( $\omega$  in eV) that cover the region of interest from 230 eV to 610 eV [python code: `np.hstack((np.linspace(230, 340, 56), np.linspace(345, 495, 21), np.linspace(500, 610, 41)))`]. A broadening factor of  $\gamma = 0.5$  a.u. was used. In this work, to optimize the cost function  $L(\theta, \phi)$ , we scan the entire parameter space,  $\theta \in [0, \pi)$  and  $\phi \in [0, 2\pi)$ . To this end, its landscape is constructed on a two-dimensional grid  $(\theta_i, \phi_j)$  [python code: `theta=np.linspace(0.0, 3.2, 33), phi=np.linspace(0.0, 6.3, 64)`]. After balancing the effects of finite samplings, time overheads, and accuracy, each term in the cost function  $L(\theta_i, \phi_j)$  is derived from the average of measurements with a fixed sample size 30000. The experimental results for  $\langle \Psi_0 | \hat{V}^\dagger \hat{V} | \Psi_0 \rangle \langle x(\theta, \phi) | \hat{A}^\dagger(\omega) \hat{A}(\omega) | x(\theta, \phi) \rangle$  (with EM),  $|\langle \Psi_0 | \hat{V}^\dagger \hat{A}(\omega) | x(\theta, \phi) \rangle|^2$ , and  $L(\theta, \phi)$  are shown in Figs. S12, S13, and S14, respectively. The landscape of  $L(\theta, \phi)$  at a given frequency  $\omega$  is constructed by cubic spline interpolations and smoothing, which is used to determine the

location of the minimum and the optimized angles  $(\theta^{\text{opt}}, \phi^{\text{opt}})$ .

Since  $\hat{A}^\dagger(\omega)\hat{A}(\omega)$  in Eq. (S63) is diagonal,  $\theta$  is the most crucial angle for computing spectra. With Eq. (S60), the theoretical value for  $\langle x|\hat{A}^\dagger(\omega)\hat{A}(\omega)|x\rangle$  with the ideal angle  $\theta^*$  can be found as

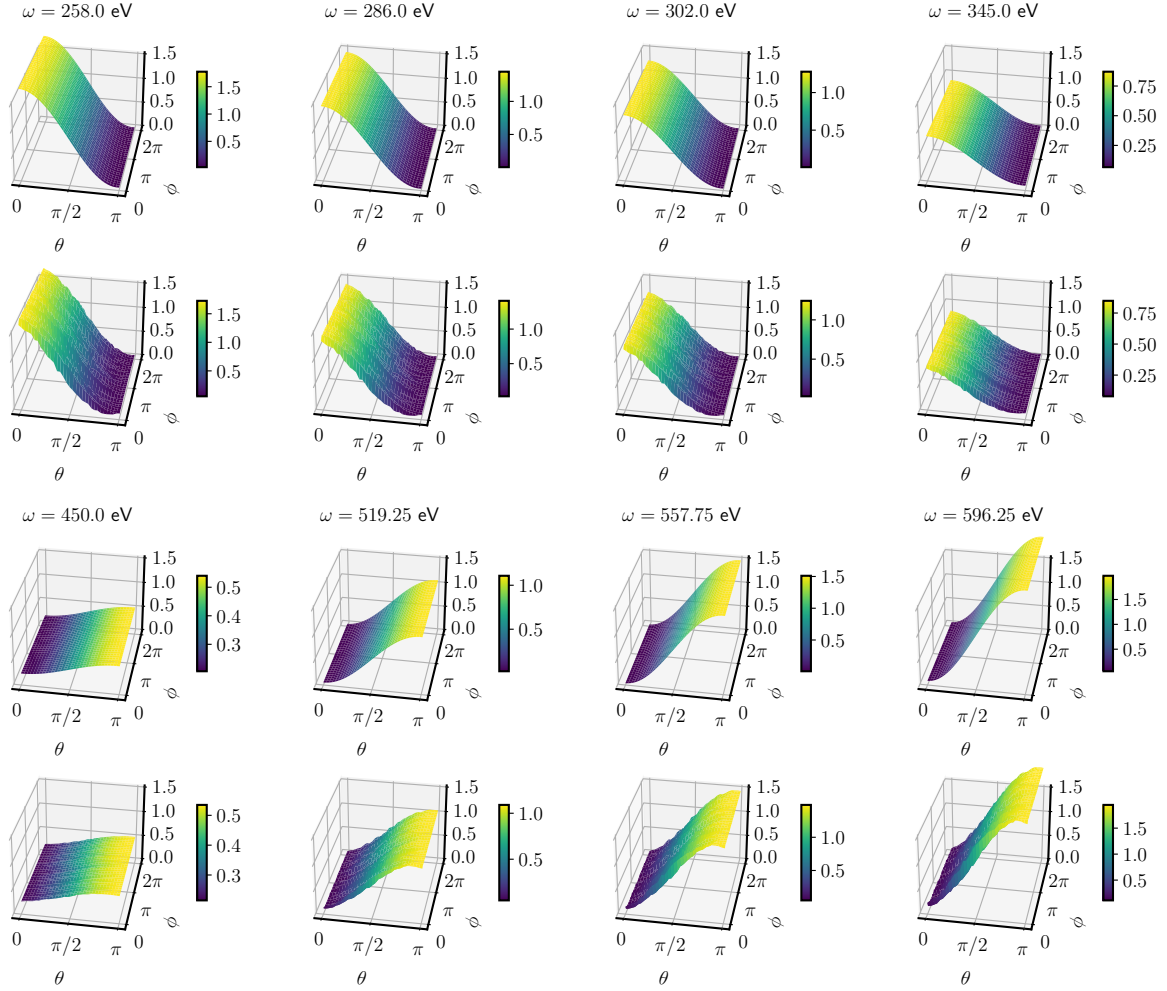
$$\begin{aligned}\langle x|\hat{A}^\dagger(\omega)\hat{A}(\omega)|x\rangle^* &= (\omega - \omega_O)^2 p_S^O + (\omega - \omega_C)^2 p_S^C + \gamma^2, \\ p_S^O &= \cos^2(\theta^*/2), \quad p_S^C = \sin^2(\theta^*/2),\end{aligned}\tag{S69}$$

where  $p_S^O$  and  $p_S^C$  represent the populations of  $|^1\Psi_{\sigma_{1s_O} \rightarrow \pi_x^*}\rangle$  and  $|^1\Psi_{\sigma_{1s_C} \rightarrow \pi_x^*}\rangle$  in the response state, respectively. In Fig. S15a, we compare the optimized angle  $\theta^{\text{opt}}$  corresponding to the minimum of  $L(\theta, \phi)$  as a function of  $\omega$  with the ideal one  $\theta^*$  in terms of the populations of singlets. It is seen that they agree well for  $\omega$  around  $\omega_C$ , whereas the deviation becomes larger for  $\omega$  around  $\omega_O$ . From Fig. S14, it is seen the landscape of  $L(\theta, \phi)$  is flatter around 519 eV, which makes it more susceptible to the errors of the two computed terms,  $\langle \Psi_0|\hat{V}^\dagger\hat{V}|\Psi_0\rangle\langle x|\hat{A}^\dagger(\omega)\hat{A}(\omega)|x\rangle$  and  $|\langle \Psi_0|\hat{V}^\dagger\hat{A}(\omega)|x\rangle|^2$ . As a result, the optimized  $\theta^{\text{opt}}$  exhibits a larger deviation from the ideal value in this frequency region.

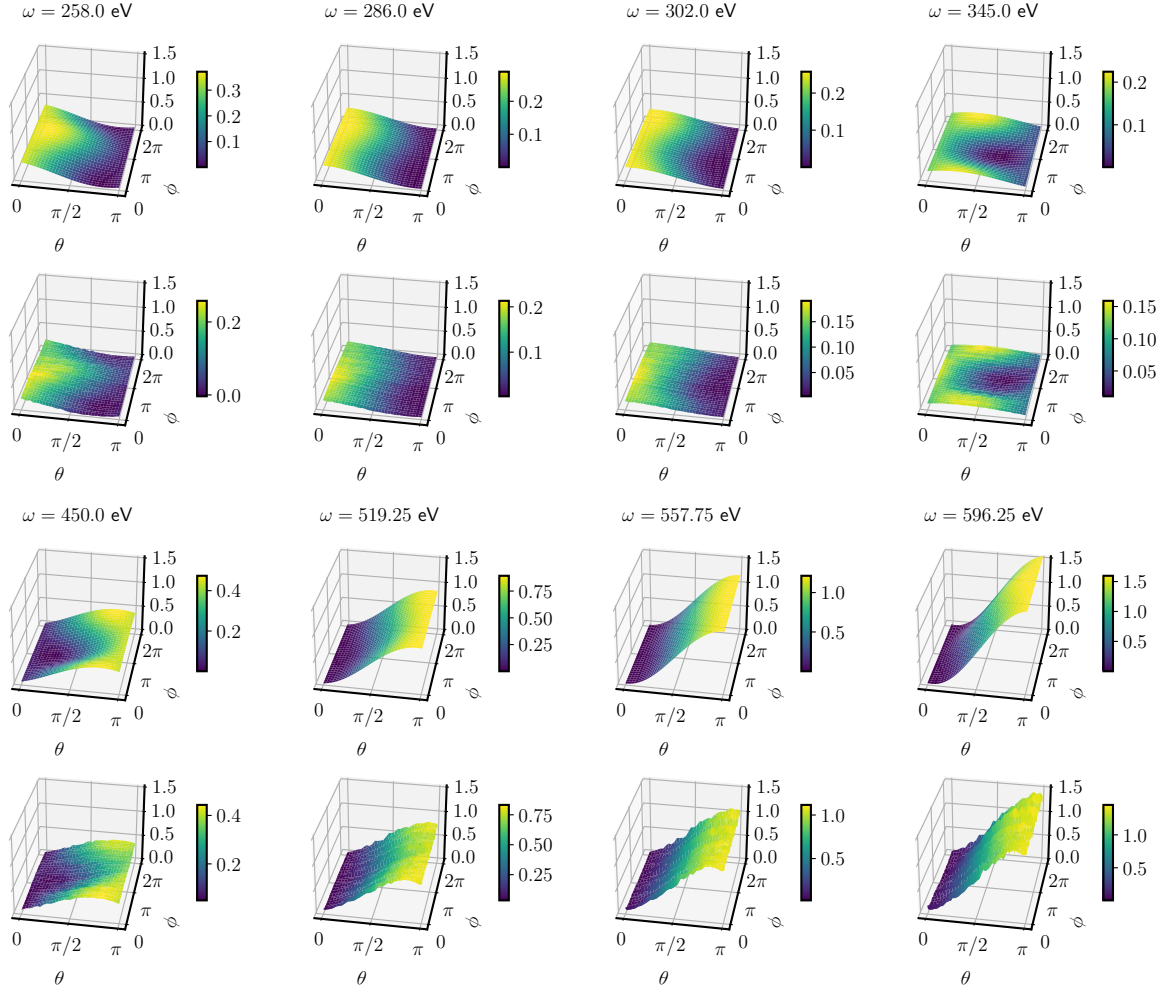
With the optimized angles  $(\theta^{\text{opt}}, \phi^{\text{opt}})$ , the X-ray absorption spectra can be computed by measuring  $\langle x(\theta^{\text{opt}}, \phi^{\text{opt}})|\hat{A}^\dagger(\omega)\hat{A}(\omega)|x(\theta^{\text{opt}}, \phi^{\text{opt}})\rangle$  for each  $\omega$ , see Eq. (S16). In Fig. S15b, we compare the raw experimental results and the error-mitigated results for  $\langle x|\hat{A}^\dagger(\omega)\hat{A}(\omega)|x\rangle$  at the optimized  $(\theta^{\text{opt}}, \phi^{\text{opt}})$  (labelled by raw and EM) and the ideal  $(\theta^*, \phi^*)$  (labelled by raw\* and EM\*), against the theoretical curve in Eq. (S69). It is clear that using EM significantly improves the accuracy of  $\langle x|\hat{A}^\dagger(\omega)\hat{A}(\omega)|x\rangle$ , and hence the computed spectra shown in Fig. 5c. The deviations of the EM results computed with the ideal angles from the theoretical curve is solely due to the errors in computing  $\langle x|\hat{A}^\dagger(\omega)\hat{A}(\omega)|x\rangle$  with QPU.

Table S9: Error mitigation strategy using  $\mathcal{P}_S$  for estimating the expectation values of  $\langle x|P_k|x\rangle$  by  $\frac{\langle x|P_k\mathcal{P}_S|x\rangle}{\langle x|\mathcal{P}_S|x\rangle}$ . Operators in the same parentheses are grouped to be measured simultaneously.

$P_k$	$16P_k\mathcal{P}^S$
$IIII$	$(2IIII - 2ZZZZ - IIIZ - IIZI - IZII - ZIII + ZZZI + ZZIZ + ZIZZ + IZZZ) + (IXIX - ZXIX - IXZX + ZXZX) + (XIXI - XIXZ - XZXI + XZXZ) + (IYIY - ZYIY - IYZY + ZYZY) + (YIYI - YIYZ - YZYI + YZYZ)$
$ZZZZ$	$(2ZZZZ - 2IIII + IIIZ + IIZI + IZII + ZIII - ZZZI - ZZIZ - ZIZZ - IZZZ) - (IXIX - ZXIX - IXZX + ZXZX) - (XIXI - XIXZ - XZXI + XZXZ) - (IYIY - ZYIY - IYZY + ZYZY) - (YIYI - YIYZ - YZYI + YZYZ)$
$ZIZI$	$(2ZIZI - 2IZIZ + IIIZ - IIZI + IZII - ZIII - ZZZI + ZZIZ - ZIZZ + IZZZ) + (IXIX - ZXIX - IXZX + ZXZX) - (XIXI - XIXZ - XZXI + XZXZ) + (IYIY - ZYIY - IYZY + ZYZY) - (YIYI - YIYZ - YZYI + YZYZ)$
$IZIZ$	$(-2ZIZI + 2IZIZ - IIIZ + IIZI - IZII + ZIII + ZZZI - ZZIZ + ZIZZ - IZZZ) - (IXIX - ZXIX - IXZX + ZXZX) + (XIXI - XIXZ - XZXI + XZXZ) - (IYIY - ZYIY - IYZY + ZYZY) + (YIYI - YIYZ - YZYI + YZYZ)$
$IIIZ$	$(2IIIZ - 2ZZZI - IIZZ - ZIIZ + ZZII + IZZI - IIII + ZIZI - IZIZ + ZZZZ) - (XIXI - XIXZ - XZXI + XZXZ) - (YIYI - YIYZ - YZYI + YZYZ) + i[(IXIY - ZXIY - IXZY + ZXZY) - (IYIX - ZYIX - IYZX + ZYZX)]$
$ZZZI$	$(2ZZZI - 2IIIZ + IIZZ + ZIIZ - ZZII - IZZI + IIII - ZIZI + IZIZ - ZZZZ) + (XIXI - XIXZ - XZXI + XZXZ) + (YIYI - YIYZ - YZYI + YZYZ) - i[(IXIY - ZXIY - IXZY + ZXZY) - (IYIX - ZYIX - IYZX + ZYZX)]$
$IIZI$	$(2IIZI - 2ZZIZ - IIZZ + ZIIZ + ZZII - IZZI - IIII - ZIZI + IZIZ + ZZZZ) - (IXIX - ZXIX - IXZX + ZXZX) - (IYIY - ZYIY - IYZY + ZYZY) + i[(XIIY - XIYZ - XZYI + XZYZ) - (YIXI - YIXZ - YZXI + YZXZ)]$
$ZZIZ$	$(2ZZIZ - 2IIZI + IIZZ - ZIIZ - ZZII + IZZI + IIII + ZIZI - IZIZ - ZZZZ) + (IXIX - ZXIX - IXZX + ZXZX) + (IYIY - ZYIY - IYZY + ZYZY) - i[(XIIY - XIYZ - XZYI + XZYZ) - (YIXI - YIXZ - YZXI + YZXZ)]$
$IZII$	$(2IZII - 2IZIZ + IIZZ + ZIIZ - ZZII - IZZI - IIII + ZIZI - IZIZ + ZZZZ) - (XIXI - XIXZ - XZXI + XZXZ) - (YIYI - YIYZ - YZYI + YZYZ) - i[(IXIY - ZXIY - IXZY + ZXZY) - (IYIX - ZYIX - IYZX + ZYZX)]$
$ZIZZ$	$(2ZIZZ - 2IZII - IIZZ - ZIIZ + ZZII + IZZI + IIII - ZIZI + IZIZ - ZZZZ) + (XIXI - XIXZ - XZXI + XZXZ) + (YIYI - YIYZ - YZYI + YZYZ) + i[(IXIY - ZXIY - IXZY + ZXZY) - (IYIX - ZYIX - IYZX + ZYZX)]$
$ZIII$	$(2ZIII - 2IZZZ + IIZZ - ZIIZ - ZZII + IZZI - IIII - ZIZI + IZIZ + ZZZZ) - (IXIX - ZXIX - IXZX + ZXZX) - (IYIY - ZYIY - IYZY + ZYZY) - i[(XIIY - XIYZ - XZYI + XZYZ) - (YIXI - YIXZ - YZXI + YZXZ)]$
$IZZZ$	$(2IZZZ - 2ZIII - IIZZ + ZIIZ + ZZII - IZZI + IIII + ZIZI - IZIZ - ZZZZ) + (IXIX - ZXIX - IXZX + ZXZX) + (IYIY - ZYIY - IYZY + ZYZY) + i[(XIIY - XIYZ - XZYI + XZYZ) - (YIXI - YIXZ - YZXI + YZXZ)]$
$ZZII$	$(2ZZII - 2IIZZ + IIIZ + IIZI - IZII - ZIII - ZZZI - ZZIZ + ZIZZ + IZZZ) + i[(IXIY - ZXIY - IXZY + ZXZY) + (XIIY - XIYZ - XZYI + XZYZ) - (IYIX - ZYIX - IYZX + ZYZX) - (YIXI - YIXZ - YZXI + YZXZ)]$
$IIZZ$	$(2IIZZ - 2ZZII - IIIZ - IIZI + IZII + ZIII + ZZZI + ZZIZ - ZIZZ - IZZZ) - i[(IXIY - ZXIY - IXZY + ZXZY) + (XIIY - XIYZ - XZYI + XZYZ) - (IYIX - ZYIX - IYZX + ZYZX) - (YIXI - YIXZ - YZXI + YZXZ)]$
$IZZI$	$(2IZZI - 2ZIIZ + IIIZ - IIZI - IZII + ZIII - ZZZI + ZZIZ + ZIZZ - IZZZ) + i[(IXIY - ZXIY - IXZY + ZXZY) - (XIIY - XIYZ - XZYI + XZYZ) - (IYIX - ZYIX - IYZX + ZYZX) + (YIXI - YIXZ - YZXI + YZXZ)]$
$ZIIZ$	$(2ZIIZ - 2IZZI - IIIZ + IIZI + IZII - ZIII + ZZZI - ZZIZ - ZIZZ + IZZZ) - i[(IXIY - ZXIY - IXZY + ZXZY) - (XIIY - XIYZ - XZYI + XZYZ) - (IYIX - ZYIX - IYZX + ZYZX) + (YIXI - YIXZ - YZXI + YZXZ)]$



**Fig. S12. Landscapes of  $\langle \Psi_0 | \hat{V}^\dagger \hat{V} | \Psi_0 \rangle \langle x(\theta, \phi) | \hat{A}^\dagger(\omega) \hat{A}(\omega) | x(\theta, \phi) \rangle$  at eight representative frequencies  $\omega$ . Upper row: ideal results; Lower row: experimental results.**



**Fig. S13. Landscapes of  $|\langle \Psi_0 | \hat{V}^\dagger \hat{A}(\omega) | x(\theta, \phi) \rangle|^2$  at eight representative frequencies  $\omega$ . Upper row: ideal results; Lower row: experimental results.**

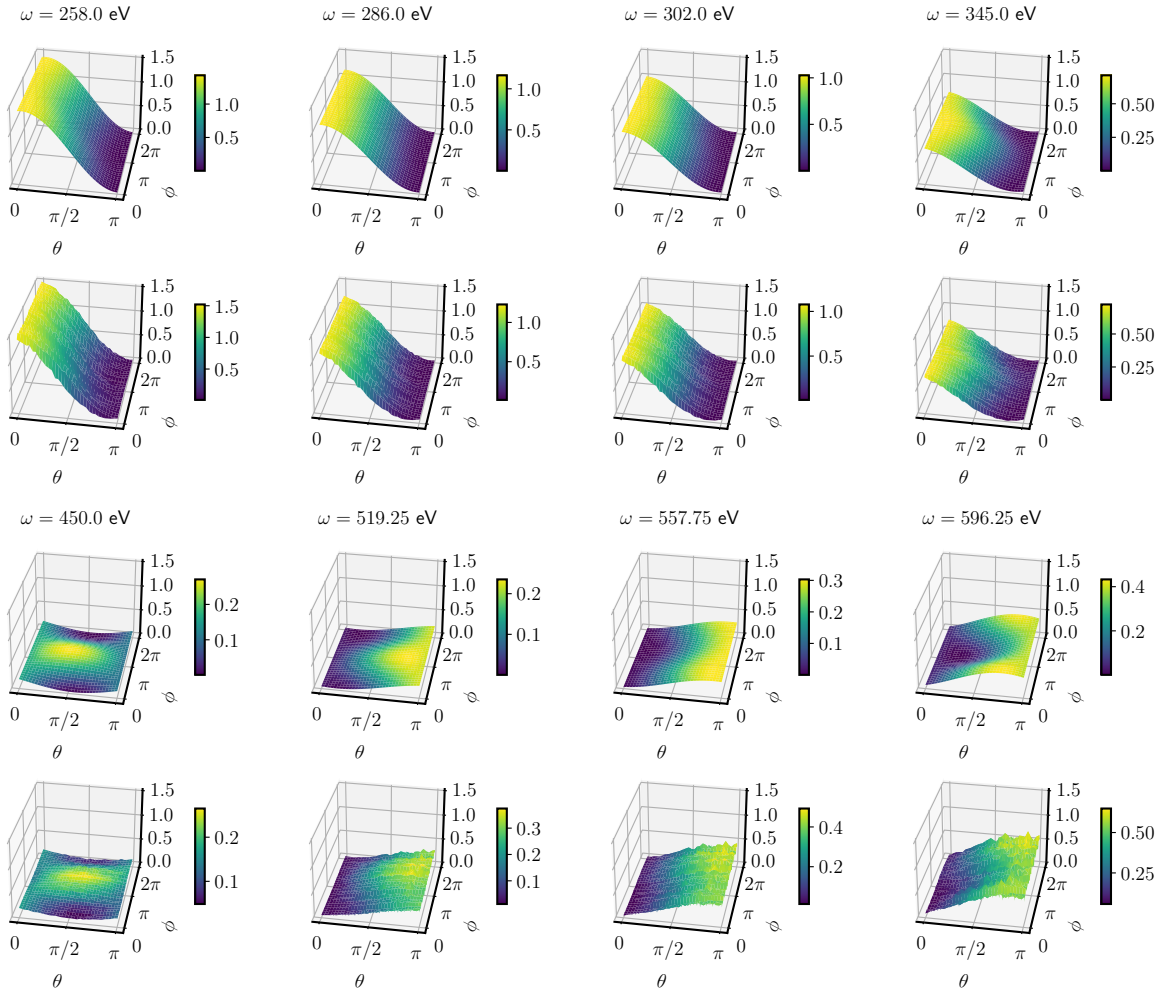


**Fig. S14. Landscapes of the cost function  $L(\theta, \phi)$  at eight representative frequencies  $\omega$ .** Upper row: ideal results; Lower row: experimental results.

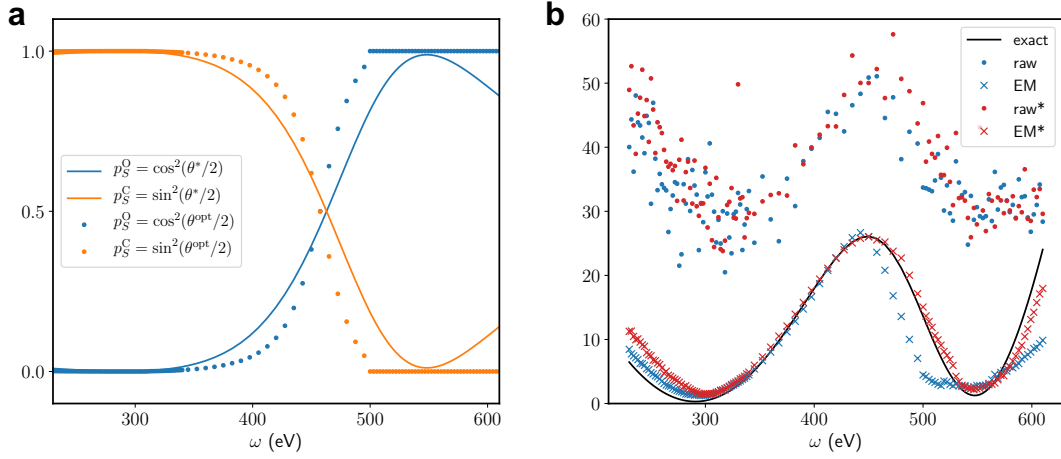


**Fig. S15.** Experimental results for the optimized angles  $\theta$  and the computed  $\langle x | \hat{A}^\dagger(\omega) \hat{A}(\omega) | x \rangle$  for  $\chi(\omega)$  in the VQR calculations for CO. a, The optimized  $\theta^{\text{opt}}$  compared against the ideal  $\theta^*$  at each frequency. b, The raw experimental results and the error-mitigated results for  $\langle x | \hat{A}^\dagger(\omega) \hat{A}(\omega) | x \rangle$  at the optimized  $\theta^{\text{opt}}$  (labelled by raw and EM) and the ideal  $\theta^*$  (labelled by raw\* and EM\*), compared against the theoretical curve (the black line)  $\langle x | \hat{A}^\dagger(\omega) \hat{A}(\omega) | x \rangle^*$  in Eq. (S69).